Automated aberration correction for STED microscopy

Dissertation

presented for the award of the degree

'Doctor rerum naturalium' (Dr.rer.nat)

of the Georg-August-Universität Göttingen

within the doctoral program physics

of the Georg-August University School of Science (GAUSS)

submitted by

Debadrita Ghosh

Bardhaman, West Bengal, India

Göttingen, June 2023

Thesis Committee

Apl. Prof. Dr. Alexander Egner
Optical Nanoscopy
Institute for Nanophotonics Goettingen e.V.

Prof. Dr. Jörg Enderlein
III. Physical Institute
Biophysics / Complex Systems
Georg-August-University Goettingen

Prof. Dr. Sarah Köster
Institute for X-Ray Physics
Georg-August-University Goettingen

Members of the Examination Board

Reviewer 1: **Apl. Prof. Dr. Alexander Egner**

Reviewer 2: **Prof. Dr. Jörg Enderlein**

Further members of the Examination Board

Prof. Dr. Sarah Köster
Institute for X-Ray Physics
Georg-August-University Goettingen

Prof. Dr. Timo Betz
III. Physical Institute
Biophysics / Complex Systems
Georg-August-University Goettingen

Apl. Prof. Dr. Michael Seibt
IV. Physical Institute
Georg-August-University Goettingen

Prof. Dr. Fred S. Wouters
Institute for Neuropathology
Laboratory for Molecular and Cellular Systems
University Medical Center Goettingen

Date of the oral examination: July 13, 2023

Abstract

Stimulated emission depletion (STED) microscopy is a powerful super resolution fluorescence microscopy technique that surpasses the diffraction limit [1]. However, the performance of a STED microscope can be adversely influenced by aberrations [2]. In thick biological specimens, aberrations are primarily induced by wavefront distortion caused by variations in the refractive index within the specimen. These aberrations have a substantial impact on the quality of the acquired images and impose limitations on the achievable resolution. This problem can be resolved by using adaptive optics (AO) in a feedback controlled manner such that the wavefront distortions are appropriately compensated, and the image quality is restored. In most cases, the feedback loop in aberration correction techniques relies on using a combination of certain image features as a metric. This approach often requires multiple acquisitions of the same field of view (FOV) [3, 4] to assess and optimize the metric. However, this process is inherently slow and can be prone to unwanted photo bleaching effects. In this thesis, a novel AO based correction scheme is developed, utilizing a newly patented metric [5]. This metric distinguishes itself from traditional methods by not relying on image features but instead capitalizes on the relationship between the fluorescence lifetime and the intensity of the depletion beam employed in STED microscopy. By directly extracting this property from the fluorescence photon stream and utilizing it as a metric, we successfully demonstrate automated and continuous aberration correction for STED imaging and additionally explore its application to confocal imaging. We show that the photon stream-based metric enables swift aberration correction in parallel with image acquisition also in biological samples. This advance significantly speeds up aberration-corrected imaging and makes it accessible to users without technical expertise.

Acronyms

2D	Two Dimensional
πPP	π Phase Plate
AO	Adaptive Optics
AOM	Acousto Optic Modulator
APD	Avalanche Photo Diode
DM	Deformable Mirror
FOV	Field of View
FWHM	Full Width at Half Maxima
HWP	Half Wave Plate
NA	Numerical Aperture
PMT	Photo Multiplier Tube
PSF	Point Spread Function
PV	Peak to Valley
RMS	Root Mean Square
SLM	Spatial Light Modulator
STED	Stimulated Emission Depletion
VPP	Vortex Phase Plate

Contents

List of Figures

Chapter 1

Background and motivation

The invention of the microscope and its advancement over a time span of a few hundred years has opened up a new horizon about the microscopic world and has led to a great improvement in the studies of life sciences, physical sciences and chemical science. Light microscopy, particularly confocal fluorescence microscopy has become an indispensable tool to observe and explore the structure and physiology of cells and tissue as fluorescence microscopy offers a high contrast by absorbing light of a certain wavelength and emitting at a longer wavelength. Fluorescent markers can be attached to a specific protein or molecule which is another advantage of fluorescence microscopy.

However, for many years, the range of application of fluorescence microscopy has been limited due to its limited spatial resolution governed by the physical law of diffraction. The major component of a fluorescence microscope is an objective lens that collects light from an object and produces the corresponding image. Due to the wave nature of light, light waves cannot be focused to an infinitesimally small point in the object plane. Instead, they produce a smeared spot having a characteristic intensity profile, which is known as point spread function (PSF) of the microscope. The size of the PSF imposes a limitation on the resolution of the microscope. In 1873, the famous German physicist, Ernst Karl Abbe published an empirical formula that describes the closest distance of two points at which they can still be resolved and thus also gives an estimate of the size of the diffraction limited spot as [6],

$$d = \frac{\lambda}{2\ n\ \sin\alpha}\ , \tag{1.1}$$

where λ is the wavelength of the light, n is the refractive index of the medium between the objective lens and the specimen and α is the half angle of the light cone that can enter or exit the objective lens. The quantity $n \sin\alpha$ is known as the numerical aperture (*NA*) of the objective lens.

Over the past two decades, new techniques have been developed in the field of fluorescence microscopy that have pushed resolution beyond the imposed diffraction limit. STED is one of the techniques developed by Stefan Hell and J. Wichmann, that yields sub-diffraction resolution while retaining the beneficial aspects of fluorescence microscopy [1]. In STED microscopy, the resolution limit is overcome by exploiting the inherent photo physical properties of the fluorescent molecules to reduce the size of the effective focal spot from where fluorescence is emitted [7]. A STED microscope uses two laser beams, an excitation laser beam that excites the fluorescent molecules to an excited state, while the other laser beam, referred to as STED laser beam, depletes the molecules from the excited state to the ground state via stimulated emission. In STED microscopy, fluorescence is selectively turned off from the outer region of the Gaussian excitation focus and the molecules at the center region are allowed to fluoresce. This targeted switching off process is achieved by making the intensity profile of the STED laser beam doughnut-shaped at the focus of the objective lens, featuring a local zero intensity at the center. Overlaying such a STED beam with a Gaussian excitation beam, the effective size of the PSF is reduced, thus the achievable resolution of the microscope is enhanced. The size of the effective PSF depends on the intensity of the STED beam, making the achievable resolution theoretically infinite. However, in practice, low signal-to-noise ratio, photo bleaching of the fluorescent molecules, and aberrations present in the system restrict the obtainable resolution.

The performance of a STED microscope is affected by optical aberrations arising from limitations of optical components or spatial variations of the refractive index within the specimen. In ideal imaging conditions, the wavefronts which are emitted from an illuminated point-object and collected by the objective lens are spherical. However, due to the imperfections of the optical system, the wavefronts are distorted. The deviation of an actual wavefront from an ideal wavefront is known as wavefront aberration. Even with the almost perfect optical components, aberrations occur when light passes through a

specimen which is mounted in a substance whose refractive index is different from the refractive index of the immersion medium of the objective lens [8]. For example, when live cells are embedded in physiological buffer solution and imaged by an oil objective lens, spherical aberration arises due to a mismatch of the refractive indices of the immersion medium and the embedding medium.

Aberrations lead the intensity distribution at the focal spot to lose its symmetry and result in a larger spread of the focal volume. This deformation reduces the resolution of the microscope and the peak intensity of the detected signal and leads to a degradation of the image quality. The problem is further increased when imaging deep into an aberrating sample and it can render the high resolution imaging unachievable. Due to its detrimental effect on imaging quality, it is necessary to correct aberrations in the imaging system.

One way to correct aberrations is to use an objective lens with a correction collar which has been utilized to improve the image quality [9]. However, the correction collar only allows the correction of spherical aberrations. Adjustment of the correction collar induces an axial shift of the PSF and takes a significant amount of time to optimize. Another method, so-called static aberration correction technique, adapts the samples according to the requirements of the microscopy technique used [10, 11]. However, in bio-medical research, in order to minimize the generation of artifacts in the biological system and to study cells in their natural environment, minimally invasive sample preparation is preferred. Alternatively, one can also use deconvolution to remove the effects of aberrations from the image [12], but this technique requires an estimation of the unaberrated PSF for each point in the sample. Deconvolution can also be computationally intensive, which makes it less effective, specially for live cell imaging.

AO is a promising tool having a fast response time to correct aberrated wavefronts [13]. AO components, such as a deformable mirror (DM) or a spatial light modulator (SLM) manipulate the wavefronts to compensate for distortion. By introducing an equal and opposite phase distortion to that present in the system, AO compensates for aberrations.

AO was first introduced in astronomy to correct for the blurring in the telescope's images caused by the earth's atmosphere. Application of AO in optical microscopy was started in the early 2000s [14, 15]. Aberrations affect both the excitation and emission paths as both the light wavefront passes through the specimen. Wavefront correction for both ex-

citation and emission paths by using a DM has been successfully tested in a confocal fluorescence microscope [16, 17, 18].

AO based aberration correction methods are implemented in two ways, referred to as direct sensing and indirect optimization. Direct sensing measures aberrated wavefronts by a sensing device such as a Shack-Hartmann wavefront sensor. The information from the sensor is used to determine how the AO device needs to modulate the wavefront in order to compensate for the wavefront distortion [18]. The employment of this approach, when used for microscopy application, suffers from certain disadvantages. In general, the wavefront sensor is designed to work with a well-defined reference wavefront. This can be only provided by a point-like emitter. In a biological specimen, a single point-like emitter may not be encountered and light comes out from multiple points. And the superposition of many wavefronts create ambiguous sensor readings. Introducing a point-like object, so called a guide star, inside the specimen is not always straight-forward and poses a major challenge in tissue.

Indirect optimization does not measure the wavefront directly but usually optimizes a quality metric associated with the recorded images. Such image based metrics are based on brightness of the image [4, 19] or sharpness of the image [20] or both in a combination [17]. AO based aberration correction methods without direct wavefront sensing have been successfully applied in STED microscopy [16, 17]. However, optimization of such an image based metric requires iteration of image acquisition, computation of the image based metric for each iteration step, and adjustment of the AO. This is repeated until the best image quality is achieved. Therefore, the FOV of the sample has to be recorded for several AO configurations, making the process slow and prone to photo bleaching, which can lead to errors in determining the metric.

In this thesis, we present an AO based indirect aberration correction scheme which does not use an image based metric but a very recently introduced photon stream-based metric [5]. This metric makes use of the dependence of the fluorescence lifetime of the fluorescent probe on the local STED beam intensity rather than the structure and brightness of the sample. In principle, it can be evaluated on the single pixel level enabling the correction procedure simultaneously with image acquisition.

The aim of the thesis is to develop a method for aberration correction using a photon

stream-based metric, to correct multiple aberrations relevant in a biological sample. The method is further extended such that it is capable of continuously detecting and compensating for the aberrations during image acquisition. In addition to its use in single color STED microscopy, the correction scheme is also successfully applied in confocal and two-color STED microscopy.

The thesis is structured in the following manner: Chapter 2 provides a general introduction to image formation, microscopy techniques, and aberration. Chapter 3 describes the optical setup of the microscope and the corresponding characterizations that are used to validate the aberration correction method. In Chapter 4, the photon stream-based metric is explained and all the results obtained using this method are discussed. Finally, Chapter 5 presents a summary of the findings and a discussion.

Chapter 2

Theoretical background

This thesis employs the confocal scanning fluorescence microscopy imaging technique, to which STED microscopy is added to enhance its resolution. While STED microscopy offers an advantage over conventional techniques, it is also susceptible to aberrations, which can affect the image quality. By introducing a metric that is developed by analyzing the characteristics of the fluorescence photons, this thesis seeks to address these aberrations. Therefore, this chapter offers a basic overview of fluorescence and the pertinent microscopy method. The working principle of STED microscopy is also given. This chapter also discusses the mathematical representation of aberrations and its theoretical framework. Finally, this chapter discusses the latest metrics used to evaluate image quality for aberration correction.

2.1 Fluorescence

Fluorescence refers to the phenomenon where certain molecules absorb light at a specific wavelength and then spontaneously emit light at a longer wavelength. Fluorescence can be explained using the Jablonski diagram presented in Fig. 2.1(a) which depicts the energy states of a fluorescent molecule. S_0 and S_1 represent the singlet electronic states and with each electronic state multiple vibrational energy states, indicated by $0, 1, 2, 3...$, are coupled. A molecule in the ground state (S_0) is excited via absorption of an excitation photon at wavelength of λ_{exc} and reaches a higher energy state (S_1). A fluorescent

molecule typically undergoes excitation within a time range of $\sim 10^{-15}s$ [21]. Vibrational relaxation happens from this excited state to the vibrational ground state of S_1 through a non-radiative process that lasts for $\sim 10^{-12}s$ [21]. Afterwards, the fluorophore molecule decays from the electronic excited state back to the ground state, $S_1 \rightarrow S_0$, via spontaneous emission of a photon at wavelength of λ_{fl}. Emission of a photon and relaxation of the molecule to the ground state occurs on the relatively longer time scale of $\sim 10^{-9}s$ [21]. The cycle completes through a non-radiative transition to the lowest vibrational level of S_0. Typically at ambient temperature, the emitted photons is of lower energy than the absorption energy due to the energy loss in vibrational relaxation, and thus has a longer wavelength compared to the absorbed photons, known as the Stokes shift.

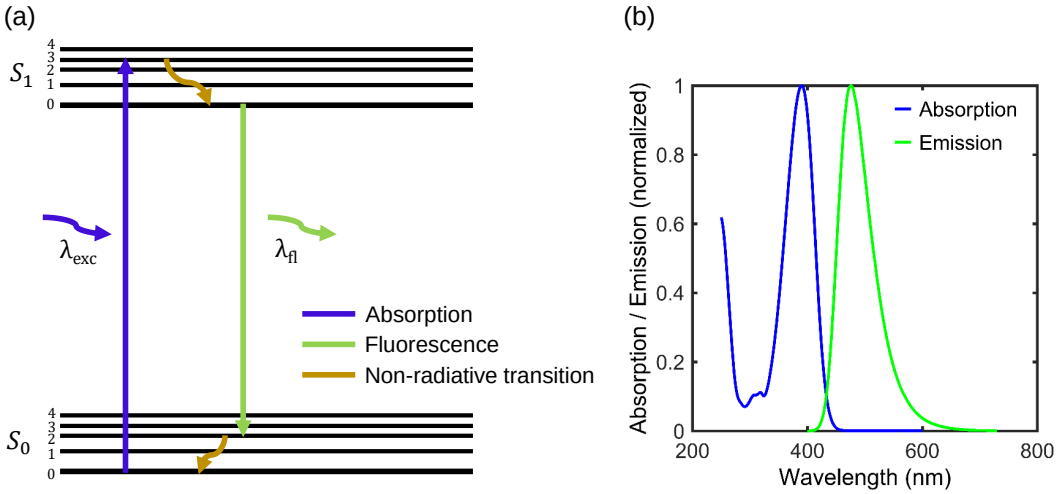

Figure 2.1: (a) The Jablonski diagram illustrates the energy states of a fluorescent molecule. S_0 and S_1 denote the electronic states, while $0, 1, 2, 3...$ and so on represent the vibrational sub energy levels. When a photon with energy of $h\frac{c}{\lambda_{exc}}$ is absorbed, where h is the Planck constant and c is the speed of light in vacuum, the molecule is excited to a higher vibrational energy level of S_1. This excited state rapidly undergoes non-radiative relaxation to the lowest vibrational level of S_1 within a few picoseconds. The molecule then relaxes back to the ground state by emitting a photon at wavelength of λ_{fl} in the form of fluorescence. (b) Absorption and emission spectra of Atto 390 dye. Spectrum data has been taken from atto-tec.com.

If the number of the molecules in the S_1, at time t is given by $N(t)$, the rate at which N changes is [21],

$$\frac{dN}{dt} = -\frac{1}{\tau_{fl}}N(t) \tag{2.1}$$

where τ_{fl} represents the lifetime of fluorescent molecules which is defined as the average time a molecule spends in an excited state before returning to its ground state via emitting

a photon. The solution to Eq.2.1 leads to a single exponential decay of fluorescence intensity [21].

$$I(t) = I_0 \; e^{-\frac{t}{\tau_{fl}}} \tag{2.2}$$

Here I_0 is the fluorescence intensity at time, $t = 0$. Fluorescence intensity is proportional to the amount of light absorbed by the molecules in their ground state, S_0 [21].

$$I \propto I_{exc} \tag{2.3}$$

Here, I_{exc} is the intensity of the excitation light. Fluorescence intensity can be reduced by various processes, one of which is photo bleaching. This process occurs when fluorescent molecules are exposed to high intensity light for a prolonged period, resulting in irreversible damage to the chemical bonds in the fluorophore. Fig. 2.1(b) shows an example of excitation and emission spectra of a fluorescent dye (ATTO 390, Atto-Tec, Germany) demonstrating the Stokes shift between the absorption and fluorescence spectra.

2.2 Confocal scanning fluorescence microscopy

The Stokes shift facilitates the separation of emission light from excitation light, and this can be utilized to implement a fluorescence microscope. In a common implementation of a fluorescence microscope, the excitation light is focused at the back focal plane of the objective lens to illuminate an extended area of the specimen that contains fluorescent molecules. This causes excitation of all the fluorescent molecules present in that area. A portion of their fluorescence is collected by the same objective lens and forms an image on the detector. A dichroic mirror is used to separate the excitation light and the emitted fluorescence based on their different wavelengths. However, the wide field illumination used in fluorescence microscopy has a disadvantage. Excitation of the molecules is not restricted to the focal plane, leading to out-of-focus signal contributing to the image formation. This can wash out features in the focal plane and generate background signals. To address this issue, in 1957, Marvin Minsky patented the working principle of confocal microscopy [22]. To secure that the signal only from the focal plane reaches the detector, a pinhole is introduced in the image plane of the object. The advantage of this config-

uration is that the pinhole distinguishes between different focal planes by blocking light coming from out-of-focus regions of the specimen. Thus, it provides the feature of optical sectioning to the microscope. To record the entire FOV either the sample needs to be scanned through an excitation focus or the focus needs to be scanned over the sample. Fig. 2.2 depicts the major parts of a standard confocal scanning fluorescence microscope. A collimated excitation light is reflected by a dichroic mirror and focused by an objective lens onto the specimen. With the same objective lens, a fraction of the fluorescence is collected, transmitted through the dichroic mirror, and then focused on the pinhole by a tube lens and afterwards collected by the detector. The pinhole guarantees that only the fluorescence emitted from the immediate area surrounding the geometric focal point is detected. In order to record a confocal image, the excitation focus is moved across the specimen while keeping the specimen stationary. This is achieved by using a set of mirrors usually in combination with an appropriate imaging system (not shown in Fig. 2.2) to scan the focus in x and y directions.

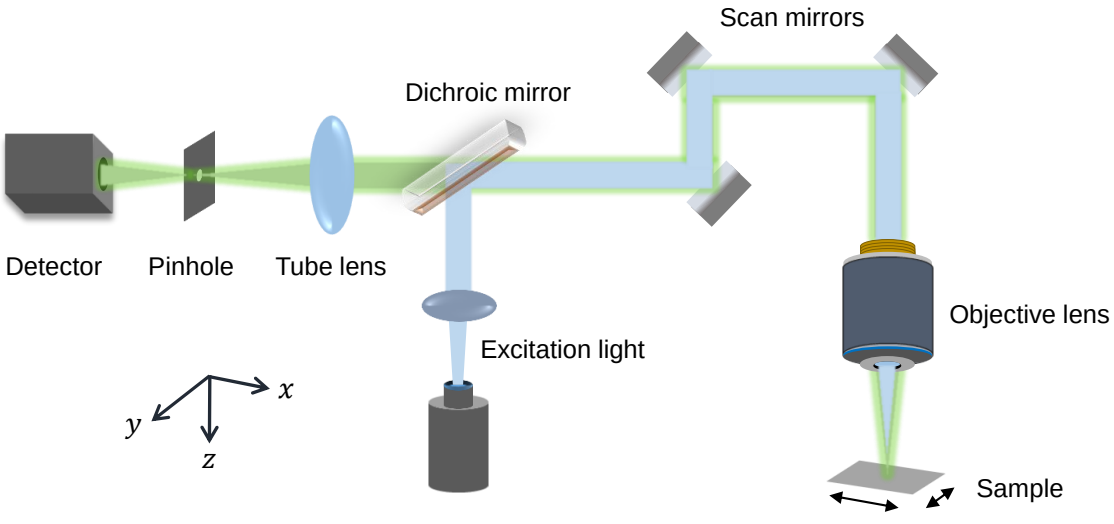

Figure 2.2: A typical confocal scanning fluorescence microscope setup with a collimated excitation beam (blue) focused by the objective lens onto the specimen. The focus is moved across the specimen by using scan mirrors. Two arrows represent the scanning directions of the focus over the specimen. A fraction of fluorescence (green) is collected by the same objective lens. Fluorescence is separated from the excitation light by a dichroic mirror and then imaged onto the detector by a tube lens. Only fluorescence emitted from the immediate vicinity of the focal region passes through the pinhole.

2.3 Image formation

This section focuses on the fundamental principle of image formation, which can be broadly categorized into two types: coherent and incoherent imaging. Since this thesis solely pertains to fluorescence imaging, the discussion will only be relevant to incoherent imaging.

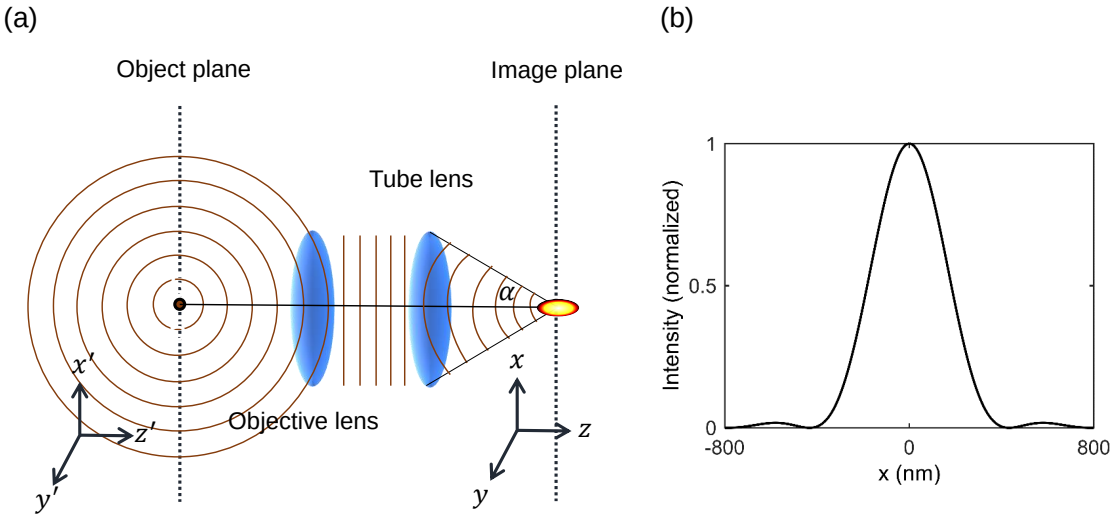

Figure 2.3: (a) Image formation of a point-like object by an objective lens and tube lens. Object at the focal plane of the objective lens generates light with a spherical wave front. The objective lens collects a fraction of this light and converts it into a plane wave. This plane wave is then intercepted by the tube lens and focused onto the image plane. However, due to the finite range of wavelets involved in the image formation process, the resulting image is not a point, but a smeared spot with a characteristic intensity distribution known as the PSF. (b) The plot shows the intensity as a function of x, and has been generated using Eq. 2.5. The parameters used in the equation are a wavelength of $640nm$, a *NA* of 1.20, and a refractive index of 1.33.

A point-like object located at $\vec{r'} = (x', y', z')$ emits light at a vacuum wavelength of λ_0 and imaged to a point $\vec{r} = (x, y, z)$ in the image plane by two identical, infinity-corrected lenses that form an ideal, aplanatic imaging system, as shown in Fig. 2.3(a). The point (x', y', z') is positioned at the focal plane of the objective lens. The point object generates the light with a spherical wavefront. The objective lens collects a portion of the spherical wavefront and converts it into a plane wave, which is intercepted by the tube lens. The tube lens reshapes the plane wavefront into a converging spherical wave, which is then focused onto the image plane.

The electric field distribution around the point $\vec{r} = (x, y, z)$ is known as amplitude PSF,

which can be calculated following scalar diffraction theory [23, 24],

$$h_A(\vec{r}) = \int_0^{\alpha} \sqrt{\cos\phi}\ \sin\phi\ J_0(k\sqrt{x^2+y^2}\sin\phi)\ \exp(i\,k\,z\cos\phi)\ d\phi \tag{2.4}$$

where k is the wave number which is given by $k = \frac{2\pi n}{\lambda_0}$, n being the refractive index. J_0 denotes the 0$^{\text{th}}$ order Bessel function of first kind. ϕ is the polar angle that ranges from 0 to α. α is the half of the maximum angle of the light cone that can enter or exit the objective lens. By applying the paraxial approximation, the integration presented in Eq.2.4 can be solved, allowing for the determination of the lateral intensity distribution at $(x, y, z = 0)$, which is commonly known as the Airy function [24],

$$h_{PSF}(x,y,0) = |h_A(x,y,z=0)|^2 = \left| 2\,\frac{J_1(k\sqrt{x^2+y^2}\sin\alpha)}{k\sqrt{x^2+y^2}\sin\alpha} \right|^2 \tag{2.5}$$

and the intensity distribution along z axis is given by,

$$h_{PSF}(0,0,z) = |h_A(x=0,y=0,z)|^2 = \left| \frac{\sin(\frac{k}{4}z\sin^2\alpha)}{\frac{k}{4}z\sin^2\alpha} \right|^2 \tag{2.6}$$

J_1 represents 1$^{\text{st}}$ order Bessel function of 1$^{\text{st}}$ kind. Fig. 2.3(b) displays the simulated intensity distribution in the x direction at $y = 0$ and $z = 0$ following Eq.2.5. The plot is generated using a wavelength of $640nm$, $NA = 1.20$ and a $n = 1.33$.

In general, the central lobe of the Airy pattern can be approximated as a Gaussian function. Half of the maximum intensity of the central lobe of the Airy disk, where $2\,\frac{J_1(k\,x\sin\alpha)}{k\,x\sin\alpha} = \frac{1}{\sqrt{2}}$ [25], occurs at $k\,x\,\sin\alpha = 1.616$ in x direction. Substituting $k = \frac{2\pi\,n}{\lambda_0}$ and $n\sin\alpha = NA$, the full width at half maxima (FWHM) of the central lobe of the Airy disk turns out to be,

$$\Delta x = 0.51\ \frac{\lambda_0}{NA} \tag{2.7}$$

and along z axis,

$$\Delta z = 1.77\ \frac{n\,\lambda_0}{NA^2} \tag{2.8}$$

When the distance between two point-like objects becomes smaller than Δx, they cannot be resolved as separate images. Therefore, FWHM of the PSF is a convenient measure for defining the resolution of a microscope. To determine the resolution in a confocal

microscope, it is necessary to consider the effects of diffraction and the generation of PSF for both the excitation and detection beams. The introduction of a pinhole in confocal microscopy makes sure that signal only from the focal region is detected. In practice, this is equivalent to image the pinhole to the focal plane. This image is called detection PSF, $h_{det}(\vec{r})$ which represents the probability of detecting a fluorescence photon at $\vec{r}$. Therefore, the effective PSF of a confocal microscope (h_{conf}) is given by the probability of exciting a fluorophore, represented by $h_{exc}(\vec{r})$, multiplied by the probability of detecting its fluorescence signal, represented by $h_{det}(\vec{r})$. $h_{exc}(\vec{r})$ and $h_{det}(\vec{r})$ represents excitation PSF and detection PSF, respectively.

$$h_{conf}(\vec{r}) = h_{exc}(\vec{r}) \cdot h_{det}(\vec{r}) \tag{2.9}$$

Usually, h_{det} is defined for an infinitesimally small pinhole. However, in order to collect sufficient amount of signal the pinhole must have a finite size that can be described by a pinhole function, $p(\vec{r})$. Mostly, a pinhole function is described by [23],

$$p(\vec{r}) = p(x, y, z = 0) = \begin{cases} 1, & \text{if } \sqrt{x^2 + y^2} \leq a \\ 0, & \text{otherwise} \end{cases}$$

where a is the radius of the pinhole. In this case, $h_{det}(\vec{r})$ is modified by the real detection PSF, $h_{real,det}(\vec{r})$ and is given by the convolution of $h_{det}(\vec{r})$ with $p(\vec{r})$.

$$h_{real,det}(\vec{r}) = \int_{-\infty}^{\infty} h_{det}(\vec{r'})\, p(\vec{r} - \vec{r'})\, d\vec{r'} \tag{2.10}$$

2.4 Working principle of STED microscopy

In STED microscopy, fluorescence is inhibited via stimulated emission. This is achieved by overlapping the Gaussian excitation focus with a laser beam, which is referred to as the STED laser beam. The STED laser beam has an intensity distribution that features zero intensity at its center. As a result, fluorescence is confined to the central region of the STED focus. The STED laser can be operated in either continuous mode or pulse mode, both of which enable resolution enhancement. When using a pulsed STED laser, it is

necessary to employ a pulsed excitation laser as well. In this thesis, STED microscopy is implemented using both pulsed STED and excitation lasers. Therefore, only this particular case is discussed in the following section.

2.4.1 Depletion of fluorescence

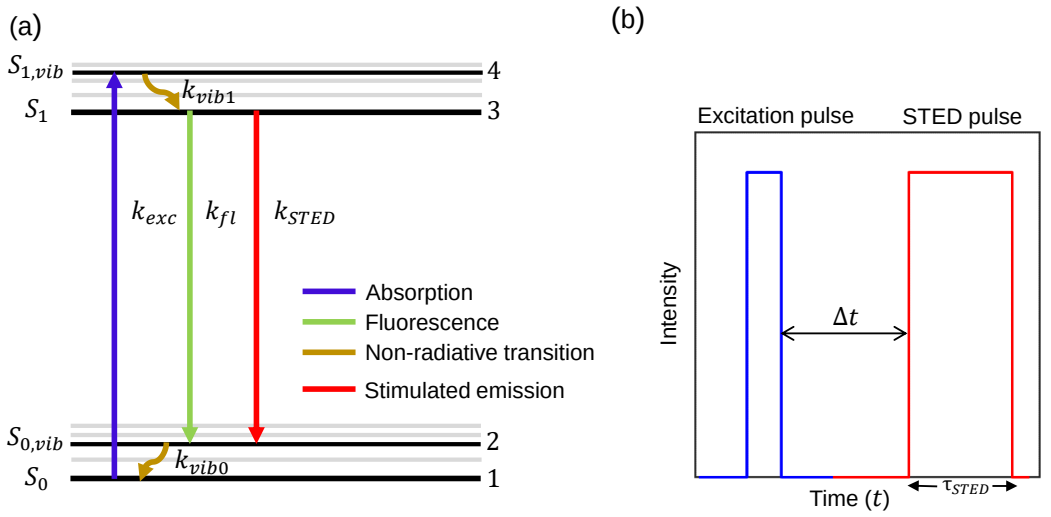

Figure 2.4: (a) Simplified Jablonski diagram illustrates a 4-level system of a fluorescent molecule which includes electronic states and corresponding vibrational states, S_0, $S_{0,vib}$ and S_1, $S_{1,vib}$ denoted by level $1, 2, 3, 4$, respectively. When molecules absorb light, they are excited from the electronic ground state, S_0, to the excited state, $S_{1,vib}$. After undergoing a non-radiative transition to state, S_1, with a rate constant, k_{vib1} molecules can either emit fluorescence spontaneously or be forced down to state, $S_{0,vib}$ through stimulated emission. Following another non-radiative transition with rate constant k_{vib0}, molecules relax back to ground state, S_0. The rate constants for absorption, spontaneous emission, and stimulated emission are denoted by k_{exc}, k_{fl}, and k_{STED}, respectively. (b) Schematic of excitation light pulse (blue) and STED light pulse (red) are shown. Δt represents the time delay between the two pulses and τ_{STED} represents the STED pulse width.

Depletion of fluorescence is done by STED laser beam having a wavelength at the red end of the emission spectrum of the fluorophore molecule. The efficiency of the depletion plays a vital role for the performance of a STED microscope. The interplay of the excitation light and the STED light can be explained using rate equations and by modelling the fluorophore as a 4-level system as shown in Fig. 2.4(a). N_1, N_2, N_3, N_4 represents the number of fluorescent molecules at the level 1,2,3,4, respectively, and k represents the rates of transition from one level to another. Molecules staying at level 3 contributes to the fluorescence. Finding a fluorescent molecule at level 3 is governed by the following

rate equation [1],

$$\frac{dN_3}{dt} = -k_{fl}\, N_3 - k_{STED}\, N_3 + k_{STED}\, N_2 + k_{vib1}\, N_4 \tag{2.11}$$

where, k_{fl} and k_{vib1} represent the rate constant for fluorescence decay from S_1 and vibrational decay from $S_{1,vib}$. As vibrational relaxation is very fast, N_2 and N_4 are much smaller as compared to N_1 and N_3 [7]. Therefore, the last two terms in Eq. 2.11 can be ignored. Solving Eq. 2.11 gives,

$$N_3(t) = N_3(0)\, e^{-(k_{fl}+k_{STED})t} \tag{2.12}$$

where, $N_3(0)$ is the number of molecules at level 3 at time, $t = 0$. Substituting $\frac{1}{k_{fl}} = \tau_{fl}$, Eq. 2.12 turns out to be,

$$N_3(t) = N_3(0)\, e^{-\frac{t}{\tau_{fl}}}\, e^{-k_{STED}\, t} \tag{2.13}$$

where, τ_{fl} represents the fluorescence lifetime. The stimulated emission rate must be greater than the fluorescence emission rate, $k_{STED} >> \frac{1}{\tau_{fl}}$, in order to effectively inhibit fluorescence. To find the dependency of depletion on the applied STED light intensity, the number of molecules, $N_3(\tau_{STED})$, that remain at level 3 after being exposed to one STED pulse with a pulse width τ_{STED} are to be determined:

$$N_3(\tau_{STED}) = N_3(0)\, e^{-\frac{\tau_{STED}}{\tau_{fl}}}\, e^{-k_{STED}\, \tau_{STED}} \tag{2.14}$$

Here, it is assumed that the STED pulse follows the excitation pulse with no delay. The rate of transition for stimulated emission induced by a STED laser pulse can be expressed as,

$$k_{STED} = \sigma_{STED}\, \frac{j}{\tau_{STED}},$$

where σ_{STED} is the stimulated emission cross-section, which represents the probability of the particular transition and j is the number of photons with frequency ν_{STED} per area and per pulse. Thus,

$$N_3(\tau_{STED}) = N_3(0)\, e^{-\frac{\tau_{STED}}{\tau_{fl}}}\, e^{-\sigma_{STED}\, j} \tag{2.15}$$

As $\tau_{STED} << \tau_{fl}$, effectively Eq. 2.15 can be simplified as,

$$N_3(\tau_{STED}) = N_3(0)\, e^{-\sigma_{STED}\, j} \tag{2.16}$$

With the saturation photon fluence per pulse j_{sat}, at which the initial fluorescence is reduced by half, $j_{sat} = \frac{\ln(2)}{\sigma_{STED}}$ Eq. 2.16 can be written as,

$$N_3(\tau_{STED}) = N_3(0)\, e^{-\ln(2)\,\frac{j}{j_{sat}}} \tag{2.17}$$

Eq. 2.17 can be rewritten in terms of average pulse intensity, I and saturation pulse intensity, I_{sat},

$$N_3(\tau_{STED}) = N_3(0)\, e^{-\ln(2)\,\frac{I}{I_{sat}}} \tag{2.18}$$

In experimental setups, it is easier to measure the average STED light power than to obtain information about the local STED intensity. When rewriting Eq. 2.17 in terms of measurable power, it is important to take into account the spatial dependence of j which reflects the lateral shape of the STED light focus.

$$j(x,y) = m\, h_{STED}(x,y), \tag{2.19}$$

where m is the number of photons per pulse and $h_{STED}(x,y)$ represents the focal distribution of a single photon per pulse with $\int\int h_{STED}(x,y)\, dx\, dy = 1$. If R is the repetition rate of the pulsed laser, the measurable average power of the STED laser beam can be written as [23],

$$P_{STED} = m\, h\, \nu_{STED}\, R, \tag{2.20}$$

where ν_{STED} is the frequency of the STED photon and h is the Plank's constant. Using Eq. 2.16, Eq. 2.19, and Eq. 2.20,

$$\begin{aligned} N_3(\tau_{STED}, x, y) &= N_3(0, x, y)\, e^{-\sigma_{STED}\, j(x,y)} \\ &= N_3(0, x, y)\, e^{-\frac{\sigma_{STED}\, P_{STED}}{R\, h\, \nu_{STED}}\, h_{STED}(x,y)} \end{aligned} \tag{2.21}$$

Eq. 2.21 shows that fluorescence intensity which is proportional to the number of molecules in S_1 is depleted by a factor, $\eta(x, y)$.

$$\begin{aligned} \eta(x,y) &= e^{-\frac{\sigma_{STED}\, P_{STED}}{R\, h\, \nu_{STED}}\, h_{STED}(x,y)} \\ &= e^{-\frac{\ln(2)\, P_{STED}}{j_{sat}\, R\, h\, \nu_{STED}}\, h_{STED}(x,y)} \end{aligned} \tag{2.22}$$

Analytic expression of the saturation power, P_{sat} can be written as,

$$P_{sat} = \frac{j_{sat}\, R\, h\, \nu_{STED}}{h_{cal(0,0)}}, \tag{2.23}$$

Here, $h_{cal}(x, y)$ is the focal distribution of the beam used in an experiment to measure the saturation power by scanning the focus over very small beads. P_{sat} refers the amount of STED light power needed to reduce the fluorescence at the center of the bead by half [26]. Therefore, the depletion factor takes the form,

$$\eta(x,y) = e^{-\ln(2)\, \frac{P_{STED}}{P_{sat}}\, \frac{h_{STED}(x,y)}{h_{cal}(0,0)}} \tag{2.24}$$

Therefore, increasing the power of STED light enhances the depopulation of the excited level 3 contributing to improved resolution. In a pulsed STED microscope, STED pulse follows the excitation light pulse within a time interval of Δt, as shown in Fig. 2.4(b). The STED pulse length, τ_{STED} must be shorter than the fluorescence lifetime, τ_{fl} to make the most effective use of the available STED photons. At the same time, τ_{STED} must be longer than the vibrational lifetime to allow for effective depletion. The excitation pulse width has not a major role to play as long as it is much shorter than the fluorescence lifetime.

To ensure optimal performance of STED microscopy, it is important to carefully choose the relative timing, denoted by Δt between the excitation and STED pulses. The relative timing refers to the difference in time between the absolute arrival of the STED pulse and the excitation pulse, which is expressed as $\Delta t = t_{STED} - t_{exc}$. A positive value of Δt indicates that the STED pulse arrives at the sample after the excitation pulse. If Δt is negative, there is a chance that some of the STED light or the entire STED light incidents on the sample even before the excitation light reaches and also there should be enough time for vibrational relaxation from $S_{1,vib}$ to S_1. Whereas, if Δt is too long the depletion

of fluorescence will be lower because the STED pulse will reach the sample too late. This means that some of the molecules will already have emitted fluorescence before the STED pulse can deplete their excited state population.

STED light must have the wavelength corresponding to the energy gap for the transition from S_1 to $S_{0,vib}$. However, STED light can also excite the molecules from S_0 which can contribute to the background of the image and jeopardize the resolution improvement. Therefore, to maximize the stimulated emission and minimize the excitation the wavelength of the STED light is shifted to the red end of the emission spectrum of the fluorophore.

2.4.2 Shape of the PSF of STED beam

The intensity profile of STED light in the focal plane of the objective lens is such that, $I_{STED}(r) = I_{max}\, f(r)$, where I_{max} is the maximum intensity of the STED light and $f(r)$ is a continuous and differentiable function describing the radial profile such that at $r = 0$, $f(r) = 0$ which means a beam profile has to be formed that has zero intensity at the geometric focus and higher intensity surrounding it. Therefore, towards the focal center, as $r \to 0$ there is less and less effect of STED laser induced stimulated emission. In practice, such $f(r)$ can be realized by making the STED laser beam profile doughnut shaped. This can be achieved by passing the STED beam through a circular π-phase plate (π*PP*) or a vortex phase plate (*VPP*).

A π*PP* can be realized by inserting a $\frac{\lambda}{2}$ phase plate producing π phase shift at the central region of a circular aperture [27] as shown in Fig. 2.5(a). The phase distribution of a π*PP* can be expressed as,

$$A(\rho,\phi) = \begin{cases} e^{i\pi}, & \text{if } \rho > r_0 \\ 1, & \text{if } \rho \leq r_0, \end{cases} \qquad \phi = [0....2\pi]$$

where, (ρ, ϕ) is the polar coordinate in the pupil plane, with ρ being the normalized radial coordinate. r_0 is the $\frac{1}{\sqrt{2}}$ times of the diameter of the pupil of the objective lens used [23]. The portion of the beam passing through the center region of a π*PP* would form a relatively larger intensity distribution due to the low effective *NA* and the part of the beam

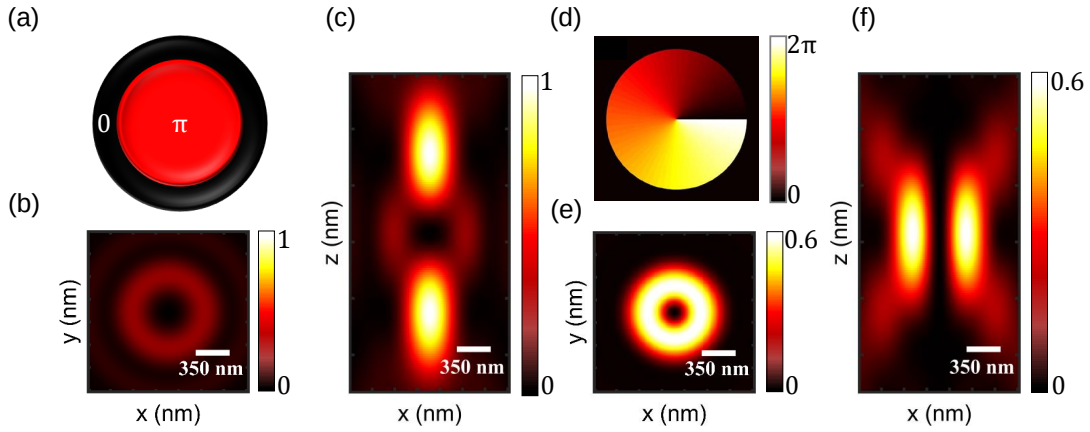

Figure 2.5: (a) Schematic of a π*PP*. It works by introducing a phase delay of π between the light passing through the central and outer regions of the aperture, which causes destructive interference at the focus center. Regions of constructive interference occur above and below the focus. (b) simulated PSF in lateral direction and (c) axial direction formed by a π*PP* illuminated by circularly polarized light at wavelength of $775nm$. An oil immersion objective lens with *NA* $= 1.35$ is used. (d) Schematic of a *VPP*. It's structure consists of a spiral phase ramp that varies from 0 to 2π. When light passes through a *VPP*, two opposite points experience a phase difference of π, causing destructive interference at the focus center. (e) simulated PSF in lateral direction and (f) axial direction formed by a *VPP* illuminated by circularly polarized light at wavelength of $775nm$. An oil immersion objective lens with *NA* $= 1.35$ is used. Using a *VPP* does not confine the fluorescence emission in the axial direction.

passing through the outer region would form a relatively smaller intensity distribution because of the higher effective *NA*. Both the electric field distributions are added coherently, resulting in a central intensity minimum by interfering destructively due to their π phase shift. As a result, an extended PSF is created along the axial direction, featuring a central dark zone at the geometric focus and bright lobes above and below. The PSF along the axial direction, $(x, 0, z)$ formed by a π*PP* is shown in Fig. 2.5(c). In Fig. 2.5(b), the PSF of a STED beam at the focus in the lateral direction is depicted, also created by a π*PP*. While π*PP* remarkably enhances the resolution along the optic axis, a *VPP* leads to a significant resolution improvement in the lateral direction [28]. The structure of *VPP* is composed like a helical staircase where each stair introduces different phase to the transmitted beam following the equation,

$$A(\rho, \phi) = e^{i\phi} \qquad \phi = [0...2\pi]$$

with a rotational symmetry as shown in Fig. 2.5(d). Every ray passing through a *VPP* ex-

periences a π-shifted counterpart and interferes destructively forming a central minimum as shown in Fig. 2.5(f). Fig. 2.5(e) shows the PSF of a STED beam at the focus in the lateral direction formed by a *VPP*.

Objective lenses with high *NA* require consideration of the polarization of light. In particular, the radial components of the electric field at the back aperture of the objective lens can cause an undesired contribution of axial fields that interfere constructively at the focus. One solution to this problem is to use circular polarization with circularity matches with the helicity of the *VPP* of the incoming beam to balance the z components of the electric field on the optic axis with an opposing field of equal magnitude. This ensures that axial fields cancel out, resulting in a zero intensity at the focus.

2.4.3 Resolution of a STED microscope

In STED microscopy, resolution manifests the spatial extension of the region which is still active to emit fluorescence. Here, the resolution improvement is explained in the lateral plane.

The PSF of the excitation beam is well approximated as a Gaussian function with a FWHM of $\Delta r_{exc} \sim \frac{\lambda}{2\,NA}$ as in Eq. 2.7.

$$h_{exc}(r) = e^{-4\,\ln(2)\,\frac{r^2}{\Delta r_{exc}^2}} \tag{2.25}$$

A parabolic function can adequately describe the proximity of the focal center of the STED beam's PSF,

$$h_{STED}(r) = 4\,a\,I_{STED}\,r^2 \tag{2.26}$$

where I_{STED} is the maximum STED beam intensity in the focal plane and a determines the steepness of the parabola [29]. The resultant PSF of the STED microscope, $h_{eff}(r)$ is expressed as,

$$h_{eff}(r) = h_{exc}(r)\,\eta(r) \tag{2.27}$$

where $\eta(r)$ is the remaining fluorescence in the presence of the STED light. Following Eq. 2.24, $\eta(r) = e^{-\ln(2)\frac{I_{STED}(r)}{I_{sat}}}$, here $I_{STED}(r)$ is the distribution of STED light intensity.

$$\begin{aligned} h_{eff}(r) &= e^{-4\ \ln(2)\ \frac{r^2}{\Delta r_{exc}^2}}\ \ e^{-\ln(2)\ \frac{4\ a\ I_{STED}\ r^2}{I_{sat}}} \\ &= e^{-4\ \ln(2)\ r^2(\frac{1}{\Delta r_{exc}^2}+\frac{a\ I_{STED}}{I_{sat}})} \end{aligned} \tag{2.28}$$

Therefore, from Eq. 2.28 the effective FWHM in the lateral direction of a STED microscope is,

$$\Delta r_{STED} = \frac{\Delta r_{exc}}{\sqrt{1 + a\ \Delta r_{exc}^2\ \frac{I_{STED}}{I_{sat}}}} \tag{2.29}$$

A parameter I_{sat}^* can be defined as, $I_{sat}^* = \frac{I_{sat}}{a\ \Delta r_{exc}^2}$. Eq. 2.29 can be written as

$$\Delta r_{STED} = \frac{\lambda}{2\ NA\ \sqrt{1 + \frac{I_{STED}}{I_{sat}^*}}} \tag{2.30}$$

According to Eq. 2.30 increasing I_{STED}, in principle, an arbitrarily small Δr_{STED} can be achieved. Thus, the resolution of the STED microscope is not fundamentally limited by diffraction, but rather by how well the theoretical conditions underlying Eq. 2.30 can be implemented in practice. Additionally, the largest value of I_{STED} that can be used in imaging is limited by the specimen's ability to tolerate high levels of light without being damaged.

2.5 Aberration

An ideal imaging system should display a one-to-one correspondence between points in the object plane and the image plane, meaning that all rays emanating from a given point in the object plane should converge precisely at the corresponding point in the image plane. However, in reality, such an ideal optical system does not exist, leading to deviations from perfect correspondence known as aberrations.

A point-like object in an ideal imaging system produces a spherical wavefront *AB* at the exit pupil of the objective lens, with a radius of curvature *R* as shown in Fig. 2.6. The center of the back focal plane of the objective lens is positioned at the origin of the coordinate system (x, y, z) with polar coordinates (ρ, ϕ), where ρ is the normalized radial coordinate,

$\rho = \frac{\sqrt{x^2+y^2}}{a}$, a being the radius of the exit pupil of the objective lens. The center of curvature of *AB* coincides with the origin of the coordinate system of the image plane (x_0, y_0, z_0). Suppose that, imperfections are introduced to the imaging system, causing the wavefront to deviate from its ideal spherical shape. The deviated wavefront is shown by *A'B'* in Fig. 2.6.

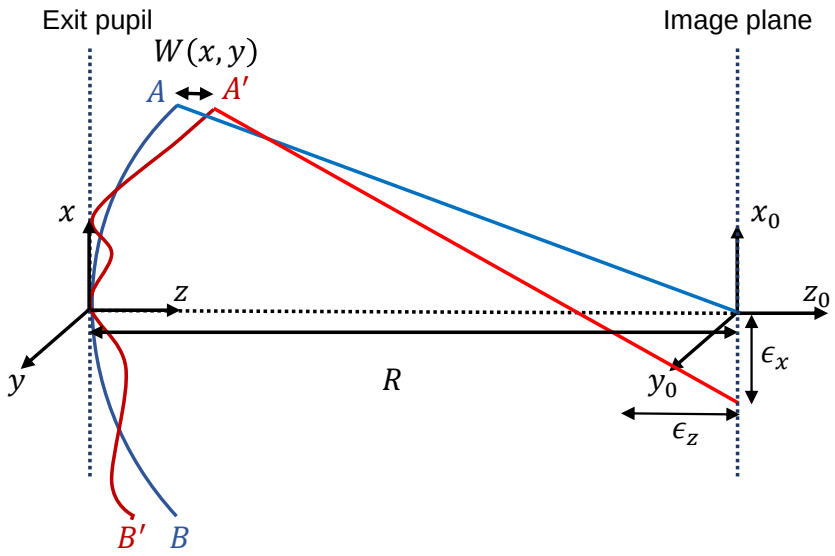

Figure 2.6: Wave aberration function for a point-like object represented in the (x, y, z) coordinate system of the exit pupil of the objective lens, with the image plane represented by (x_0, y_0, z_0). Under ideal imaging conditions, a spherical wavefront *AB* (blue) with a radius of curvature R is produced at the exit pupil. However, in reality, the actual wavefront *A'B'* (red) deviates from the ideal wavefront, with $W(x, y)$ representing the aberration function defined as the distance between the ideal and actual wavefront. This aberration causes different parts of the actual wavefront to focus at different points, resulting in an aberrated image.

An aberration function can be defined as $W(x, y)$ that represents the optical path length from the reference wavefront *AB* to the actual wavefront *A'B'* at the exit pupil along the ray [24]. A ray from *A'B'* intersect the image plane at a point (ϵ_x, ϵ_y).

The standard way to describe the aberration function is to expand in a series [24, 30, 31]. The rotational symmetry about the z axis of the optical system shown in Fig. 2.6 implies that $W(x, y)$ is a function of three variables that are invariant under rotation, namely $x^2 + y^2 = \rho^2$, ϵ_x^2, $x \cdot \epsilon_x + y \cdot \epsilon_y$ [31]. The radius of the pupil of the objective lens is considered as 1. The image point can be placed on the x_0 axis by assuming, without loss of generality,

that $\epsilon_y = 0$. Therefore, the expansion of W in polar coordinate is,

$$W(\rho^2,\, \epsilon_x \rho \cos\phi,\, \epsilon_x^2) = b_1\, \epsilon_x^2 + b_2\, \epsilon_x\, \rho \cos\phi + b_3\, \rho^2 + b_4\, \rho^4 + b_5\, \epsilon_x\, \rho^3 \cos\phi + b_6\, \epsilon_x^2\, \rho^2 \cos^2\phi + b_7\, \epsilon_x^2\, \rho^2 + b_8\, \epsilon_x^3\, \rho \cos\phi \cdots \tag{2.31}$$

Each terms in Eq. 2.31 represents a specific type of aberration with a corresponding coefficient, b_n. These aberrations include piston, tilt, defocus, primary spherical, coma, astigmatism, respectively.

However, the power series expansion as given in Eq. 2.31 is not always the most efficient method for fitting experimental data. When integrating over the entire exit pupil, it is often more appropriate to expand the aberration function in terms of a complete set of orthogonal polynomials that are defined over the circular pupil. One well-known set of such polynomials is the Zernike basis, introduced by F. Zernike [32].

2.5.1 Zernike polynomial expansion

Zernike polynomials are an infinite set of polynomials in two variables, ρ and ϕ. Zernike polynomials exhibit rotational symmetry and are defined as [33].

$$Z_n^m(\rho,\phi) = \begin{cases} \sqrt{2(n+1)}\, R_n^m(\rho)\, \cos(m\phi) & \text{for } m > 0; \\ \sqrt{2(n+1)}\, R_n^m(\rho)\, \sin(m\phi) & \text{for } m < 0; \\ \sqrt{n+1}\; R_n^0(\rho) & \text{for } m = 0. \end{cases} \tag{2.32}$$

Here, n and m are integer. n and m are such that $n \geq m$ and $n - |m|$ =even.

$R_n^m(\rho)$ is expressed as,

$$R_n^m(\rho) = \sum_{k=0}^{\frac{n-|m|}{2}} \frac{(-1)^k\,(n-k)!}{k!\,(\frac{n+m}{2}-k)!\,(\frac{n-m}{2}-k)!}\, \rho^{n-2k} \tag{2.33}$$

The prefactor in Eq. 2.32 is determined by the orthogonality and normalization properties of the Zernike polynomials over the unit pupil radius, which are described by the following equations [24, 33],

$$\int_0^1 \int_0^{2\pi} Z_n^m(\rho,\phi)\, Z_{n'}^{m'}(\rho,\phi)\, \rho\, d\rho\, d\phi = \pi\, \delta_{mm'}\, \delta_{nn'}$$

$$\int_0^{2\pi} \cos(m\phi)\, \cos(m'\phi)\, d\phi = \pi\,(1+\delta_{m0})\, \delta_{mm'}$$

$$\int_0^1 R_n^m(\rho)\, R_{n'}^m(\rho)\, \rho\, d\rho = \frac{\delta_{nn'}}{2(n+1)}$$

Here, δ is defined as,

$$\delta_{ij} = \begin{cases} 1, & \text{if } i = j, \\ 0, & \text{if } i \neq j. \end{cases}$$

Any arbitrary aberration function, $W(\rho,\phi)$ can be decomposed into a sum of Zernike polynomials with appropriate coefficients,

$$W(\rho,\phi) = \sum_{n=0}^{\infty} \sum_{m=0}^{n} C_{nm}\, Z_n^m(\rho,\phi) \tag{2.34}$$

Using Eq.2.33, Eq. 2.34 can be conveniently written as,

$$W(\rho,\phi) = C_{00} + \sum_{\substack{n=2 \\ n \text{ even}}}^{\infty} \sqrt{n+1}\, C_{n0}\, R_n^0(\rho) + \sum_n \sum_m \sqrt{2(n+1)}\, C_{nm}\, Z_n^m(\rho,\phi) \tag{2.35}$$

Following Eqs. 2.32,2.33, some orthonormal Zernike polynomials along with the corresponding names of the aberrations associated with them are presented in table 2.1. The index j represents the Noll index [33]. Throughout the rest of the thesis, Zernike polynomials will be referred using the Noll index.

There are two commonly used units of measurement for describing the shape of a wavefront surface, peak-to-valley (PV) and root-mean-square (rms). The PV value represents the maximum difference in height between the highest and lowest points of the wavefront, while the rms value is determined by calculating the standard deviation of the wavefront's height relative to a desired, non-aberrated reference wavefront. In this thesis, all aberration amplitudes will be expressed in terms of their rms values.

j	n	m	Normalized Zernike functions	Name of aberrations
1	0	0	1	Piston
2	1	1	$2\rho \cos\phi$	Horizontal tilt
3	1	-1	$2\rho \sin\phi$	Vertical tilt
4	2	0	$\sqrt{3}(2\rho^2 - 1)$	Defocus
5	2	-2	$\sqrt{6}\rho^2 \sin(2\phi)$	Primary astigmatism (O)
6	2	2	$\sqrt{6}\rho^2 \cos(2\phi)$	Primary astigmatism (V)
7	3	-1	$\sqrt{8}(3\rho^2 - 2\rho) \sin\phi$	Primary coma (V)
8	3	1	$\sqrt{8}(3\rho^2 - 2\rho) \cos\phi$	Primary coma (H)
9	3	-3	$\sqrt{8}\rho^3 \sin(3\phi)$	Primary trefoil (O)
10	3	3	$\sqrt{8}\rho^3 \cos(3\phi)$	Primary trefoil (V)
11	4	0	$\sqrt{5}(6\rho^4 - 6\rho^2 + 1)$	Primary spherical
12	4	-2	$\sqrt{10}(4\rho^4 - 3\rho^2) \sin(2\phi)$	Secondary astig. (O)
13	4	2	$\sqrt{10}(4\rho^4 - 3\rho^2) \cos(2\phi)$	Secondary astig. (V)
14	4	-4	$\sqrt{10}\rho^4 \sin(4\phi)$	Primary tetrafoil (O)
15	4	4	$\sqrt{10}\rho^4 \cos(4\phi)$	Primary tetrafoil (V)
17	5	-1	$\sqrt{12}(10\rho^5 - 12\rho^3 + 3\rho) \sin\phi$	Secondary coma (V)
18	5	1	$\sqrt{12}(10\rho^5 - 12\rho^3 + 3\rho) \cos\phi$	Secondary coma (H)
22	6	0	$\sqrt{7}(20\rho^6 - 30\rho^4 + 12\rho^2 - 1)$	Secondary spherical

Table 2.1: The table displays the Zernike polynomials and their associated aberrations, labeled by their Noll index (j). The prefactors of the Zernike functions are normalization constants. The abbreviations H,V, and O represent horizontal, vertical, and oblique, respectively.

2.5.2 Refractive index mismatch induced aberration

In optical microscopy, one of the primary causes of spherical aberration is a difference in refractive index. This difference can occur between the refractive index of the lens immersion medium and the specimen embedding medium, or in the case of a thick biological specimen, due to its heterogeneous tissue composition.

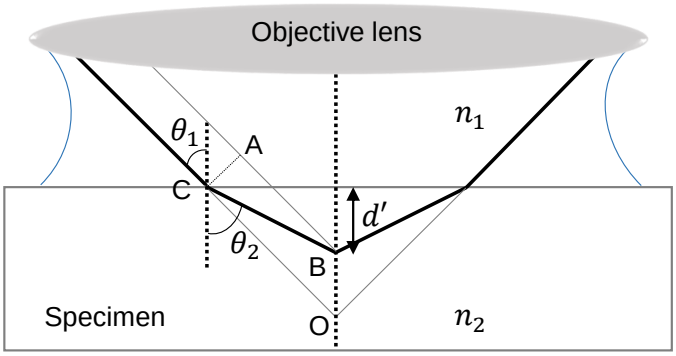

Figure 2.7: The figure illustrates the focusing geometry of an objective lens through an interface between two mediums with refractive indices n_1 and n_2. Light converges precisely at point *O* when n_1 and n_2 are perfectly matched. However, when $n_2 > n_1$, the refractive index mismatch causes the light to converge at a different distance, d' from the interface. The angles of incidence and refraction at the interface between the two mediums are denoted by θ_1 and θ_2, respectively.

Let us consider a scenario where light is focused at a depth d' within the specimen through a medium with a mismatched refractive index, as illustrated in Fig. 2.7. It is important to note that d' refers to the nominal focal position, which is the distance within the specimen when there is no refractive index difference. However, in the presence of refractive index mismatch, the light focuses at a different depth, known as the actual focal position [8]. In such a system, an aberration function $W(\rho, d')$ can be derived [34]. As the light is focused by the objective lens, it encounters an interface between two mediums with different refractive indices, namely n_1 and n_2. The light rays makes an angle of incidence θ_1 and angle of refraction θ_2 at the interface while transitioning from n_1 to n_2. The grey line *AB* in Fig. 2.7 represents the light path in a refractive index-matched system, where $n_1 = n_2$. In contrast, the black line *CB* represents the path of light when $n_2 > n_1$. The difference between the two optical paths, *AB* and *CB*, can be written as [34],

$$W(\rho, d') = n_2(CB) - n_1(AB) \tag{2.36}$$

where, λ is the wavelength of the light. The geometry of Fig. 2.7 allows to write,

$$AB = CB\cos(\theta_2 - \theta_1)$$

$$CB = \frac{d'}{\cos\theta_2}$$

Along with the Snell's law, $n_1 \sin\theta_1 = n_2 \sin\theta_2$ and some trigonometric identities $W(\rho, d')$ can be written as,

$$W(\rho, d') = d'\,(n_2\cos\theta_2 - n_1\cos\theta_1) \tag{2.37}$$

If the objective lens adheres to Abbe's sine condition, a scaled pupil coordinate can be defined as $\rho = \frac{\sin\theta_1}{\sin\alpha}$, where α is half of the maximum angle determined by the *NA* of the objective lens. The value of ρ ranges from 0 to 1 [35]. Using Snell's law, Eq. 2.37 can be written as [34, 36],

$$W(\rho, d') = d'\,n_1\,\sin\alpha\left\{\sqrt{\frac{n_2^2}{n_1^2}\csc^2\alpha - \rho^2} - \sqrt{\csc^2\alpha - \rho^2}\right\} \tag{2.38}$$

As described in section 2.5.1, the aberration function can be expressed as an infinite series of Zernike polynomials. Because $W(\rho, d')$ does not have any angular dependence, it is sufficient to expand it using Zernike polynomials of $m = 0$ [36, 37].

$$W(\rho, d') = d'\,n_1\,\sin\alpha\left\{\sum_{\substack{n=2\\ n\ even}}^{\infty}\sqrt{n+1}\,C_{n0}\,R_n^0(\rho)\right\} \tag{2.39}$$

2.5.3 Effect of aberration

The first four aberration modes, in Table 2.1, namely piston, horizontal tilt, vertical tilt, and defocus, do not significantly affect image quality. Piston is a constant shift of the entire wavefront, while horizontal and vertical tilt represent orthogonal linear phase variations across the pupil of the objective lens, leading to a lateral translation of the image. Defocus causes to an axial shift of the image, which can be easily corrected by refocusing when using a low *NA* objective lens. However, correcting axial shift when using a high *NA* lens is not straightforward, and both defocus and spherical aberration must be manipulated to achieve the correction [38]. Other aberration modes, particularly those of lower order,

present in an optical system affects the shape of the PSF, resulting in a broader distribution and decreased resolution. This aberration-induced spreading of the PSF also causes a reduction in the maximum focal intensity [39]

In an ideal imaging system, Eq. 2.4 describes the amplitude PSF in the focal plane of an objective lens. In the presence of aberration, an additional phase is introduced, resulting in the amplitude PSF,

$$E(\vec{r}) = \int_0^{\alpha} \sqrt{\cos\phi}\, \sin\phi\, J_0(kr\sin\phi)\, \exp ik\{z\cos\phi + W(\rho,\phi)\}\, d\phi \tag{2.40}$$

For a unit radius of the objective lens pupil, the variable $r \equiv \rho$.

To assess the impact of wavefront aberration on image quality, Strehl ratio, S is commonly employed. This ratio compares the intensity value of the central maximum of the PSF of an ideal system to that of an aberrated system, $S = \frac{|h_A(\vec{r}=0)|^2}{|E(\vec{r}=0)|^2}$. Strehl ratio is defined as [40],

$$S = \frac{1}{\pi^2}\left|\int_0^{2\pi}\int_0^{1} e^{\{ikW(\rho,\phi)\}}\rho\, d\rho\, d\phi\right|^2 \tag{2.41}$$

Eq. 2.41 demonstrates that as the magnitude of the aberration function increases, the Strehl ratio decreases.

In STED microscopy, aberration modes can distort the intensity distribution at the focus, while still maintaining a zero intensity. When aberrations are significant in amplitude, the STED resolution enhancement can be compromised because the ring can open up. Some aberration modes can fill in the zero intensity [41], which negate the benefits of resolution enhancement. This occurs because even a small increase in the intensity at the focal center can significantly reduce the fluorescence emission, resulting in a loss of signal-to-noise ratio [42].

Fig. 2.8 demonstrates the impact of various aberrations including $j = 6$, $j = 8$, $j = 10$, $j = 11$, on the PSFs of both Gaussian excitation light and STED light. The PSFs of the Gaussian excitation light are shown in the axial plane, while those of the STED light are shown in the lateral plane, at the focus. These PSFs are generated using a simulation at an excitation wavelength of $640nm$ and a STED wavelength of $775nm$, with an oil immersion objective of *NA* $= 1.35$. The PSFs are calculated by applying phase aberrations with an amplitude, C_{nm} as in Eq. 2.34, of $60nm$ or $60\frac{2\pi\, n}{\lambda}rad$, where λ is

the wavelength of the corresponding light and n is the refractive index of the immersion medium. The PSFs are normalized with respect to the maximum of the PSF with no aberration for the excitation light. In the case of STED PSFs, normalization is carried out with respect to the PSF with astigmatism $(j = 6)$, since astigmatism results in the maximum intensity being concentrated in two lobes.

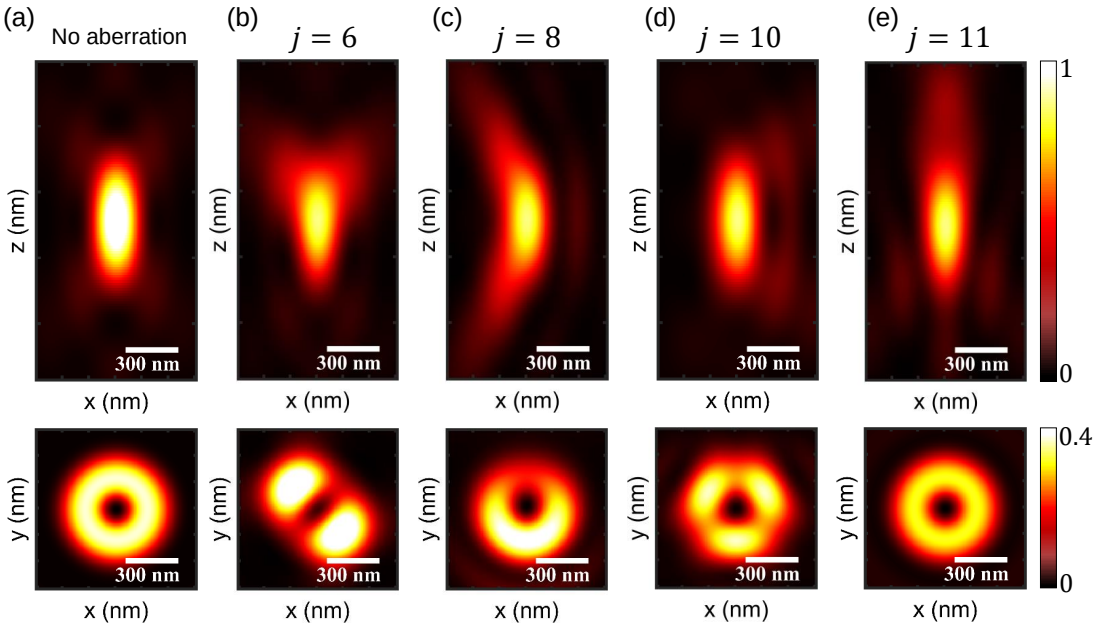

Figure 2.8: Simulated excitation PSFs in xz plane and STED PSFs in xy plane are shown for (a) no aberration and with different aberration modes including vertical primary astigmatism (b), horizontal coma (c), vertical primary trefoil (d), and primary spherical (e). All aberrations have an amplitude of $60nm$. PSFs are simulated using an oil immersion objective lens with *NA* $= 1.35$ at an excitation wavelength of $640nm$ and STED wavelength of $775nm$. Excitation PSFs are normalized with respect to the non-aberrated PSF, and the STED PSFs are normalized with respect to the PSF with $j = 6$.

2.5.4 Aberration correction

In principle, aberration-induced phase can be compensated by introducing an equal and opposite phase into the pupil of the objective lens. This compensation is accomplished using an AO module, which modulates the light wavefront according to the Zernike functions.The amplitudes of the Zernike functions are adjusted based on the types and strength of aberrations present in the optical system. The function of the AO module is to modulate phase of the light wavefront such that the correct phase, $W'(\rho, \phi)$, is introduced into the

objective lens's pupil where,

$$W'(\rho,\phi) = W(\rho,\phi) - \sum_{n=0}^{\infty}\sum_{m=0}^{n} C_{nm}\, Z_n^m(\rho,\phi) \tag{2.42}$$

In an ideal case, $W'(\rho,\phi) = 0$, which means that the aberrations are entirely corrected. However, in practice, there is always a residual amount of aberrations present in the system due to the limitations of the AO module being used. In the next chapter, the limitations of a particular AO module, relevant to this thesis, and its ability to produce Zernike polynomials will be discussed.

The use of AO in microscopy varies depending on how the aberrations are measured. There are two main approaches, direct and indirect measurement schemes. In the direct measurement scheme, a wavefront sensor is used to measure the wavefront, which is then used to set the AO module such that aberrations are minimized [18]. A feedback control system is utilized to link these two elements. However, direct wavefront sensing can be challenging in microscopy due to the complex structure of specimens [13]. The indirect measurement scheme, on the other hand, does not measure the wavefront directly. Instead, typically it optimizes the aberration through a sequence of images. This process iteratively adjusts the wavefront until a certain image metric is optimized. The metrics, commonly used in the indirect optimization approach are total image brightness [4, 19] and sharpness [43, 44]. However, these metrics have some drawbacks. For example, total image brightness can be affected by background signal. In the case of fluorescence imaging, image brightness can decrease due to photo bleaching of the fluorescent molecules which can result in false optimization results. Image sharpness metric by doing Fourier transform of the image has been used [20] but it is highly dependent on the signal-to-noise ratio of the image. To optimize image sharpness, a good signal-to-noise ratio is required. The sharpness metric remains relatively flat near the optimal correction for some aberration modes [20]. This flat maximum indicates that the metric's value only varies significantly for severe aberration amplitudes, rendering it inefficient for correcting aberrations. A metric with a combination of brightness and sharpness has also been used to optimize image quality [17]. However, optimization of such image based metric requires an iterative process that involves acquiring multiple images, computing the metric for each image, and adjusting the AO accordingly. This repetition is necessary until the best im-

age quality is achieved, which can be time-consuming and prone to photo bleaching. To address this issue, a new photon stream-based metric has been introduced recently [5] that allows for fast correction of aberrations in parallel to image acquisition. This new approach, which will be discussed in chapter 4, enables rapid optimization of image quality without the need for repeated image acquisition and the associated drawbacks.

Chapter 3

Experimental setup and characterization

3.1 Experimental setup

The experimental setup for this thesis is grounded in a conventional confocal scanning microscopy configuration. To further improve resolution, a two-color STED microscopy design is incorporated [45]. Fig. 3.1 shows the schematic of the setup. The black dashed box represents an inverted microscope body (IX83, Olympus,Japan). The imaging process is facilitated by using either an oil objective lens ($60X$, 1.35 oil, UPlanSApo, Olympus, Japan) or a water objective lens ($60X$, 1.20 water, $\infty/0.13 - 0.21$, UPlanSApo, Olympus, Japan). The beam delivery to the microscope and detection of the signal from the specimen is accomplished through the optical arrangements positioned at the side of the microscope body. The setup uses two pulsed diode lasers at wavelengths of $640nm$ (LDH-P-C-640B, PicoQuant, Germany) and $560nm$ (PDL 561, Abberior Instruments GmbH, Germany) as excitation beams. A pulsed laser (Abberior instrument GmbH, Germany) at wavelength of $775nm$, with a pulse width of $\sim 940ps$ and repetition rate of 40 MHz is used as a STED laser. Each of the three laser beams is coupled into a separate polarization maintaining, single mode fiber (Schäfter + Kirchhoff GmbH, Germany) and delivered to the setup through the output of the respective fiber. An acousto-optic-modulator, AOM

(MT110, AA Opto Electronic, France) is employed in each beam path to modulate the intensity of the laser beams, enabling each beam to switch on and off pixelwise. STED laser beam is passed through an optical module (Abberior Instruments GmbH, Germany) including a liquid-crystal spatial light modulator, SLM (X13268, Hamamatsu, Germany) in order to provide the intended phase modulation to the STED laser beam. The liquid crystals in the SLM are oriented in such a way that only phase modulation is possible when incident beam is s-polarized. The SLM is placed at the conjugate plane to the back focal plane of the objective lens. The SLM is divided into two parts namely S_1 and S_2. Each of which is configured with a specific phase distribution to generate light intensity in a way that S_1 acts as a *VPP* and S_2 acts as a π*PP*. The working principle of these phase plates are described in section 2.4.2. To enable flexibility in changing the polarization of the incoming STED beam, a half waveplate, M-HWP is mounted on a rotational stage (18PMR-0.5M, SK Advanced, Israel). The STED beam, upon being reflected from S_1 and directed towards S_2, encounters a half waveplate, s-HWP integrated on a mirror, which rotates the polarization of the beam by $90°$. The active area of the s-HWP is suitable for a beam diameter of $2mm$, which is obtained by a combination of lenses, L_1 and L_2, with focal lengths of $16mm$ and $8mm$, respectively. To achieve circular polarization of the STED beam, a quarter waveplate, QWP and a half waveplate, HWP combination is used. In order to entirely illuminate the back aperture of the objective lens, STED beam diameter is expanded by a lens combination of L_3 and L_4 with focal length of $100mm$ and $200mm$, respectively. For $640nm$ excitation beam, a lens combination of L_5 and L_6 with focal length of $10mm$ and $40mm$, respectively and for $560nm$ excitation beam, a lens combination of L_7 and L_8 with focal length of $25mm$ and $100mm$, respectively are used to expand the beam diameters. A dichroic reflector, DIC775 (F$73-750$T, AHF Analysentechnik, Germany) is used to reflect the STED beam towards the microscope. The $640nm$ excitation beam is reflected by a single notch filter, N640 (F$40-658$, AHF Analysentechnik, Germany). The notch filter is designed to transmit specific band at a precise angle of incidence of $0°$. However, in this particular setup, the notch filter is positioned at a slightly different incident angle, which causes it to reflect the $640nm$ beam instead of blocking it. The $560nm$ excitation beam is reflected by a dichroic reflector, DIC560 (F$43-093$, AHF Analysentechnik, Germany).

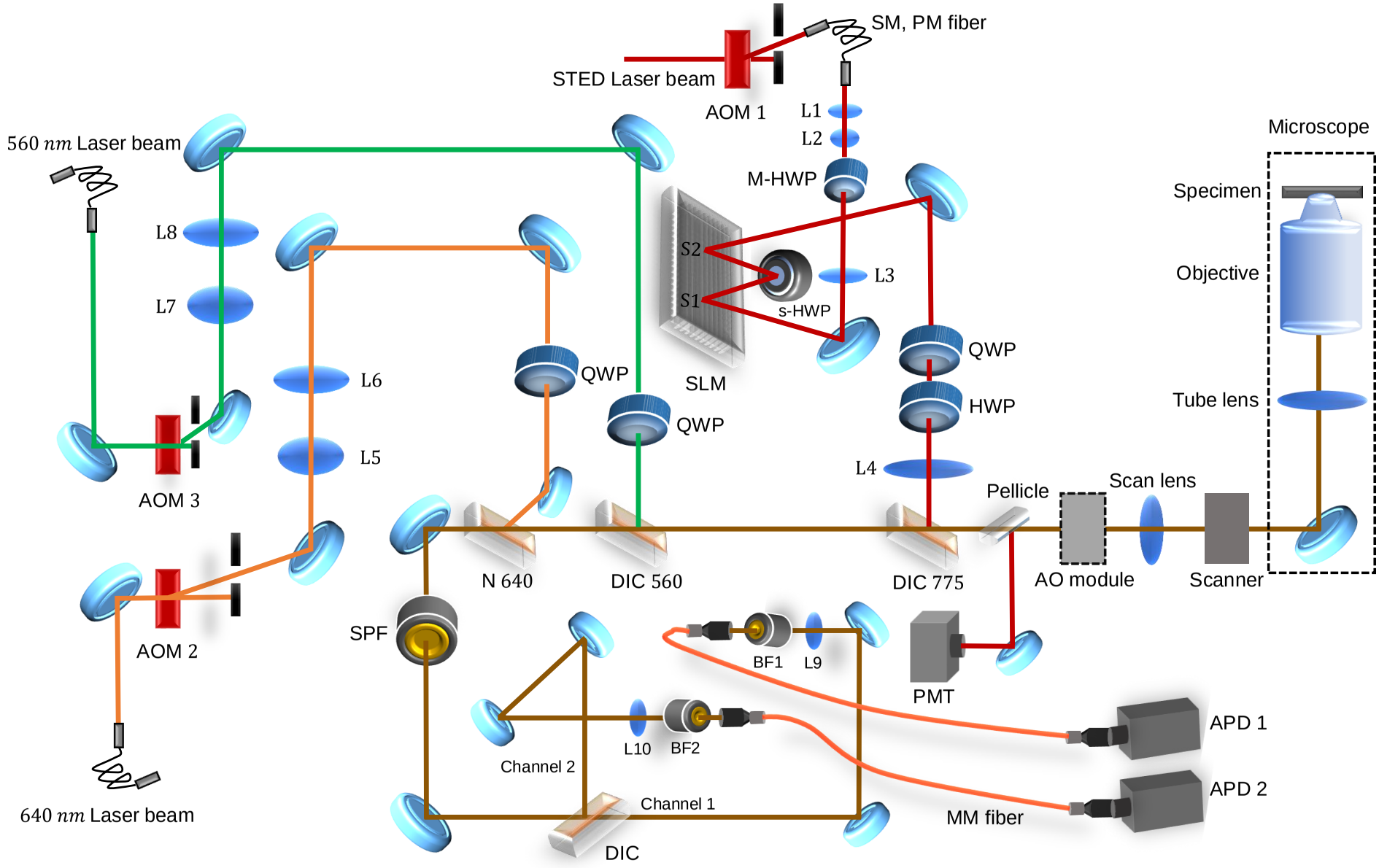
SM, PM fiber
STED Laser beam
AOM 1
L1
L2
M-HWP
Microscope
Specimen
Objective
Tube lens
560 nm Laser beam
L8
L7
L6
L5
AOM 3
AOM 2
640 nm Laser beam
QWP
QWP
SLM
S2
S1
s-HWP
L3
QWP
HWP
L4
Pellicle
Scan lens
AO module
Scanner
N 640
DIC 560
DIC 775
SPF
BF1
L9
PMT
APD 1
APD 2
MM fiber
L10
BF2
Channel 2
Channel 1
DIC

Figure 3.1: Schematic of the experimental setup. AOM1, AOM2, AOM3 is the acousto optic modulator in STED, $640nm$ excitation and $560nm$ excitation beam path, respectively. L_1-L_{10} are the lenses. SM,PM fiber: Single mode, polarization maintaining fiber, MM fiber: Multimode fiber, HWP: half wave plate, QWP: quarter wave plate, M-HWP: Motorized half wave plate, s-HWP: Small half wave plate, SLM: Spatial light modulator, DIC775: Dichroic reflector, transmits at the wavelength range of $400 - 740nm$ and reflects at $780 - 1200nm$. DIC560: Dichroic reflector that transmits at the wavelength range of $610 - 845nm$ and reflects at $500 - 594nm$. N640: Single notch filter that blocks light at wavelength $640 - 680nm$ at an angle of incidence of $0°$. SPF: shortpass filter, transmits at the wavelength range of $380 - 720nm$ and blocks at $750 - 1100nm$. DIC: Dichroic reflector, transmits at the wavelength range of $665 - 800nm$ and reflects at $500 - 643nm$. BF1: bandpass filter 1 at central wavelength of $690nm$ and a bandwidth of $70nm$. BF2: bandpass filter 2 at central wavelength of $623nm$ and a bandwidth of $24nm$. APD: avalanche photodiode, PMT: photomultiplier tube. AO module: Adaptive optics module contains a deformable mirror.

The three beams are combined by the dichroic reflectors and the notch filter and pass through the scan lens and tube lens with focal lengths of $80mm$ and $180mm$, respectively before reaching the specimen through the objective lens. A galvanometer based four mirror scanner (Abberior QUAD scanner, Abberior Instruments GmbH, Germany) is used to move the beam across the specimen, whereas axial scan is done by moving the objective lens along the direction of the beam. The excitation laser diodes and STED laser are synchronized. To facilitate the synchronization, electronic component and microscope control, as well as data acquisition, a field programmable gate arrays based multifunction National Instruments Data Acquisition card (PCIe-6321, National Instruments, US) is utilized along with a software, Imspector (Imspector, Abberior Instruments GmbH, Germany).

When conducting measurements in reflection mode, specifically to align the setup, the reflected light from specimen is directed towards a photomultiplier tube (PMT, H10682 series, Hamamatsu, Germany) using a magnetically attached pellicle beamsplitter.

The fluorescence signal that originates from the specimen is transmitted through DIC775, DIC560 and N640. To separate any residual STED light from the fluorescence a shortpass filter, SPF (F$75 - 750$, AHF Analysentechnik, Germany) is used. A dichroic mirror (F$43 - 643$, AHF Analysentechnik, Germany) is used to separate the spectral detection window into two channels. One channel is designed to detect fluorescence mainly from dyes that are excited by the $640nm$ beam, while the other channel detects fluorescence mainly from dyes excited by the $560nm$ beam. The transmitted arm of the DIC, which

belongs to the $640nm$ excitation, is referred to as channel 1. The reflected arm of the DIC, which belongs to the $560nm$ excitation, is referred to as channel 2. Channel 1 is equipped with a bandpass filter, BF1 (F$49-691$, AHF Analysentechnik, Germany) that selects fluorescence emitted between $655nm-725nm$. Similarly, channel 2 has a bandpass filter, BF2 (F$39-622$, AHF Analysentechnik, Germany) that selects fluorescence emitted between $611nm-635nm$.

Two lenses, $L9$ in channel 1 and $L10$ in channel 2, with a focal length of $120mm$, are used to focus fluorescence onto a multimode fiber (M31L03, Thorlabs, Germany). The fiber has a core diameter of $62.5\mu m$, which serves as a confocal pinhole. The multimode fibers are connected to avalanche photodiode photon counting module, APD (SPCM-AQRH-13-FC, Excelitas, Germany). In Fig. 3.1, there is a black box labeled as the 'AO module'. This box houses a DM, which is currently being used as a static flat mirror. Its potential for correcting aberrations will be further elaborated on in Section 3.2.

3.1.1 Characterization of the setup

Overlapping excitation and STED beams

Achieving optimal STED imaging requires precise lateral overlap of the center of the zero-intensity STED focus with the central maximum of the Gaussian excitation focus, as well as axial overlap. In this context, lateral overlap in the x direction is presented, but axial overlap has also been achieved. To visualize and optimize the lateral overlap, both the excitation and STED light focus are scanned through a single $80nm$ diameter nano-sphere. As the size of the nanosphere is much smaller than the dimension of the light focus used, the detected signal distribution provides a sufficiently accurate approximation for the PSF. For the measurement, a layer of single, sparsely distributed gold beads (Gold colloid, BBI Solutions, Germany) is attached to a poly-L-lysine (Sigma-Aldrich, USA) coated coverslip and embedded in mowiol. The gold beads are illuminated sequentially by the excitation light at a $640nm$ wavelength and the STED light. The reflected light from the beads is directed towards the PMT. A $2D$ image at the focal plane with a FOV of $1.4\mu m$ x $1.4\mu m$ is recorded, with a pixel size of $20nm$ x $20nm$, a $40\mu s$ pixel dwell time, and an excitation light power of $1.5\mu W$ and a STED light power of $9\mu W$ at the back focal plane of the ob-

jective lens. Fig. 3.2(a) and (b) show the signal distribution which resembles the PSF of the excitation and STED light, respectively. Line profiles in the x direction are drawn through the center of the signal distribution for both the excitation and STED light, and the resulting profiles are plotted together in Fig. 3.2(c). The y axis represents the measured photon counts over a duration of $40\mu s$. This plot confirms that the zero-intensity center of the STED focus coincides with the maximum of the Gaussian excitation focus in the x direction. The same verification has been done in the y direction. The lateral FWHM of the excitation light is $\sim 300nm$, which represents the lateral resolution limit of the microscope in confocal configuration. Similar overlap verification has also been done for the $560nm$ excitation light in both the lateral and axial directions.

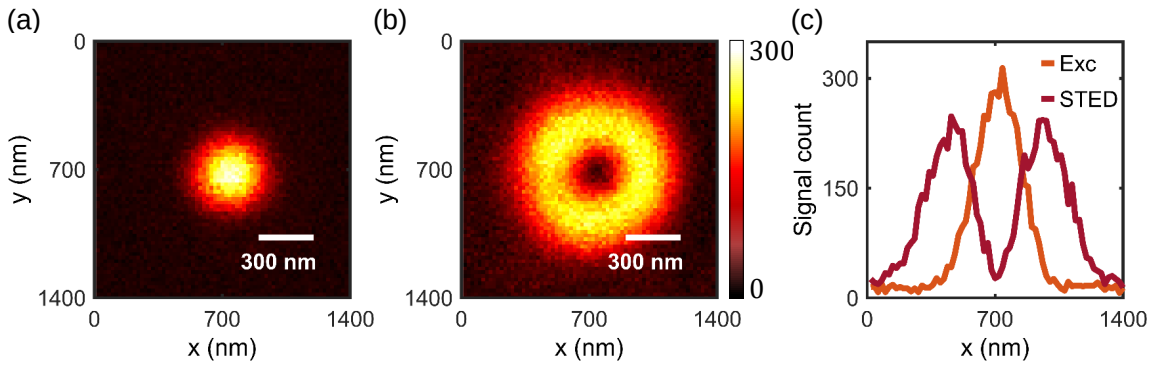

Figure 3.2: The lateral PSFs of (a) $640nm$ excitation light and (b) STED light are measured by detecting the light reflected from gold beads using a PMT. The measurements are performed with an oil objective lens with *NA* $= 1.35$, a pixel size of $20nm$ x $20nm$, a pixel dwell time of $40\mu s$, and excitation and STED light powers of $1.5\mu W$ and $9\mu W$, respectively at the back focal plane of the objective lens. A single colorbar is used to represent the signal intensity for both PSFs. (c) Line profiles along x direction are plotted through the centers of both the PSFs.

Time delay between STED and excitation pulse

In order to set the optimum timing difference, Δt between the arrival times of the STED pulse and excitation pulse at the sample, as explained in section 2.4.1 a homogeneous dye (AD-647N, ATTO-TEC, Germany) dissolved in water with a concentration of $80nM$ is used and the dependency of the fluorescence signal on the timing is analyzed. For these measurements, a water objective lens with *NA* $= 1.20$ is employed. The SLM configuration is set such that no phase modulation is applied on the STED beam, resulting in a Gaussian intensity profile at the focus of the objective lens. Excitation of dye molecules is achieved by illuminating them with excitation light at a wavelength of $640nm$ and a power

of $36\mu W$ at the back focal plane of the objective lens, while fluorescence is depleted by the Gaussian STED beam with a power of $86mW$ at the back focal plane of the objective lens. An APD is used to detect the fluorescence photons.

Since the excitation laser is operated in slave mode and the excitation pulse is electronically triggered by the STED laser's synchronization output signal, the timing difference Δt at the sample can be experimentally easily adjusted by introducing an additional electronic delay $\Delta t'$ to the synchronization signal using the multifunction data acquisition card and the software Imspector. Here, an increasing value of $\Delta t'$ indicates that the excitation pulse is time delayed with respect to the STED pulse. Note that, $\Delta t' = 0$ is set randomly and does not necessarily indicate simultaneous pulse arrival $(\Delta t = 0)$ at the sample. The electronic delay $\Delta t'$ is varied from $-2ns$ to $20ns$ through the software, Imspector and corresponding xy images with a pixel dwell time of $20\mu s$ are recorded. Average photon counts over the same FOV are determined for each $\Delta t'$ and then plotted as a function of $\Delta t'$. If $\Delta t'$ is too large the depletion efficiency of the STED light decreases because

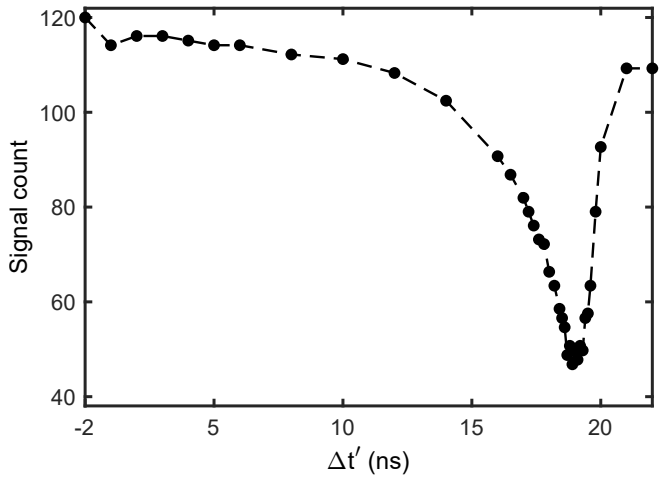

Figure 3.3: Measured fluorescence photons from a dye solution as a function of the electronic delay $\Delta t'$. No phase modulation is applied to the STED beam, resulting in a Gaussian intensity profile at the focus of the objective lens. The measurements are carried out using an water objective lens of *NA* $= 1.20$, with $640nm$ excitation light at a power of $36\mu W$ and Gaussian STED light at a power of $86mW$, with a pixel dwell time of $20\mu s$. Fluorescence signal exhibits a minimum at $16.9ns$, indicating the optimum $\Delta t'$ for the setup.

the excitation pulse has been delayed too much. This means that the STED pulse arrives at the sample before the dye molecules are excited or because they may not have completed the process of vibrational relaxation to reach the lowest energy level of S_1, as shown in Fig. 2.4. This effect is evident on the right side of Fig. 3.3. If $\Delta t'$ is too small,

the depletion efficiency of the STED light also decreases, as the STED pulse reaches the sample too long after the excitation pulse, causing some of the molecules to have already fluoresced. This effect is observed on the left side of Fig. 3.3. The minimum of the fluorescence signal is found to be at electronic delay $\Delta t' = 16.5ns$ for this particular case, representing the optimum timing difference of the pulse arrival times at the sample for the currently used optical and electronical implementation.

2D resolution of the STED microscope

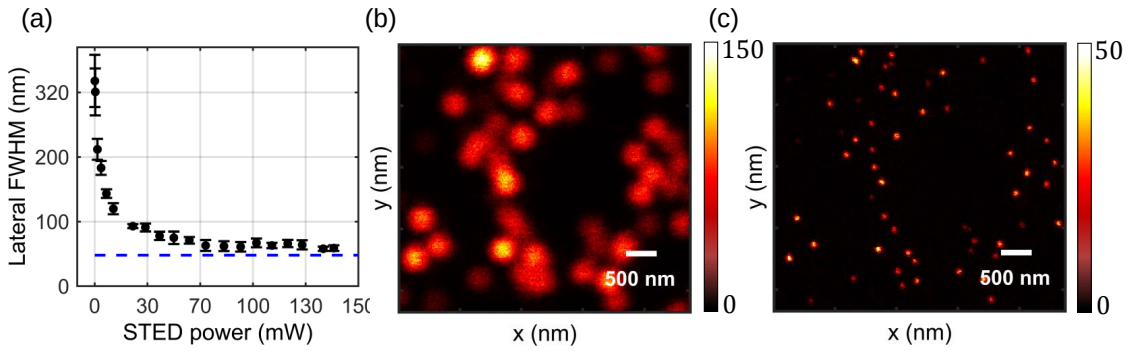

Figure 3.4: (a) $2D$ STED resolution as a function of STED light power, measured using $48nm$ diameter crimson beads, an oil objective lens with $NA = 1.35$, and excitation light at wavelength of $640nm$ with $3.5\mu W$ power at the back focal plane of the objective lens. Varying STED power, xy images are recorded. Line profiles are drawn along the x direction through the center of the beads. To determine the FWHM, three parallel neighboring line profiles are averaged and fitted with a Gaussian function. The lateral FWHM at zero STED power is consistent with that achieved in a confocal configuration. The blue dashed line represents the size of the beads. (b) Confocal image of crimson beads obtained using $640nm$ excitation light and an oil objective lens. (c) Image of same FOV obtained with $2D$ donut shaped STED focus at a power of $83mW$, showing a five-fold reduction in lateral FWHM compared to the confocal image.

To test the resolution capability and determine how it varies with applied STED power, measurements are conducted using fluorescent crimson beads with a diameter of $48nm$ and an oil objective lens with $NA = 1.35$. Excitation of the crimson beads is achieved using light at a wavelength of $640nm$ and a power of $3.5\mu W$ at the back focal plane of the objective lens. The STED beam is phase modulated to create a donut shaped intensity profile at the focal plane of the objective lens, thereby enabling $2D$ resolution enhancement. xy STED images are recorded with a FOV of $5\mu m$ x $5\mu m$, a pixel size of $20nm$ x $20nm$, and a pixel dwell time of $40\mu s$ at different STED light powers. Field programmable

gate arrays are used in data acquisition cards to apply time-gating, which reduces confocal background noise. This process involves selectively detecting photons that arrive after a specified time interval relative to the excitation pulse, while disregarding those that arrive earlier [46, 47].

To determine resolution, a representative bead is chosen and the lateral FWHM of its image is calculated. The pixel with the maximum signal count in the bead image is identified as the center of the bead, and then a line profile through the center of the bead in the x direction is plotted. Three parallel, neighboring line profiles are averaged and then fitted with a Gaussian function to derive the FWHM.

Fig. 3.4(a) displays the derived FWHM at different STED powers. FWHM is averaged over five same representative beads for all the STED powers and the corresponding standard deviation is represented by the error bar. It shows a decrease in FWHM as STED power increases, as shown in Eq. 2.23, with convergence to $60nm$ after $\sim$ $120mW$ of STED power. Blue dashed line indicates the size of the crimson beads. Fig. 3.4(b) depicts the $2D$ image of crimson beads in the confocal microscope configuration. Finally, Fig. 3.4(c) displays the same image but with $83mW$ of STED power, demonstrating a 5-fold reduction in lateral FWHM.

3.2 Deformable mirror

This thesis presents an AO-based aberration correction method utilizing a DM (Multi-DM $3.5\mu m$ CDM, Boston Micromachines Corporation, US). The use of a DM is particularly advantageous in fluorescence imaging due to its polarization and wavelength independence. A schematic cross-section of a small portion of the DM is illustrated in Fig. 3.5(a). The DM is composed of an array of actuators arranged in a cartesian layout of electrodes mounted on a silicon substrate. These actuators are connected to a continuous flexible mirror face-sheet through attachment posts. By applying voltage to the electrodes, the actuators apply forces on the mirror sheet, causing it to deform. The DM consists of a square array of 140 actuators, with 12 of them situated across the aperture of the mirror. The pitch of these actuators is $400\mu m$, and they cover an area of $4.4mm$ x $4.4mm$. Fig. 3.5(b) displays the actuator map over the mirror surface. The yellow shaded region in-

dicates the aperture of the DM. The maximum stroke of the actuators is $3.5\mu m$, and the maximum voltage the DM can handle to achieve the maximum stroke is $210V$. The DM has a fast mechanical response time $< 75\mu s$, which is within the range of typical pixel dwell times in STED microscopy. This allows the DM to make rapid adjustments within just a few image pixels.

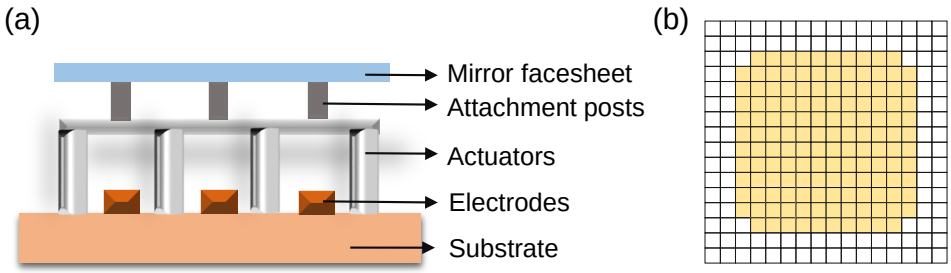

Figure 3.5: (a) Schematic cross-section of a small portion of the DM where actuators are attached to the continuous mirror face-sheet through attachment posts. The mirror is modulated by applying independent voltages to each of the actuators. (b) Actuators map over the DM surface. Each grid represents an actuator. The aperture of the DM is indicated by the yellow shaded region which consists total 140 actuators with a pitch of $400\mu m$, covering an area of $4.4mm$ x $4.4mm$.

3.2.1 Creating desired shape of the DM face-sheet

This section describes how to generate any desired shape on the DM face-sheet, using functions such as Zernike polynomials and aberration functions. An algorithm that controls the desired shape of the mirror face-sheet is available and implemented on the Matlab platform provided by Boston Micromachines. The Matlab control script for creating the desired shape of the mirror face-sheet is also available as a dynamic link library, which can be called by a Python script. This allows for easy integration of DM control into measurements performed in the Imspector software via the Python interface. The dynamic link library was created by Dr. Thomas Fricke Begemann.

The desired shape is defined within a circle, called the modulation region, which fits within the aperture of the mirror surface. The software parameters can be used to freely adjust the physical diameter and lateral position of the modulation region within the DM aperture. The area beyond the modulation region but within the DM aperture, indicated by the yellow shaded region in Fig. 3.5(b) must also be defined. There are two rows or columns of inactive actuators surrounding the DM aperture, as depicted in Fig. 3.5(b).

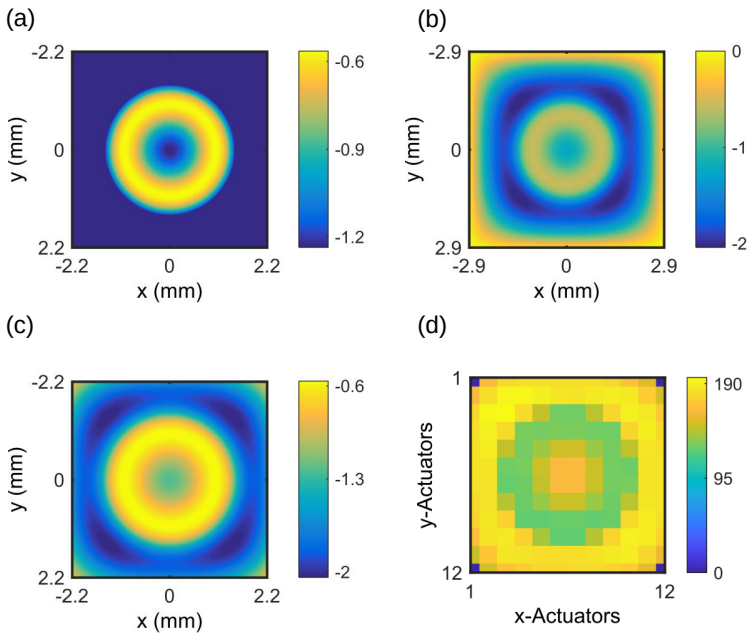

Figure 3.6: Creating the desired shape using the DM. (a) The desired shape is based on primary spherical aberration with an amplitude of $200nm$, calculated over a modulation region diameter of $3.4mm$. The x and y axes represent the range of the DM's 12 x 12 actuators. (b) Desired shape is then interpolated beyond the modulation region but within the DM aperture and finally driven to 0 beyond the edge of the DM aperture. x and y axes represent the total mirror face-sheet area. (c) The final desired shape (d) The voltages required to achieve the desired shape over the DM modulation region are determined based on the calibration data provided for the DM. The colorbar indicates the corresponding voltage values in volts. The x and y axes represent the area covered by the 12 x 12 actuators of the DM.

To mitigate any induced effects caused by these inactive actuators, the desired shape at the edge of the inactive actuators is driven to zero by interpolation. Furthermore, a constant offset of $900nm$ is added to the applied shape so that the voltage at each actuator corresponding to the desired shape is increased by a voltage corresponding to the $900nm$ actuation. This adjustment centers the mirror face-sheet in the axial center of the available actuator stroke. To generate the desired shape on the DM face-sheet, the corresponding voltage map is determined using the open loop calibration data specific to the DM provided by Boston Micromachines. This calibration data accounts for inter-actuator coupling and allows for the translation of the desired shape into the necessary voltages for each actuator.

Fig. 3.6 illustrates the creation of desired shape using the DM, for the example of primary spherical aberration $(j = 11)$ with an amplitude of $200nm$. In Fig. 3.6(a), the function, $W(\rho) = 200\sqrt{5}(6\rho^4 - 6\rho^2 + 1)$ is calculated over the modulation region with a diameter

of $3.4mm$. x and y axis represent the range of the 12 x 12 actuators as indicated by the yellow shaded region in Fig. 3.5(b). The colormap indicates the values of $W(x, y)$ in micrometers. Fig. 3.6(b) shows that the function is interpolated to zero beyond the edge of the yellow shaded region. Fig. 3.6(c) displays the final desired shape extracted within the yellow shaded region. Voltage values for each of the actuators are calculated using the given calibration data. Fig. 3.6(d) shows the voltage map to be applied to the DM for the desired shape of primary spherical aberration with amplitude of $200nm$.

3.2.2 Alignment of the DM

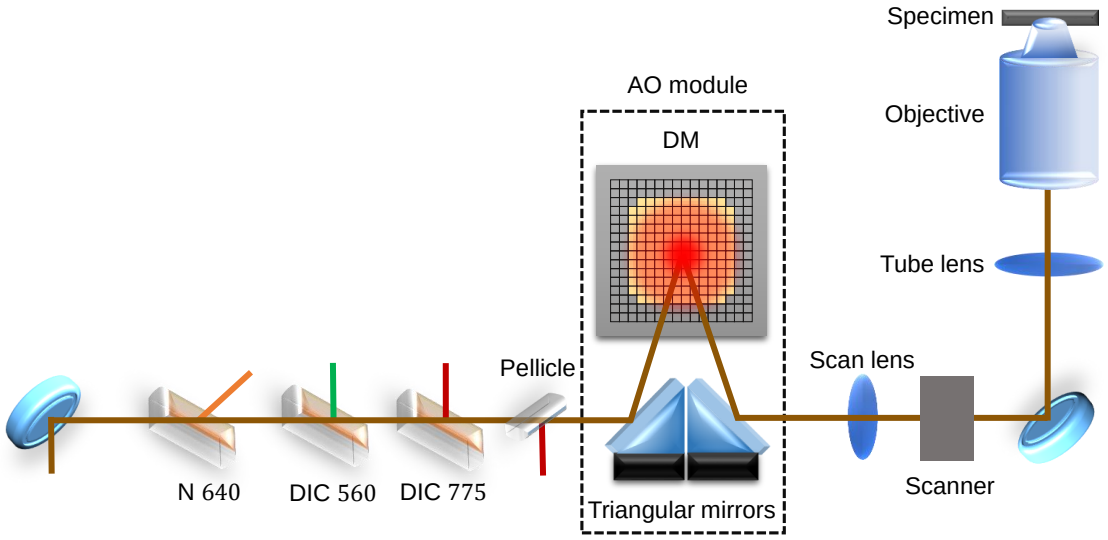

Figure 3.7: A segment of the setup labeled as AO module in Fig. 3.1 with the DM while the rest of the setup remains the same as previously described. The DM mirror face-sheet is placed conjugate to the back focal plane of the objective lens. A pair of triangular mirror is used. Excitation and STED beams after they are combined, reflected by one of the triangular mirror onto the DM. The reflected beams from the DM are directed towards the microscope by another triangular mirror. The fluorescence signal also travels back along the same path and is then directed towards the detection path.

The DM is placed in the common beam path of excitation, STED, and fluorescence light and its mirror face-sheet is positioned in a plane that is conjugate to the back focal plane of the objective lens. Fig. 3.7 displays a schematic of a portion of the experimental setup with the added DM while the rest of the setup remains the same as previously described in Fig. 3.1. To achieve a small angle of incidence of the light on the DM mirror face-sheet given the spatial constraints on the optical table, a pair of triangular mirrors are used to

direct the light towards the DM. The excitation and STED beams overlap and are reflected towards the DM by one of the triangular mirrors. The beams reflected by the DM are then directed towards the microscope by another triangular mirror. The fluorescence signal follows the same path back and also passes through the DM.

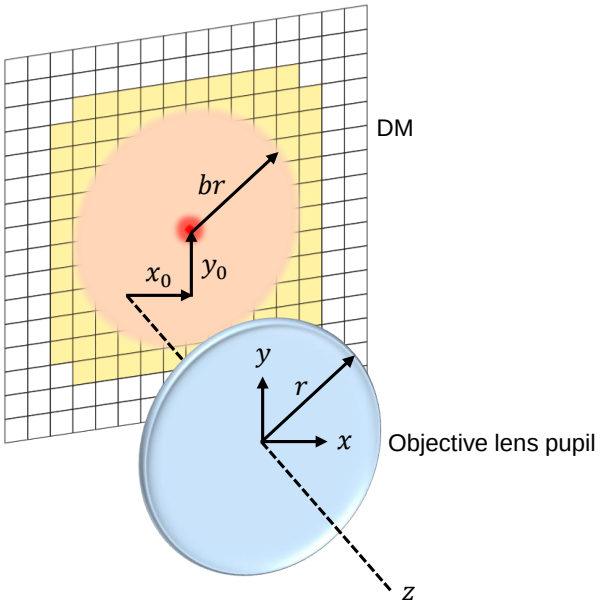

Figure 3.8: Indigo circle represents the back projected pupil of the objective lens, with the origin of the (x, y) coordinate system at its center. The pupil is de-magnified by the tube and scan lenses and has a radius of r. The red dot denotes the center of the DM modulation region over which Zernike functions are generated. Modulation region has a radius of $b\,r$, where b is a positive real number. The center of the DM modulation region has an offset (x_0, y_0) with respect to the center of the pupil.

Proper alignment of the modulation region on the mirror face-sheet with respect to the back projected pupil of the objective lens is crucial for effective aberration correction. Back projection in this context refers to the de-magnified pupil diameter that results from the combination of the tube lens and scan lens. Specifically, the centers of the modulation region and the objective lens pupil should lie on the same axis, and the diameter of both the modulation region and the back projected pupil should match. Misalignment of the modulation region, in terms of both diameter and position, can increase cross talk between aberration modes generated by the DM. In Fig. 3.8, the DM mirror face-sheet is shown along with its DM aperture (highlighted in yellow), as well as the modulation region (highlighted in orange) on the mirror face-sheet. The circular objective lens pupil is also shown (highlighted in indigo), which is back projected from the objective pupil plane to the DM face-sheet plane. It should be noted that both planes are drawn with an axial

offset along the z-axis for better visualization. The center of the pupil is represented by the Cartesian coordinates (x, y), where $\rho = \frac{\sqrt{x^2+y^2}}{r}$. Here, r is the radius of the objective pupil, and ρ is the normalized radial coordinate. Suppose, the center of the DM modulation region is offset by (x_0, y_0) in both the x and y directions with respect to the center of the pupil. When considering defocus $(j = 4)$, it is demonstrated in Eq. 3.1 that these offsets induce horizontal tilt $(j = 2)$ and vertical tilt $(j = 3)$ with amplitudes proportional to the offsets. Eq. 3.1 begins with the Zernike polynomial of defocus, where the normalization constant is ignored. The polynomial is then expressed in Cartesian coordinates. An offset of x_0 and y_0 is applied to both the x and y directions. The resulting equation expressed in polar coordinate, shows not only the defocus term but also the horizontal tilt (second term), vertical tilt (third term), and piston (fourth term).

$$
\begin{aligned}
Z_4^0 &= 2\rho^2 - 1 = \frac{2}{r^2}(x + x_0)^2 + \frac{2}{r^2}(y + y_0)^2 - 1 \\
Z_4^0\big|_{x\to x+x_0,\, y\to y+y_0} &= \frac{2}{r^2}(x^2 + y^2) - 1 + \frac{4}{r^2} x\, x_0 + \\
&\qquad \frac{4}{r^2} y\, y_0 + \frac{2}{r^2}({x_0}^2 + {y_0}^2) \\
Z_4^0\big|_{\textit{with offset}} &= (2\rho^2 - 1) + \frac{2x_0}{r}\, 2\rho \cos\phi + \frac{2y_0}{r}\, 2\rho \sin\phi + \frac{2}{r^2}({x_0}^2 + {y_0}^2)
\end{aligned}
\tag{3.1}
$$

The strategy for aligning the position of the DM modulation region exploits the induction of tilt by defocus when the modulation region is offset with respect to the objective lens pupil. The expectation is that when there is no offset present, defocus will not introduce any lateral shift to the PSFs. This can be measured observing the shift in the PSFs.

To align the DM modulation region with respect to the objective pupil, measurements are carried out using gold beads with a diameter of $80nm$ and an oil objective lens with a $NA = 1.35$. Excitation light with a wavelength of $640nm$ is used, and the reflected light from single gold beads is detected by the PMT. As mentioned in section 3.2.1 the modulation region on the mirror face-sheet which serves as the unit circle on which the Zernike polynomials are calculated can be offset both in x and y directions using the software interface associated with the DM. Offsets in the x direction is varied using the software and for each offset, the DM applies defocus with different amplitudes. Here $(x_0, y_0 = 0, 0)$ represents the physical center of the DM aperture. For each combination

of x-offset and defocus amplitude, xz images of single gold beads are recorded at the y-center of each bead.

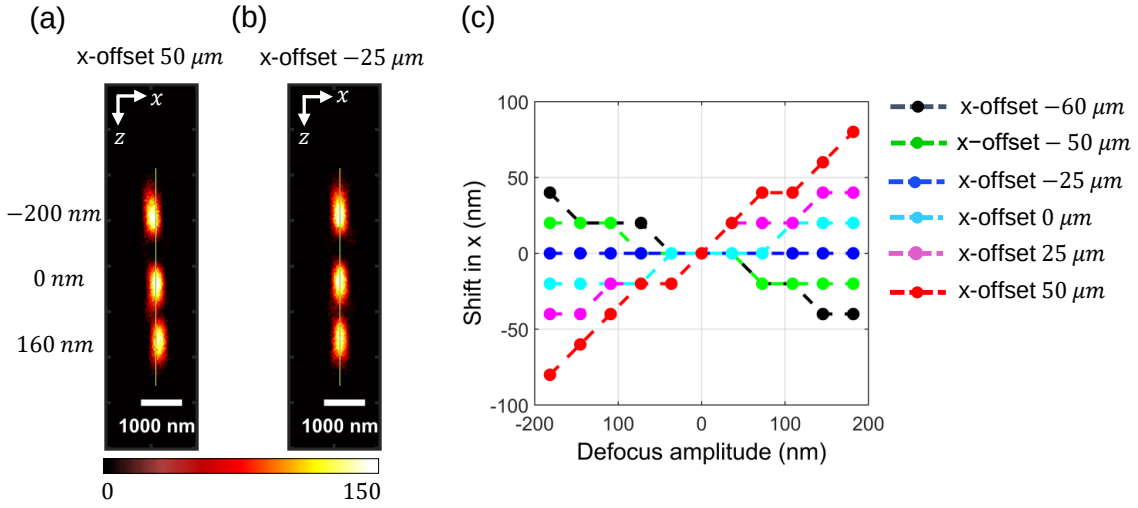

Figure 3.9: To align the DM modulation region with respect to the objective lens pupil, measurements are performed using gold beads, an excitation beam at a wavelength of $640nm$ and an oil objective lens with *NA* of 1.35. xz PSFs are measured for different amount of x-offsets while varying the defocus amplitudes. xz PSFs are obtained at the y-center of each beads with defocus amplitudes of $-200nm$, $0nm$, and $160nm$ when the x-offset is set as (a) $50\mu m$ (b) and $-25\mu m$ (c) Lateral shifts of the PSFs at different defocus amplitudes with respect to the PSF with $0nm$ defocus in the x direction are calculated for various x-offset. The results indicate that the induced lateral shift by the defocus is minimum for $-25\mu m$ x-offset.

Fig. 3.9(a) and 3.9(b) illustrate an overlay of xz PSFs for defocus amplitudes of $-200nm$, $0nm$, and $160nm$, with different x-offsets of $50\mu m$ (a) and $-25\mu m$ (b). The green line represents the line through the lateral center of the PSF with $0nm$ defocus. It is clear from the figures that PSFs with varying defocus amplitudes exhibit a lateral shift relative to the PSF with $0nm$ defocus when the offset is $50\mu m$. In contrast, the lateral shift is minimal for an x-offset of $-25\mu m$. Fig. 3.9(c) depicts the amount of lateral shift of the PSFs with different defocus amplitudes for various x-offsets. The amount of lateral shift of a PSF obtained at certain defocus amplitude is determined relative to the PSF obtained with zero defocus as follows: the Fourier transform is taken of each PSF image using a fast Fourier transform algorithm. The complex conjugate of one of the Fourier transforms is then computed. These two Fourier transforms are multiplied element-wise, and the resulting product is inverse Fourier transformed using an inverse FFT algorithm. The peak value in the resulting image corresponds to the cross-correlation coefficient, while

the position of the peak corresponds to the shift. The results indicate that an x offset of $-25\mu m$ is optimal because defocus induces the least lateral shift. To determine the y-offset, the same measurements are performed, but images are recorded in the yz plane. The results of these measurements yields a y-offset of $30\mu m$. To align the diameter of the DM modulation region, a similar approach is taken. Let us consider that the radius of the DM modulation region is different from the radius of the back-projected objective pupil, and is given by $b\,r$, where b is a positive real number as displayed in Fig. 3.8. When horizontal primary coma $(j = 8)$ is taken into consideration, it is shown in Eq. 3.2 that different radius of the DM modulation region with respect to the back-projected objective pupil induces horizontal tilt $(j = 2)$.

$$\begin{aligned} Z_3^1|_{r\to b\,r} &= 3\,\frac{\rho^2}{b^2} - 2\,\frac{\rho}{b}\cos\phi \\ &= \frac{1}{b^2}\,(3\rho^2 - 2\rho)\,\cos\phi + 2\rho\,\cos\phi\,(\frac{1}{b^2} - \frac{1}{b}) \end{aligned} \tag{3.2}$$

This fact is exploited to determine the appropriate radius of the DM modulation region. The expectation is that when the correct radius is used, coma will not introduce any lateral shift to the PSFs due to the horizontal tilt.

To perform the measurements, gold beads with a diameter of $80nm$ are utilized. The beads are illuminated with excitation light at a wavelength of $640nm$, and are imaged using an oil objective lens with a *NA* $= 1.35$. The reflected light from single beads is detected using the PMT. Different diameters of the modulation region are set by the DM software. Primary horizontal coma with various amplitudes is then applied by the DM for each diameter. xz images of gold beads are recorded at the y-center of each bead, and line profiles through the lateral center of the bead images are plotted. Fig. 3.10(a)-(c) illustrate the line profiles of the PSFs with coma amplitudes of $-30nm$, $0nm$, and $30nm$ at various diameters. In Fig. 3.10(b) and (c), it can be observed that the PSFs with $-30nm$ and $30nm$ coma amplitudes exhibit a lateral shift in comparison to the PSF with a $0nm$ coma amplitude. Conversely, Fig. 3.10(a) demonstrates the maximum overlap of the PSFs, indicating that a modulation region diameter of $3.4mm$ is optimal.

It is important to note that the optimal x and y offset and diameter of the DM modulation region depend on the choice of the objective lens used. To illustrate this point, the same measurements are conducted with a water objective lens of *NA* $= 1.20$, which yields an

optimal x offset of $-40\mu m$, a y offset of $40\mu m$, and a modulation region diameter of $3.2mm$.

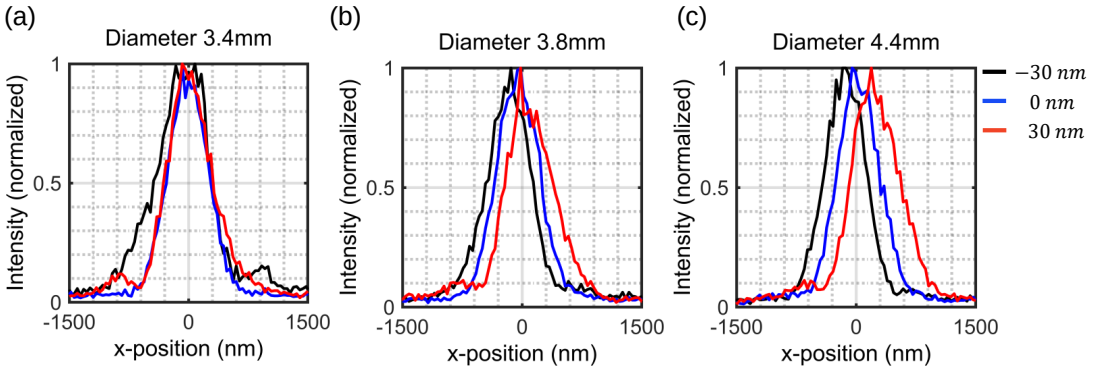

Figure 3.10: To match the diameter of the DM modulation region to the back-projected objective lens pupil, measurements are performed using gold beads, an excitation beam at a wavelength of $640nm$ and an oil objective lens with *NA* of 1.35. xz PSFs at the y-center of each bead are measured for different amount of modulation region diameter while varying the horizontal coma. Line profiles are plotted through the lateral center of the PSFs. Line profiles are obtained with coma amplitudes of $-30nm$, $0nm$, and $30nm$ when the DM modulation region diameter is set as (a) $3.4mm$ (b) $3.8mm$ and (c) $4.4mm$. The results indicate that the lateral shift due to tilt induced by the coma is minimum for $3.4mm$ diameter.

3.2.3 Characterization of the DM

To accurately introduce or correct Zernike based wavefront aberrations using a DM, it is important to determine the shape and amplitude of the wavefront deformation generated in response to a given aberration amplitude applied to the DM. A reliable way to calibrate a DM is to use a wavefront sensor. In this thesis, the wavefront sensor is solely used for this purpose and is not involved in generating the experimental results for aberration correction. Due to spatial constraints in the experimental setup, the DM characterization is performed in a separate test setup with a water objective lens and with a DM, both of the same design as the ones used for the measurements presented in chapter 4.

The wavefront sensor (WFS$40-14$AR, Thorlabs, Germany) utilized in this thesis is a Shack-Hartmann wavefront sensor, which determines the shape of an incoming beam's wavefront by breaking it into an array of discrete intensity points. It achieves this by using a square microlens array with a pitch of $300\mu m$ and an effective focal length of $14.6mm$. At a distance of one focal length from the microlens array, a CMOS camera sensor is mounted, with a maximum active area of $11.26mm$ x $11.26mm$ and a resolution of up to 2048 x 2048 pixels. The wavefront sensor operates by tracking the position of the focal

spots on the camera sensor. If the incoming wavefront is flat, all the focal spots are arranged in a regular grid defined by the lenslet array geometry. However, when aberrations are present in the wavefront, the focal spots move from their initial positions. The shape of the wavefront $W(x, y)$ can be determined by analyzing the spot shift. The wavefront is then reconstructed by fitting it with Zernike polynomials weighted by their amplitudes. Typically, a least squares Zernike fit is performed to determine the Zernike amplitudes.

The wavefront sensor is positioned at the location of the objective lens such that its reference plane, that is the plane in which the wavefront sensor analyzes the wavefront, coincides with the back focal plane of the objective lens. This arrangement ensures that the DM mirror face-sheet and the wavefront reference plane are conjugate to each other. Following the protocol outlined in section 3.2.2, the diameter of the modulation region of the DM is matched to the objective lens pupil. Due to the slightly different optical system in the test setup as compared to the STED microscopy setup, the diameter of the DM modulation region is $3.6mm$ for the water objective lens as opposed to $3.2mm$ derived for the same lens in the STED microscopy setup. Its diameter thus matches the largest modulation diameter used in the STED microscopy setup.

In the wavefront sensor software, the Zernike evaluation circle represents the unit circle and serves as a boundary for determining which spots are used to fit the wavefront to Zernike functions. Specifically, only the spots located within this circle are used for fitting. The center and the diameter of this Zernike evaluation circle must be aligned with the DM modulation region. To determine the center coordinates in both x and y directions, a strategy is followed that involves applying a defocus of preferably higher amplitude to the DM. The pupil's center in x and y direction in the wavefront sensor software is fine tuned until no horizontal and vertical wavefront tilt is induced by the DM. The diameter of the Zernike evaluation circle is set such that no defocus aberration is detected when a primary spherical aberration $(j = 11)$ with an amplitude of $\sim 200nm$ is applied to the DM. This relatively large amplitude is necessary to more clearly pronounce the effect and accurately determine the optimal pupil diameter of the wavefront sensor. As expected, the experimentally determined diameter of the evaluation circle agrees closely with the theoretical pupil diameter of $7.2mm$, which is calculated as $2NAf$ with $f = 3mm$ being the focal length of the objective lens.

The primary goal of this thesis is to correct specimen induced aberrations, which are predominantly spherical aberrations in the case of refractive index mismatched specimens. Therefore, the wavefront sensor is primarily used to assess the DM response for spherical aberrations. The DM is subjected to primary $(j = 11)$, secondary $(j = 12)$, and tertiary $(j = 37)$ spherical aberrations, and the corresponding wavefronts generated by the DM are measured by the wavefront sensor. The amplitudes of the applied spherical aberrations are selected as $30nm$, $20nm$, and $25nm$ for primary, secondary, and tertiary spherical aberration, respectively, to ensure that the resulting PV of the DM mirror face-sheet is approximately $100nm$ resulting in an expected PV of the measured wavefront of approximately $200nm$. This PV value is chosen because it falls comfortably below the maximum stroke capacity of the mirror, while still being sufficiently higher than the minimum detectable deformation of the mirror face-sheet.

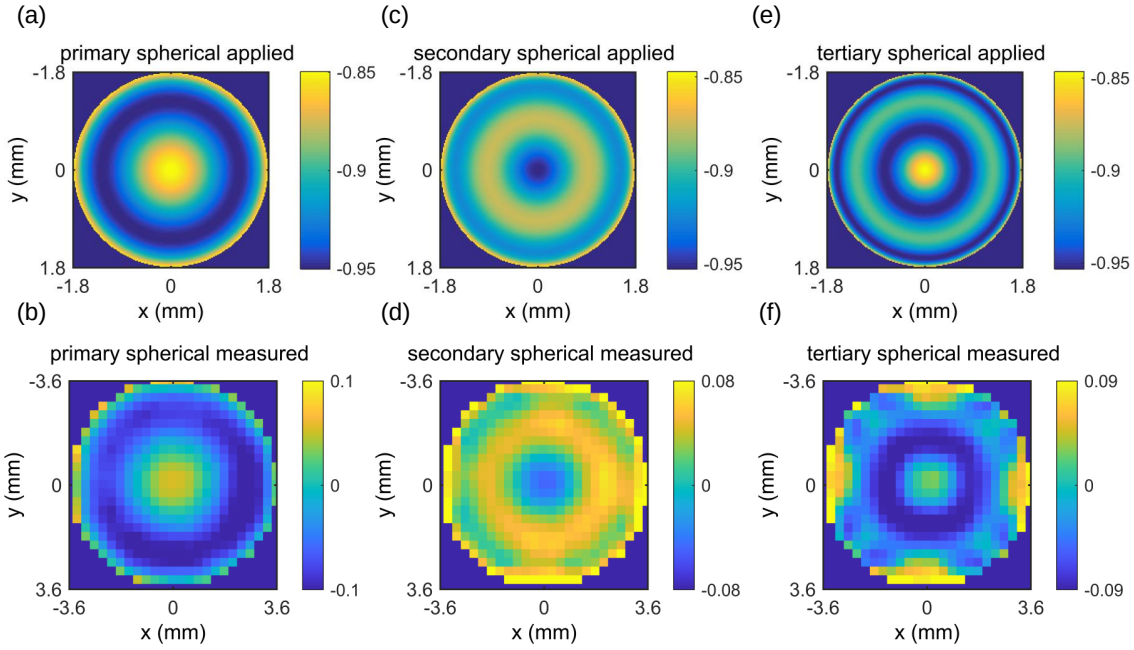

Figure 3.11: The desired shape applied to the DM is generated using a modulation region of $3.6mm$ (top row), while the measured wavefronts are obtained using the WFS with an evaluation circle of $7.2mm$ in diameter (bottom row). (a) and (b) primary spherical. (c) and (d) secondary spherical. (e) and (f) tertiary spherical. The colorbars indicate the mirror face-sheet deformation (a,c,e) and the measured wavefront (b,d,f) in μm.

The DM modulation is generated using the approach described in section 3.2.1. Fig. 3.11(a) displays the desired shape of the DM face-sheet for a primary spherical aberration with $30nm$ amplitude applied to the DM, and Fig. 3.11(b) shows the measured wavefront. Similarly, Fig. 3.11(c) shows the desired shape for a secondary spherical aberration

with $20nm$ amplitude applied to the DM, and Fig. 3.11(d) displays the measured wavefront. The obtained results indicate that the DM effectively achieves the desired primary spherical aberration of the wavefront, and, albeit with a lower quality and smaller PV than expected, also the secondary spherical aberration. However, tertiary spherical aberration, which is a polynomial with radial order 8 cannot be generated. Fig. 3.11(e) displays the applied tertiary spherical aberration with an amplitude of $25nm$, while Fig. 3.11(f) shows the measured wavefront that clearly does not exhibit a radial symmetry anymore and lacks the ring-shaped outer minimum. This can be explained as follows, only a maximum of 10 actuators along the diameter of the DM aperture are within the DM modulation region, and the number of actuators along the diagonal is at most 7. This limited number of actuators is not sufficient to generate an eighth-order polynomial.

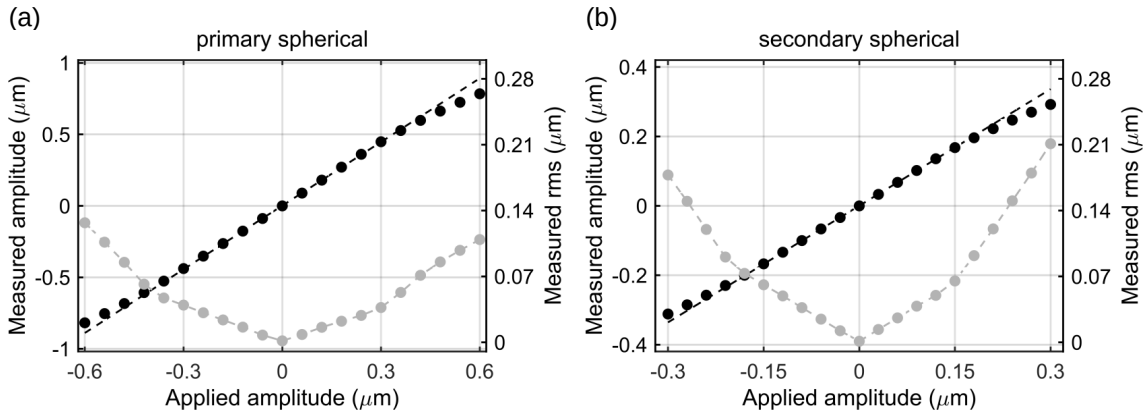

Figure 3.12: The DM is subjected to various amplitudes of primary spherical (a) and secondary spherical (b) aberration modes, and the resulting change in the wavefront is measured using the WFS. The reconstructed wavefront is then analyzed. In the figure, the obtained amplitudes of the respective aberration mode at each applied amplitude to the DM are represented by black circular data points. The black dashed line indicates linearity. Additionally, the rms values of the residual wavefront, reconstructed from the presence of other aberration modes (excluding tip, tilt, and defocus), are depicted as grey data points.

To evaluate the capability of the DM to induce different amplitudes of primary spherical and secondary spherical aberration, the DM is subjected to primary spherical aberration ranging from $-600nm$ to $600nm$, and secondary spherical aberration ranging from $-300nm$ to $300nm$. The resulting wavefront is measured for each amplitude using the WFS fitted and reconstructed with Zernike polynomials up to order 8. Fig. 3.12(a) illustrates the measured amplitude of the primary spherical aberration at various amplitudes applied to the DM, shown by the black circular data points. The black dashed line represents a linear fit

to the central data points, implying that if all the measured values adhere to a linear relationship with the applied aberration amplitudes, they should closely align with the dashed line. The analysis of the wavefront using Zernike polynomials indicates that the desired primary spherical aberration is not generated in its pure form. Instead, it is accompanied by additional undesirable Zernike modes of smaller amplitude. The analysis excludes tip, tilt, and defocus, as they only cause a constant lateral or axial shift. To quantify these contributions, the residual wavefront, which comprises these modes, is reconstructed, and its rms value is calculated. In Fig. 3.12(a), these rms values are represented by grey data points. Similarly, in Fig. 3.12(b), the corresponding results for applying secondary spherical aberration to the DM are presented.

It is observed that the amplitudes of the wavefront aberration and the applied amplitudes to the DM exhibit a linear relationship only within a limited range of $\pm 300nm$ for primary spherical and $\pm 160nm$ for secondary spherical aberration. Therefore, it will be necessary to recalibrate the DM if the desired wavefront shape falls outside of this range. As a result, the effective range of the DM that can be used without recalibration is limited. Additionally, there is a higher contribution of other aberration modes, particularly for secondary spherical aberration, which is likely due to the limited number of actuators being utilized. As the relative contribution of these undesired modes increases beyond the linear range, the subsequent usage of the DM will generally be confined to lie within this range.

3.3 Application of aberration correction

The initial step in aberration correction is to assess the quality of correction that can be achieved at a specific depth within the specimen through a refractive index mismatch. Two critical factors that influence wavefront deformation are the choice of the *NA* and the immersion medium of the objective lens. Additionally, the type and magnitude of wavefront deformation that can be corrected depend on the number of usable actuators and the maximum usable stroke of the DM. These limitations of the DM have been discussed in the previous section. To find the achievable quality of aberration correction under these constraints, measurements are performed on $150nm$-sized, sparsely distributed gold beads with a water objective lens with $NA = 1.20$. The measurements are carried out in the same

test setup mentioned in the previous section 3.2.3, which is a confocal microscope featuring a piezo based sample scanning for image acquisition. Gold beads are illuminated with an excitation wavelength of $640nm$ and reflected light from the beads is detected by a PMT.

The sample is prepared as a two-layered structure using the following protocol: Gold beads are mounted on two coverslips as illustrated in Fig. 3.13. The coverslips are positioned facing each other, with the bead layers oriented inwards. They are separated by a certain amount of embedding medium composed of a mixture of water and $2,2$-Thiodiethanol which creates a specific distance between the layers. The immersion and embedding medium have refractive indices of $n_1 = 1.333$ and $n_2 = 1.401$, respectively. Upon observation through the microscope, it is found that the distance between the two layers is $95\mu m$.

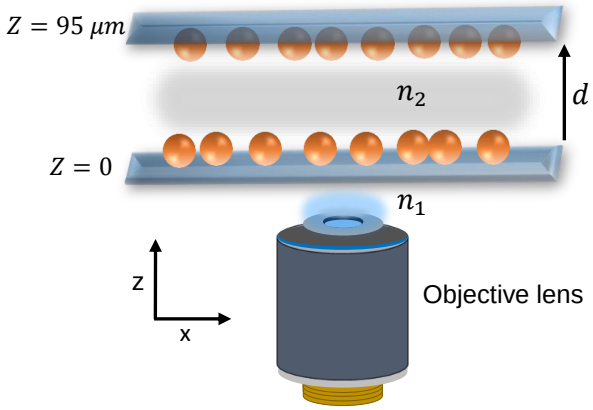

Figure 3.13: Schematic representation of two-layered bead sample. The beads are mounted on two coverslips separated by a layer of liquid, creating a specific distance, d between the two layers. n_1 and n_2 are the refractive indices of immersion medium and embedding medium, respectively.

The objective lens is focused on the layer at $z = 95\mu m$. Light waves, as they pass through the interface between two mediums with different refractive indices become distorted and introduce spherical aberrations. Two approaches can be used to compensate for this distortion by modulating the DM. One approach is to apply different amplitudes of primary and secondary spherical aberration functions to the DM. The other approach is to apply the entire aberration function, as expressed in Eq. 2.38, to the DM.

Aberration correction by applying individual Zernike functions

To determine the necessary range of applied amplitudes for correcting aberrations at the specific depth and with the particular refractive index mismatch, a simulation is conducted using vector diffraction theory [37]. This simulation helps to estimate the amplitudes required for achieving the correction. The amplitudes of primary spherical aberration applied to the DM are varied within a certain range, including amplitudes of $100nm$, $180nm$, $200nm$, $220nm$, $240nm$, $260nm$, and $300nm$. For each value of primary spherical aberration, the amplitude of secondary spherical is also adjusted. The maximum range for the secondary spherical aberration amplitude is set between $20nm$ to $160nm$ though the actual range of the secondary spherical aberration amplitude varies depending on the applied primary spherical aberration amplitude. During each iteration, which represents a combination of a primary and secondary aberrations amplitude, xz-sections are recorded through the y-center of individual gold beads. The maximum signal count and the axial FWHM of the gold bead image are then calculated. The maximum signal count and axial FWHM serve as measures of the quality of correction. Since the size of the gold bead is relatively small compared to the axial extent of the excitation PSF, the image of a single gold bead adequately approximates the PSF in this particular context. Hence, it is commonly referred to as the PSF in the subsequent analysis. Additionally, PSFs are also measured at $z = 0$, providing the reference PSF without aberration. Fig. 3.14(a) and (b) show plots of the maximum signal count and axial FWHM of the PSFs as a function of iteration, respectively. The maximum signal count is normalized with respect to that of the PSFs at $z = 0$. Each data point represents the maximum signal count or FWHM of the PSFs for a specific combination of primary and secondary spherical aberration amplitudes. Iteration 0 corresponds to the case when both the amplitudes are zero, meaning no aberration correction is performed. Each data point represents an average value obtained from three representative beads, and the error bar indicates the corresponding standard deviation. The blue dashed line marks the maximum signal count or axial FWHM of the PSF measured at $z = 0$. The red lines represent the increasing amplitudes of primary spherical aberration from left to right, with no secondary spherical aberration applied. Data points between two adjacent red lines correspond to measurements taken with both primary and secondary spherical aberrations applied. It is evident from the graphs that the maximum

signal count and FWHM change at different combination of amplitudes. For the combination of primary spherical amplitude of $200nm$ and secondary spherical of $60nm$ (iteration 14), the PSF quality is best and 65% of brightness can be restored.

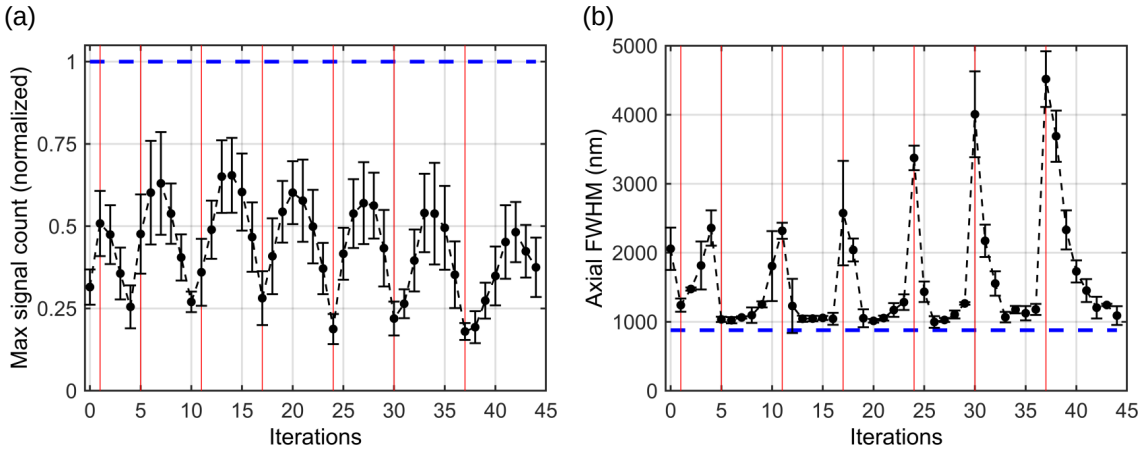

Figure 3.14: Evaluation of aberration correction quality at $z = 95\mu m$ using a two-layered gold bead sample with a refractive index mismatch of $\Delta n = 0.068$. The measurements are performed using a water immersion objective lens with $NA = 1.20$ and excitation light at wavelength of $640nm$. PSFs in xz plane are measured for different combination of primary and secondary spherical aberration amplitudes applied to the DM. Each combination is referred to as an iteration. (a) Normalized maximum signal count as a function of the iteration. The blue dashed line indicates the maximum signal count at $z = 0$. The combination of $200nm$ primary spherical aberration and $60nm$ secondary spherical aberration (iteration 14) achieves maximum signal count, restoring 65% of brightness. (b) Similar graph but with the axial FWHM of PSFs measured at $z = 95\mu m$ plotted on the y-axis. The blue dashed line indicates the axial FWHM at $z = 0$.

It is relevant to note that the chosen depth of $95\mu m$ is deliberately selected for the purpose of assessing the quality of aberration correction achieved in the context of large spherical aberration amplitudes. These amplitudes are close to the edge of the linear response regime, as depicted in Fig. 3.12. The main objective of utilizing such a large depth is to evaluate the effectiveness of the correction at the edge of the linear response regime, where the system is most challenged.

Aberration correction by applying the entire aberration function

Instead of modulating the DM with individual Zernike functions, it is also possible to modulate the DM by applying the entire aberration function as presented in Eq. 2.38, to correct the wavefront deformation. To compare the quality of aberration correction achieved in these two scenarios, measurements are performed with the same sample and experimen-

tal parameters. However, in this case, the DM is modulated with the aberration function varying nominal focal position, d'. It is found that modulating the DM with the full aberration function required a too large modulation amplitude of the DM face-sheet. Therefore, At each d', the corresponding defocus amplitude is calculated following [37]. This defocus amplitude is then subtracted from the aberration function, resulting in a modified aberration function. Subsequently, this modified aberration function is applied to the DM.

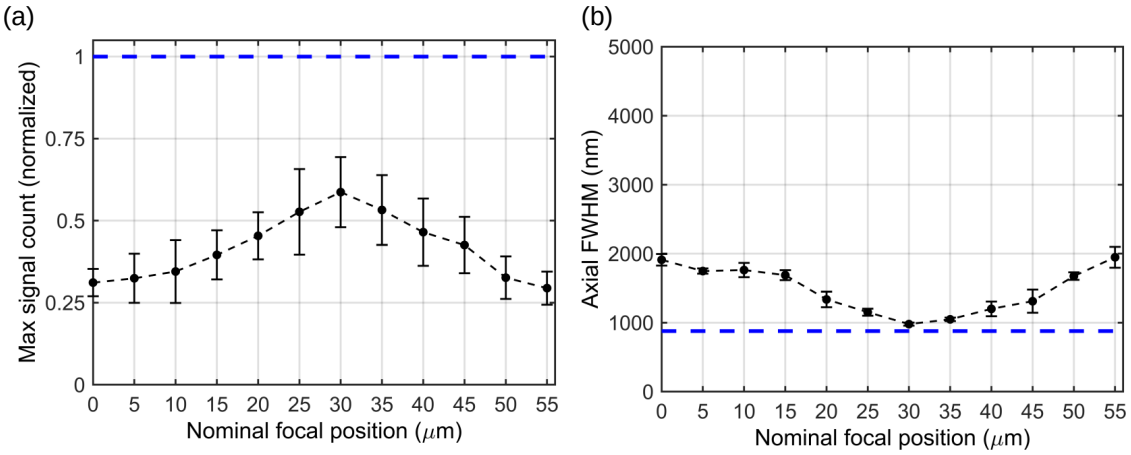

Figure 3.15: Aberration correction is achieved by applying the entire aberration function to the DM, while varying the nominal focal position, d'. The sample and experimental parameters remain the same as in Fig. 3.14. (a) Normalized maximum signal count as a function of d' showing a maximum at $d' = 30\mu m$. (b) Axial FWHM as a function of d' showing minimum at $d' = 30\mu m$. It is important to note that the d' is not the same as the depth observed through a microscope. Blue dashed line indicates maximum signal counts and axial FWHM at $d' = 0$

It is expected that aberration correction is maximum at a certain d'. However, it is important to note that this nominal focal position, d', is not the same as the actual focal position that is observed through the microscope. The actual focal position is affected by the refractive index mismatch, whereas the nominal focal position is a reference point used to define the aberration function. Fig. 3.15 shows the normalized maximum signal count and the axial FWHM as a function of d'. The blue dashed line indicates the maximum signal count or FWHM at $d' = 0$ which corresponds to no aberration correction. The PSFs measured at $z = 0$, without aberration correction at $z = 95\mu m$ and with aberration correction are presented in Fig. 3.16(a), (b), (c) respectively for both the correction procedures.

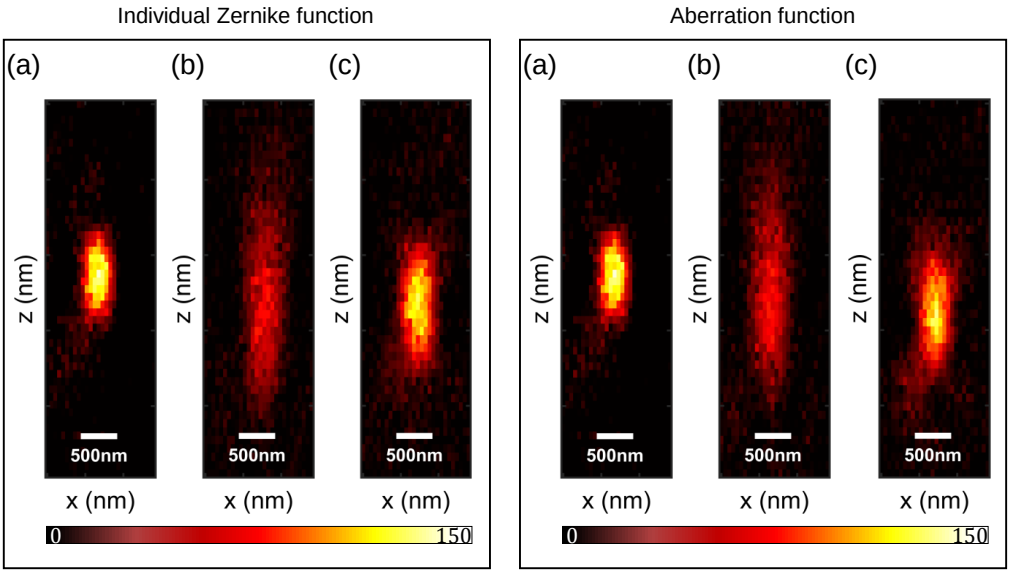

Figure 3.16: Visualization of the PSF in a two-layered gold bead sample at $z = 0\mu m$ and $z = 95\mu m$ through a refractive index mismatch of $\Delta n = 0.068$. The sample is illuminated with a $640nm$ light and imaged using a water objective lens with *NA* $= 1.20$. (a) xz PSF measured at $z = 0\mu m$. (b) xz PSF measured at $z = 95\mu m$ without aberration correction. (c) xz PSF measured at $z = 95\mu m$ with aberration correction achieved by applying a primary spherical aberration amplitude of $200nm$ and a secondary spherical aberration amplitude of $60nm$ (left) and applying the modified aberration function (right).

In a deep tissue region where both the refractive index and depth are unknown, there is no significant advantage in using the modified aberration function for aberration correction compared to applying individual Zernike functions. Furthermore, the correction scheme involving individual spherical aberrations yields slightly better results in terms of correction quality. As a result, for subsequent measurements, individual Zernike functions will be applied to the DM for aberration correction.

Chapter 4

Photon stream-based metric and fluorescence measurement

This chapter introduces the photon stream-based metric for aberration correction and presents the results obtained using this approach. The microscope setup described in chapter 2 is used to generate these results. The experimental measurements are performed while taking into consideration the knowledge gained from the characterization of the setup and the DM. All STED imaging experiments are performed using a STED beam with a donut-shaped intensity profile at the focal plane, which allows for $2D$ resolution enhancement in the xy plane.

4.1 Photon stream-based metric

The importance of finding new metrics that can accurately assess image aberrations based on the photo-physical properties of the fluorophores, rather than relying solely on image brightness, sharpness, or contrast, has already been discussed in chapters 1 and 2.

4.1.1 Principle of photon stream-based metric

Fluorescence lifetime, τ_{fl}, is one of the photo-physical properties of fluorophores that is described in section 2.1. At ambient temperature, the fluorescence lifetime is typically a few nanoseconds. However, it is important to note that the presence of other probe light can influence the lifetime. For instance, in STED microscopy, lifetime is reduced due to the presence of STED light-induced stimulated emission and as the intensity of the STED light increases, lifetime further decreases.

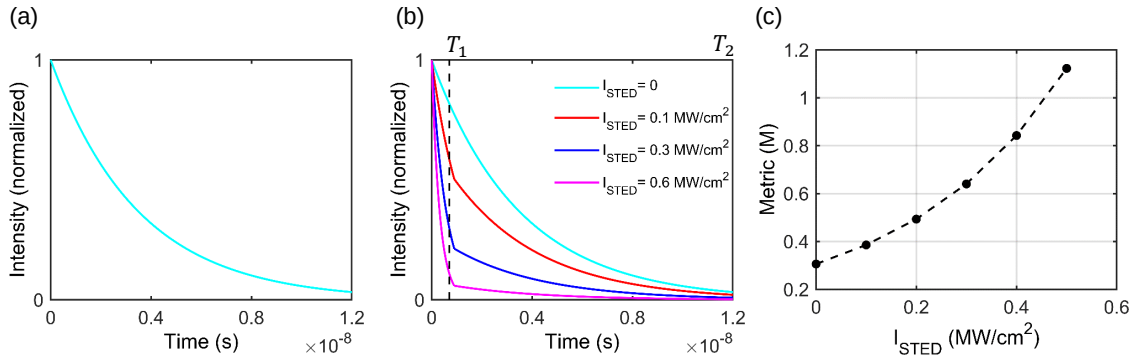

Figure 4.1: Principle of photon stream-based metric for evaluating aberration. (a) Normalized fluorescence intensity is plotted as a function of time for a fluorescence lifetime of $3.5ns$. (b) In the presence of STED light, normalized fluorescence intensity is plotted as a function of time for different values of average STED pulse intensity,I_{STED}. The lifetime of fluorescence is reduced as I_{STED} increases. The photon stream is divided into two parts based on the time T_1, with all photons acquired before T_1 called early photons and those acquired after T_1 called late photons. The photon stream-based metric is defined as the ratio of early photons to late photons. (c) The metric is calculated for various STED intensities and shows an increase with an increase of STED intensity.

In Fig. 4.1(a), the normalized fluorescence intensity is plotted as a function of time for a τ_{fl} of $3.5ns$, following Eq. 2.2. The choice of τ_{fl} is based on the lifetime of a standard STED fluorophore, abberior Star580 (Abberior STAR 580, Abberior, Germany), which is subsequently utilized in the experiment. Fig. 4.1(b) shows the normalized fluorescence intensity, calculated using Eq. 2.13, where $k_{STED} = \sigma_{STED} \frac{I_{STED}}{\tau_{STED}\, h\nu_{STED}\, R}$. Here, I_{STED} represents the average pulse intensity of the STED beam, and the definitions of the other parameters can be found in Section 2.4.1. When time (t) is less than the pulse width of the STED light (τ_{STED}), the fluorescence intensity follows the aforementioned equation. However, for $t \geq \tau_{STED}$, the STED dependent fluorescence intensity is replaced by $e^{-k_{STED}\tau_{STED}}$. This indicates the remaining fluorescence intensity after a single STED

pulse duration. The plot depicts different fluorescence intensity curves corresponding to different values of I_{STED}. The parameters are set for a typical fluorophore under STED illumination with a repetition rate of $40MHz$, pulse length of $900ps$, a wavelength of $775nm$ and a stimulated emission cross section of $4.6 \times 10^{-}21m^2$ [23]. It can be observed that as the intensity of the STED light increases, lifetime becomes progressively smaller.

The natural fluorescence lifetime of a fluorophore is independent of the excitation light intensity, whereas the effective fluorescence lifetime depends on the intensity of the probe laser. By switching the probe laser on and off during measurement, both the natural and effective lifetimes can be acquired. When only the excitation laser is on, a single lifetime of τ_{fl} is present. However, as soon as the STED laser is added, the lifetime behavior changes. The distribution of photon arrival time exhibits a rapid decay during the initial phase when the STED laser is active, which is subsequently followed by the natural decay of the fluorophore. It is worth noting that this phenomenon is expected given the assumption that the STED pulse duration is shorter than the natural fluorescence lifetime.

The photons obtained when both the excitation and STED laser are active are referred to as 'early photons', while those obtained when only the excitation laser is active are referred to as 'late photons'. In Fig. 4.1(b), a black dashed line indicates the time T_1, which separates early and late photons. Early photons are defined as those detected before time T_1, while late photons are those detected after T_1. Therefore the metric can be quantitatively expressed as,

$$M = \frac{\int_0^{T_1} I_0\, e^{-\frac{t}{\tau_{fl}}}\, e^{-t\,\frac{\sigma_{STED}\, j}{\tau_{STED}}}\, dt}{\int_{T_1}^{T_2} I_0\, e^{-\frac{t}{\tau_{fl}}}\, e^{-T_1\,\frac{\sigma_{STED}\, j}{\tau_{STED}}}\, dt} \tag{4.1}$$

where, all the parameters are defined in section 2.4.1. j can be expressed as $j = \frac{I_{STED}}{h\,\nu_{STED}\,R}$. Duration of the late photon range, represented by T_2, extends up to the fluorescence lifetime. T_1 can be chosen conveniently as comparable to the pulse width of the STED laser because it allows to separate the photons influenced by STED from those that are not. In Fig. 4.1(c), M is calculated for various I_{STED} values, and it is observed that an increase in I_{STED} results in a corresponding increase in M.

Aberration causes the intensity of the probe laser in the focal region to decrease, leading to a decrease in M. Therefore, The ratio between the number of early and late photons

can be used as a metric to evaluate the aberrations present in the system [5].

4.1.2 Measurement protocol for metric determination

In a typical STED measurement protocol, in the easiest implementation, the number of detected fluorescence photons is integrated over the pixel dwell time, and the resulting total photon count is assigned to the corresponding image pixel. However, this process discards all information about the arrival time of the photons in relation to the excitation pulse. In a more elaborate approach, typically used for suppressing signals contributing to a confocal background, a technique known as time-gating [46, 47] is applied. This technique is implemented using the timing capabilities of the field programmable gate array-based data acquisition card. With time-gating, only fluorescence photons arriving after a certain time relative to the respective excitation pulse are considered for image generation. The rest of the photons are disregarded. To extract the photon stream-based metric from STED measurements, it is not necessary to know the full photon arrival time histogram. Instead, it is sufficient to determine, for each image pixel, the number of detected photons with photon arrival times smaller than T_1 and larger than T_1 as depicted in Fig. 4.1(b). To accomplish this, the STED measurement protocol is adapted to generate two images instead of one for each measurement. The pixel values of the first image represent the count number of photons with arrival times smaller than T_1, while the pixel values of the second image represent the number of all detected photons. By subtracting the first image pixel values from the second image pixel values, the number of photons with arrival times larger than T_1 can be obtained. This approach is chosen to avoid any accidental overlap or gap between the two respective time windows. In addition, a third image is recorded for visual purposes only. This image is obtained using a time-gating optimized for suppressing the confocal background. However, it is not used for calculating the photon stream-based metric.

In the following, this approach is illustrated for the example of a STED-measurement using crimson beads with a diameter of $48nm$ and an oil objective lens with $NA = 1.35$. The crimson beads are excited by $640nm$ light with a power of $7.4\mu W$ at the back focal plane of the objective lens, and STED light has a power of $83mW$ at the back focal plane of the objective lens. Fluorescence photons are then detected using an APD. xy STED image

at the focal plane is recorded with a FOV of $7.8\mu m$ x $8.9\mu m$, a pixel size of $20nm$ x $20nm$, and a pixel dwell time of $240\mu s$.

Fig. 4.2(a) shows the xy STED image of the crimson beads formed by the photons acquired within $T_1 = 703ps$, which are referred to as early photons. In comparison, Fig. 4.2(b) shows the image of the same FOV formed by photons acquired within the time window of $8ns$, which is comparable to the natural fluorescence lifetime of the crimson beads and contains information of all the photons. To obtain the number of late photons, the photon counts in each pixel of the image with early photons are subtracted from each pixel count of the image with all photons. For the metric calculation, only pixel counts greater than 5 in the image corresponding to all detected photons are taken into account, as this value represents a typical background count observed. In principle, the metric can be calculated for each pixel by determining the ratio of early photon numbers to late photon numbers. Fig. 4.2(c) illustrates the time-gated image.

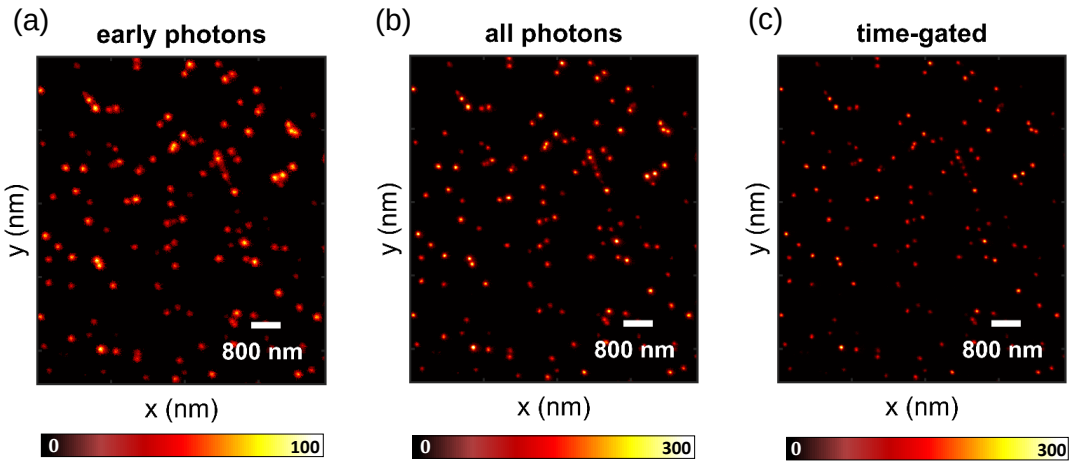

Figure 4.2: Determination of metric by measuring crimson beads with an oil objective lens with *NA* $= 1.35$. (a) xy STED image of beads formed by the early photons acquired within a time window of $703ps$ (b) Image of the same FOV formed by all the photons acquired within a time window of $8ns$. (c) Time-gated image for visual purpose.

4.1.3 Properties of the metric

This section discusses the properties and quality of the photon stream-based metric for aberration correction. The goal of the metric in aberration correction is to exhibit an extremum at the optimal aberration amplitude, representing the highest image quality, thus having a clear dependence on the strength of the aberrations.

To test the effectiveness of the metric, measurements are conducted on a sample consisting of single crimson beads with a diameter of $48nm$ using an oil objective lens with $NA = 1.35$, $640nm$ excitation light with a power of $6.3\mu W$ and STED light with a power of $83mW$ at the back focal plane of the objective lens. Different amplitudes of primary spherical aberrations, ranging from $-80nm$ to $80nm$, are applied to the DM and corresponding xy STED images are acquired at the respective focal plane. As stated in section 3.2.1, the aberration amplitudes are expressed in units of nm rms in this thesis.

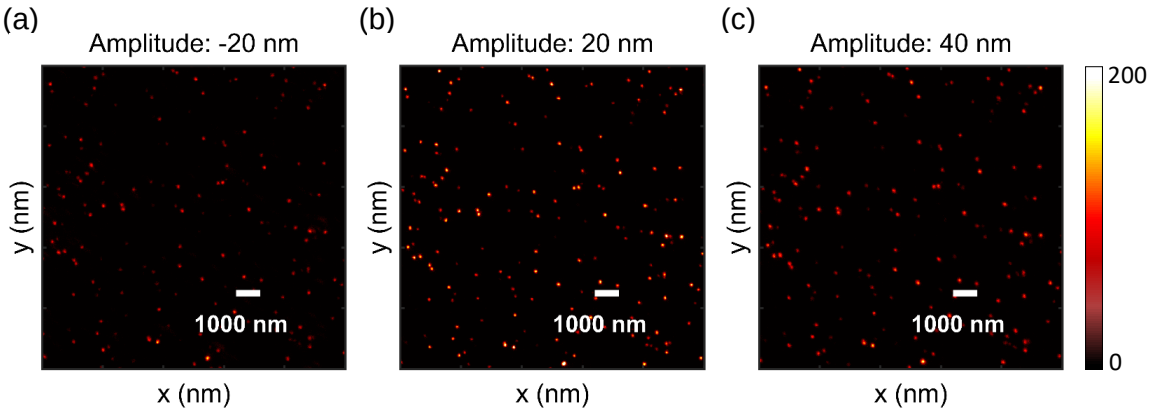

Figure 4.3: xy STED images of crimson beads are obtained using oil objective lens, $640nm$ excitation light while varying amplitudes of primary spherical aberrations are applied to the DM including (a) $-20nm$ (b) $20nm$ (c) $40nm$. The signal levels of the images are normalized relative to the image with $20nm$ amplitude.

Fig. 4.3(a),(b),(c) shows the STED images of the beads for aberration amplitudes of $-20nm$, $20nm$, and $40nm$, respectively. It should be noted that these images are with optimized time gating, which are recorded for visualization purpose, as described in section 4.1.2. When using an oil immersion objective lens with no refractive index mismatch, a primary spherical aberration amplitude of $20nm$ compensates for the residual aberrations present in the microscope setup. This amplitude is considered as a reference for the case without aberration, meaning that the aberration amplitude of 0 corresponds to this compensation level. Upon observation of the presented images, it is evident that the metric's response to the aberration amplitude is equally prominent as the response of the image characteristics. This quality confirms the metric's suitability as a measure for image quality.

For each applied aberration amplitude, the photon stream-based metric is calculated using the previously discussed approach in section 4.1.2. Although the metric can be calculated

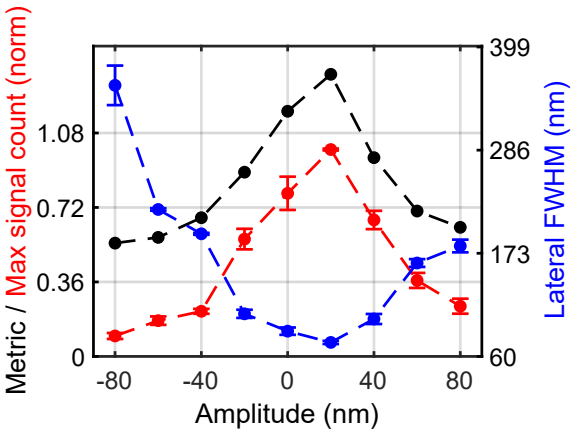

Figure 4.4: Photon stream-based metric values are calculated for each amplitude and plotted as a function of aberration amplitudes (black). Additionally, lateral FWHM (blue) and maximum signal count (red) of the single bead image are also plotted. The photon stream-based metric shows a maximum value at the best image quality which is characterized by the maximum signal count and minimum FWHM. The markers indicate the data points and the dashed lines are used as a visual aid.

for individual pixels, in this case it is calculated by summing the number of early photons over all pixels, and dividing this by the sum of late photons over all pixels with photon counts greater than the background threshold. The resulting metric values are plotted against the aberration amplitudes in Fig. 4.4, which reveals a global maximum at an amplitude of $20nm$, corresponding to an unaberrated image. In addition, Fig. 4.4 displays the lateral FWHM along x axis and maximum signal counts of the single representative bead images as a function of the applied aberration amplitude represented by blue and red, respectively. A line profile is generated by selecting the maximum pixel count in a single bead image. Three consecutive lines are averaged together. The resulting average line profile is then fitted with a Gaussian function. From this fit, the full FWHM and the maximum signal count are derived. The FWHM and maximum signal count are averaged over three representative beads, and the corresponding standard deviation is indicated by the error bar. These results verify that the maximum of the photon stream-based metric matches the best image quality, as characterized by maximum signal counts and minimum FWHM of the bead image.

Since the photon stream-based metric relies on the photo-physical properties of the fluorophore, it is assumed that the metric value is independent of the sample's brightness. Consequently, the optimal aberration amplitude, at same aberration condition of the system, corresponding to the maximum metric value is expected to be independent of the sample brightness. To confirm the conjecture, measurements are performed on a layer of crimson beads using an oil objective lens with $NA = 1.35$ and excitation light at a wavelength $640nm$. The excitation beam has a power of $9.9\mu W$, and the STED beam has a power of $83mW$ at the back focal plane of the objective lens. xy STED images at the

respective focal plane are recorded for different primary spherical aberration amplitudes ranging from $-80nm$ to $80nm$, applied to the DM. Photon stream-based metrics are calculated by summing up the early and late photons over all pixels and then taking the ratio for each aberration amplitude, and are plotted with respect to aberration amplitude.

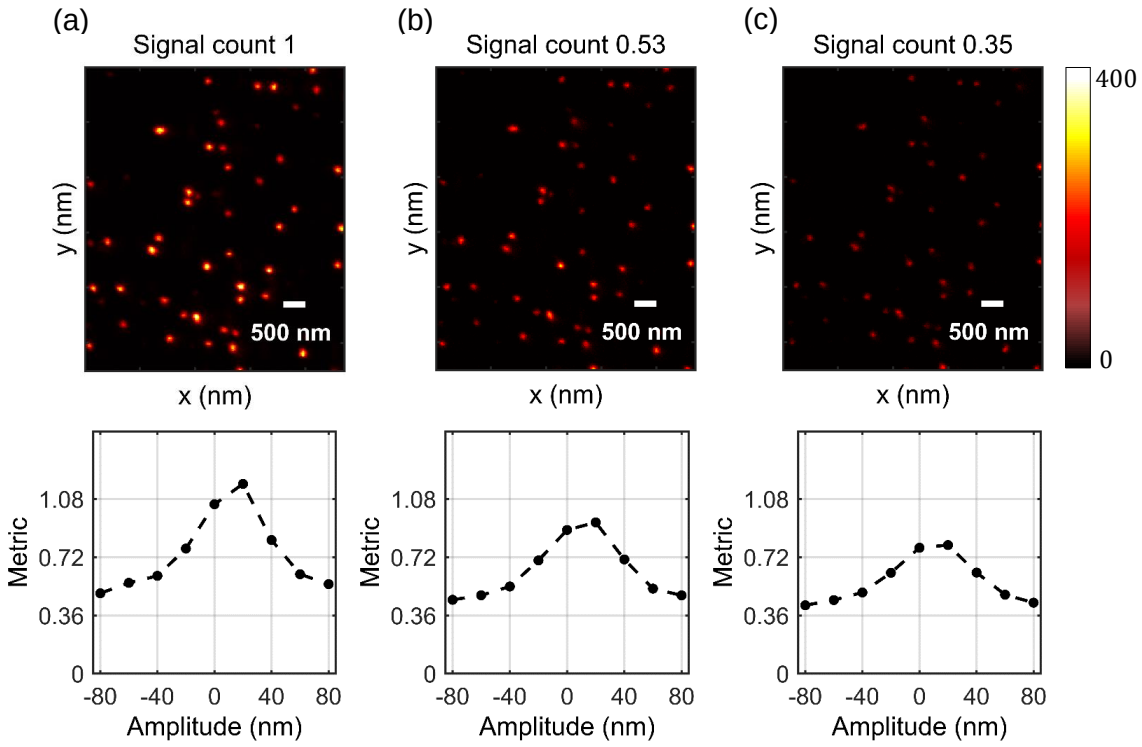

Figure 4.5: To investigate the dependence of the photon stream-based metric on the brightness of the sample measurements are performed on a sample consisting of crimson beads, using an oil objective lens with *NA* $= 1.35$. xy STED images are recorded for different primary spherical aberrations applied to the DM. Same FOV of the sample is measured for different signal counts achieved by exposing the FOV to light and inducing bleaching. Three scenarios includes a high signal counts (a) 47% reduction (b) 65% reduction in signal counts (c). The accompanying xy STED image corresponds to the image obtained at the optimal aberration amplitude, which reflects the maximum metric value. Signal levels of the images are normalized relative to the image with maximum signal count. The x position of the maximum metric value remains unchanged regardless of the brightness of the sample.

The sample's FOV is initially measured, followed by exposing it to both the excitation and STED beams for several runs. This causes the FOV to bleach, resulting in approximately a 47% decrease in signal counts. Similarly, the process is repeated to achieve approximately a 65% decrease in signal counts. Metric curves are generated for each of these scenarios. Fig. 4.5(a),(b),(c) display photon stream-based metric value as a function of aberration amplitudes for three distinct signal counts. The presented xy STED image of

the crimson beads corresponds to the maximum metric, which is obtained at the optimal aberration amplitude. The maximum metric reflects the same aberration amplitude for all the excitation light powers. This observation confirms that the location of the metric maximum, as theoretically expected, does not depend on the brightness of the image.

The photon stream-based metric is also assumed to be independent of the sample's structure, which implies that the optimized aberration amplitude remains the same under the same aberration condition of the optical system, regardless of the sample's structure. To investigate this assumption, first a measurement is performed using a layer of crimson

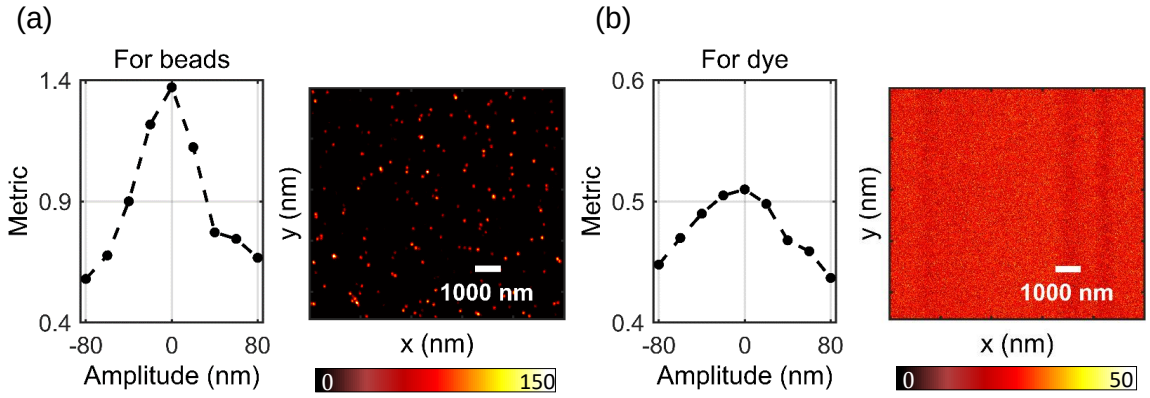

Figure 4.6: To examine how the photon stream-based metric depends on sample structure measurements are conducted using a water objective lens with *NA* $= 1.20$ on (a) crimson beads and (2) homogeneous dye solution under the same experimental conditions. The amplitudes of primary spherical aberration are varied. Metric values are plotted as a function of aberration amplitudes. The maximum values of the metric are observed at $0nm$ amplitude in both cases, indicating that the location of the metric maximum is independent of the sample structure.

beads with a diameter of $48nm$, a water objective lens with *NA* $= 1.20$, and $640nm$ excitation light with a power of $5.2\mu W$ at the back focal plane of the objective lens. Different primary spherical aberration amplitudes ranging from $-80nm$ to $80nm$ are applied to the DM and the corresponding xy STED images at the focal plane are recorded. When using a water immersion objective lens with no refractive index mismatch, the residual aberrations in the setup can be compensated without introducing primary spherical aberration. Thus, in this case, the reference aberration amplitude is 0. Metric values are plotted as a function of aberration amplitudes and as expected Fig. 4.6(a) shows the metric curve with a maximum at aberration amplitude of $0nm$. The accompanying xy STED image of crimson beads corresponds to the aberration amplitude of 0 nm.

Next, measurements are conducted using homogeneous dye (AD-647N, ATTO-TEC, Germany) dissolved in water, under the same experimental conditions. The measurements are performed a few micrometers inside the coverslip to place the detection volume inside the dye solution and avoid any effects due to the coverslip surface. Since the immersion and embedding medium are both water, no change in the primary spherical aberration is expected. Fig. 4.6(b) shows the metric curve as a function of aberration amplitude and the accompanying STED image corresponds to the aberration amplitude of 0 nm. In both cases, the metrics show a maximum at the same aberration amplitude, providing evidence that the optimization of the metric does not depend on the structure of the sample.

4.2 Automation of correction procedure

This section describes the automation of the AO based aberration correction procedure using the photon stream-based metric.

Implementing spherical aberration without creating focal shift

When using a high *NA* objective lens to focus light, defocus cannot be fully characterized by Zernike defocus alone, as listed in Table 1, but requires additional Zernike spherical terms [38]. This implies that modifying any Zernike spherical term of first or higher order would cause a shift in the focus position, resulting in an axial translation of the PSF. When dealing with thin samples, such as a layer of beads, a shift in the focus can lead to a blurry image due to defocus. To distinguish between the image deterioration caused by aberration and the blurring due to defocus, it is necessary to compensate for the axial shift in focus. The range of primary spherical aberration amplitudes used induces a significant shift in focus, while the range of secondary spherical aberration amplitudes used results in negligible focal shifts. In the following, the correction procedure is implemented and tested on thin samples. The axial focal displacement induced by spherical aberration can be minimized by using the DM without any mechanical movement of the objective lens. This can be achieved by applying defocus to the DM, which corrects for the axial shift. To determine the required amplitudes of defocus for each primary spherical aberration amplitudes, the following approach is taken. The measurement is performed using both

an oil objective lens with *NA* $= 1.35$ and a water objective lens with *NA* $= 1.20$ in a crimson bead sample with an excitation wavelength of $640nm$, utilizing the confocal configuration of the microscope. However, only the results obtained using the oil objective lens are presented here.

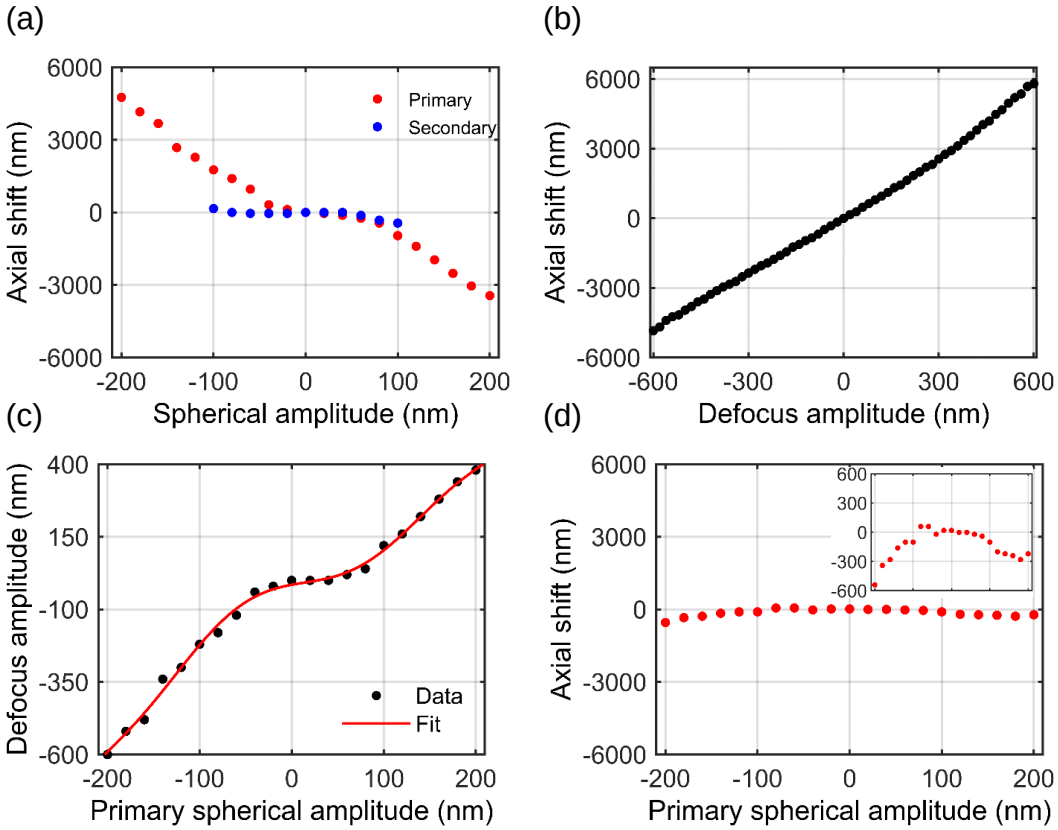

Figure 4.7: The measurement is performed on a layer of single crimson beads using an oil objective lens with a *NA* of 1.35 and an excitation beam wavelength of $640nm$. Different amplitudes of primary and secondary spherical aberration and defocus are applied to the DM and the corresponding PSFs in the xz plane are recorded. The axial shifts of the PSFs with respect to the non-aberrated PSF are measured for (a) different amplitudes of primary spherical aberration (red) and secondary spherical aberration (blue) (b) and defocus. (c) The defocus as a function of primary spherical amplitudes is determined (black data points) and fitted with a polynomial function (red line). (d) After applying the calibration function to the DM, the axial shifts of the PSFs due to primary spherical aberration are minimized. Inset plot shows the same but with resized y axis for better visualization.

Various amplitudes of primary and secondary spherical aberration are applied to the DM in a large range and corresponding PSFs in the xz plane are recorded. The range of applied amplitudes is chosen to fall within the linear regime of the applied and response graph, as depicted in Fig. 3.12 in Section 3.2.3. The axial shifts of the PSFs relative to the non-aberrated PSF are determined. Fig. 4.7(a) displays the axial shifts of the PSFs at

varying primary spherical amplitudes (red), with respect to the PSF at a primary spherical amplitude of 0. The axial shift of the PSFs at varying amplitudes of secondary spherical aberration (blue), relative to the PSF with a secondary spherical amplitude of 0, is also displayed. However, since the axial shift caused by the range of used secondary spherical aberration is insignificant in comparison to primary spherical aberration, the primary focus is on minimizing the axial shift caused by primary spherical aberration. To calculate the axial shifts, the Fourier transform is taken of each PSF image using a fast Fourier transform algorithm. The complex conjugate of one of the Fourier transforms is then computed. These two Fourier transforms are multiplied element-wise, and the resulting product is inverse Fourier transformed using an inverse fast Fourier transform algorithm. The peak value in the resulting image corresponds to the cross-correlation coefficient, while the position of the peak corresponds to the shift. Similarly, various amplitudes of defocus are applied to the DM over a wide range, and the resulting axial shift caused by defocus is determined. Fig. 4.7(b) illustrates the axial shift of the PSFs at varying defocus amplitudes, relative to the PSF at a defocus amplitude of 0. From these two sets of measurements, the amount of defocus required to minimize the axial shift due to each primary spherical aberration is calculated. The data points are fitted with a polynomial function to obtain defocus as a function of spherical aberrations. Fig. 4.7(c) shows the calculated defocus amplitudes at different primary spherical aberration amplitudes (black) with the polynomial fit function (red). This calibration function allows to apply the amplitude of defocus required to compensate for the axial shift, when the amplitude of the primary spherical aberration is changed. Fig. 4.7(d) shows that applying the calibration function to the DM reduces the axial shifts of the PSFs at various amplitudes compared to not applying the calibration function. In order to provide a clearer visualization of the axial shift, the range of the y-axis is reduced in the inset plot. An axial shift of approximately $300nm$ is considered acceptable since it falls within half of the axial extension of the PSF. However, beyond an amplitude of $-160nm$, the axial shift exceeds $300nm$. In practice, to ensure that spherical aberration amplitudes remains within the linear regime of the applied response graph, sample depth and refractive index mismatch are chosen accordingly to restrict the primary spherical aberration from exceeding an amplitude of $160nm$. As the calibration function depends on the depth and refractive index mismatch of the sample, it

may be necessary to repeat the calibration for a specific sample as required.

Software implementation and optimization routine

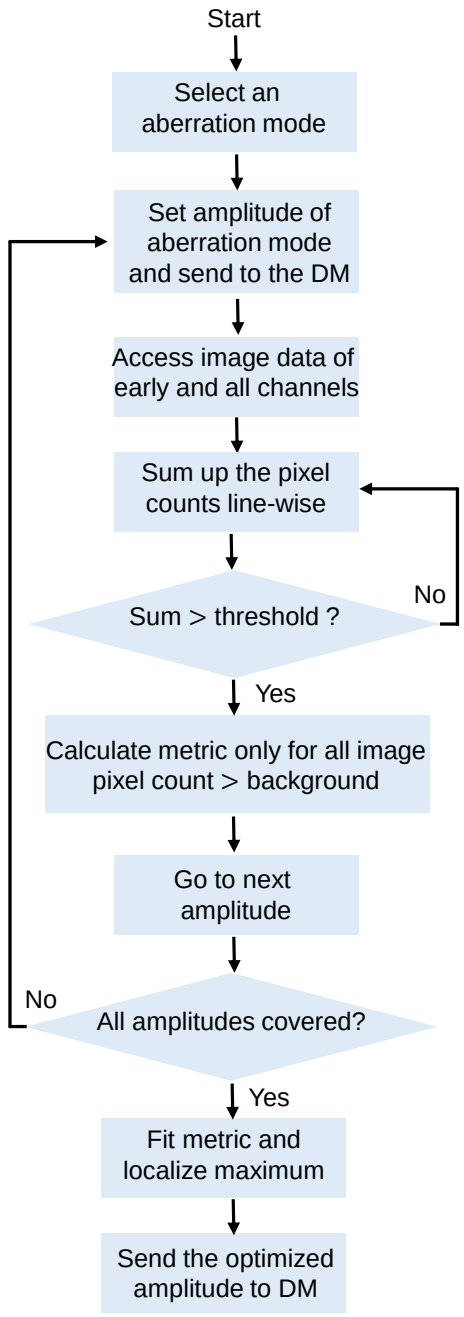

Figure 4.8: Flowchart illustrating the algorithm for the initial optimization of aberration amplitudes using photon stream-based metric.

Python (Python Software Foundation, US) is selected as the programming language, as Imspector offers a Python interface [48] that facilitates the transfer of real time data to Python. Additionally, Python is used to control the DM. To automate aberration correction, specific instructions are executed in parallel with image acquisition. These instructions involve accessing the acquired image data from both 'early' and 'all' time windows, as explained in section 4.1.2, and reading out the pixel values of each line. This evaluation of the data is done in parallel to the data acquisition process. A single or multiple aberration modes are applied sequentially to the DM within a specified amplitude range. The number of amplitudes checked within the range is determined by a given value. For spherical aberration the range is chosen to cover the theoretically predicted amplitudes that correspond to the given depth and refractive index of the sample used. For other aberration modes, a sufficiently wide range of amplitudes is used, which includes both positive and negative values, as well as 0. After the image acquisition process begins, the first amplitude is sent to the DM. At the end of each line in the 'all' image, the pixel counts are summed up. If the sum exceeds a pre-defined photon threshold, the metric is calculated. To determine 'late' photons, the sum of the pixel counts over the line of the 'early'

image is subtracted from that of the 'all' image. Metric is then calculated by dividing the sum of the 'early' photon counts obtained by summing the pixel counts over all the pixels of a line by the 'late' photon counts. Only the pixels in the 'all' image that have photon counts greater than a specified background number are considered in the metric calculation. If the sum of photon counts over a line does not reach the photon threshold, the same procedure is applied to the next line, and the sum of the photon counts over all pixels in both lines is compared to the photon threshold. Once the metric value is calculated for a given aberration amplitude, the next amplitude is sent to the DM and the same procedure is followed. This process is repeated until all the amplitudes within the specified range are covered. The metric values obtained for each amplitude are then fitted using a Gaussian function, and the amplitude corresponding to the maximum metric value is identified from the fit. This amplitude value is then sent to the DM. This entire process is referred to as the initial optimization for a specific aberration mode. A flow diagram of the algorithm is presented in Fig. 4.8.

Influence of photon threshold on the metric

The use of a photon threshold in the optimization routine enhances the robustness of the process by reducing errors due to low signal-to-noise ratios. This subsection investigates how the photon threshold affects both the photon stream-based metric and the initial optimization of aberration amplitude. The analysis is performed as post-processing of STED images of a layer of crimson beads with a diameter of $48nm$. The images are recorded using an oil objective lens with a *NA* of 1.35, $640nm$ excitation beam with a power of $3.5\mu W$, and STED beam with a power of $83mW$ at the back focal plane of the objective lens. Primary spherical aberration amplitudes ranging from $-40nm$ to $60nm$ in $20nm$ increments are applied to the DM, and the corresponding xy STED images at the respective focal plane are recorded with a pixel dwell time of $240\mu s$.

To analyze the impact of the photon count threshold on the metric values, the full FOV of the STED image at the optimum aberration amplitude of $20nm$ is divided into disjoint regions where the sum of photon counts in each region is approximately equal to the photon threshold. The metric values are then calculated for each region, and the average of these values over all regions, along with the corresponding standard deviation, is determined.

This procedure is repeated for a range of photon thresholds up to $50,000$. Fig. 4.9(a) shows the variation of the metric as a function of the photon threshold. As expected, the standard deviation decreases for as the threshold increases. For very small thresholds < 1000, the error associated with a metric may jeopardize the optimization process.

To assess how the photon threshold affects the automatic optimization process, it is not sufficient to only consider the standard deviation. The metric stroke over the range of tested aberration amplitudes must also be taken into account. Using the same approach as discussed above, STED images obtained at varying aberration amplitudes are partitioned into non-overlapping regions, and the average metric values and their corresponding standard deviations are computed. This is repeated for photon thresholds ranging from 500 to $50,000$. Fig. 4.9(b) shows a metric curve for a photon threshold of $20,000$. To assess the stability of the metric curve, a quantity named as relative error is calculated for each metric curve at different photon thresholds. The relative error is obtained by dividing the mean of the standard deviations of the metric values at each aberration amplitude by the metric stroke, which is defined as the difference between the maximum metric value (at $20nm$ aberration amplitude) and the minimum metric value (at $-40nm$). Fig. 4.9(c) shows the relative error as a function of the photon threshold. A photon threshold above $20,000$ results in a relative error below 0.1, indicating a reproducible metric curve.

In order to verify that this threshold allows for a reliable initial optimization, the initial optimization is repeatedly performed on the recorded STED images. For this, instead of accessing the image data and applying different aberration amplitudes during an image acquisition, the pre-existing STED images at the respective aberration amplitudes are analyzed. The initial optimization step is repeated until the full FOV is covered, generating multiple metric curves for each photon threshold. A Gaussian function is fit to each curve to determine the optimum aberration amplitude. This procedure is repeated for different photon thresholds ranging from $2,500$ to $40,000$. Fig. 4.9(d) illustrates the optimized amplitude as a function of photon number presented using boxplot formalism for better understanding of the distribution of the optimized amplitudes. The blue box represents the interquartile range, with the top and bottom edges indicating the $75th$ and $25th$ percentiles of the data sets, respectively. The red line represents the median, while the extreme black lines represent the maximum and minimum values of the data sets,

excluding outliers. The red plus signs indicate outliers.

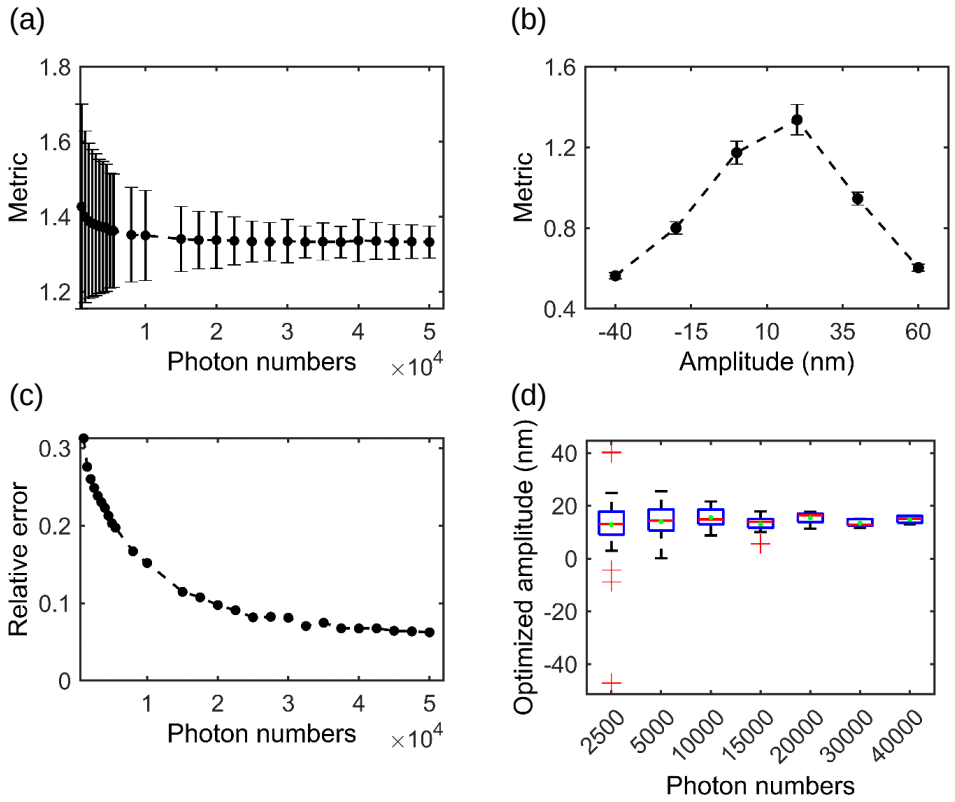

Figure 4.9: Influence of the photon threshold on both the metric and optimization process. The measurements are conducted on a layer of crimson beads with a diameter of $48nm$, using an oil objective lens with a *NA* of 1.35, a $640nm$ excitation beam with $3.5\mu W$ power, and a STED beam with a power of $83mW$ at the back focal plane of the objective lens. A range of primary spherical aberration amplitudes, from $-40nm$ to $60nm$ in steps of $20nm$, are applied to the DM, and the corresponding xy STED images at the respective focal plane are recorded. The impact of photon numbers is analyzed by post-processing the recorded images. To analyze the effect of photon numbers, the FOV of the STED images is divided into non-overlapping multiple boxes, each containing a certain photons threshold, and metrics are calculated for each box. The average metric and corresponding standard deviation are determined, and the same procedure is repeated for a next higher number of photon threshold. (a) The resulting average metric over the boxes and the corresponding standard deviation are plotted as a function of photon threshold, using the image with a $20nm$ aberration amplitude. (b) An example of metric curve showing metrics as a function of aberration amplitude using the photon threshold of 20000. (c) Relative error is plotted as a function of the photon numbers. The relative error is calculated by dividing the mean of the standard deviations of the metric values at each aberration amplitude for a given metric curve by the metric stroke. The metric stroke is defined as the difference between the maximum and minimum metric values of the same curve. (d) Boxplot-style visualization of the optimized aberration amplitudes as a function of photon number.

Experimental verification confirms that there is no significant effect on image quality within a fluctuation range of $\pm 5nm$ around the optimized amplitude. The results of the analysis indicate that a photon threshold of $\geq 20,000$ ensures a stable optimization. Since a higher

threshold results in a longer optimization time, a threshold of $20,000$ will be used in the following. It is important to note that this conclusion is specific to the experimental conditions employed as it takes into consideration various factors such as the metric stroke, the number of amplitude values tested which contribute to the number of sampling points for the fit, and the various sources of noise such as shot noise and signal background from stray light. As such, it is crucial to acknowledge that the conclusion may not necessarily hold true for other experimental scenarios.

Successful initial optimization of a single aberration

To test the displacement free initial optimization routine for aberration amplitude in xy STED imaging modality, measurement is performed on a layer of crimson beads using a water objective lens with *NA* $= 1.20$. The FOV is $10\mu m$ x $12\mu m$, with a pixel size of $20nm$ x $20nm$, and a pixel dwell time of $240\mu s$. $640nm$ excitation light has a power of $2.1\mu W$ at the back focal plane of the objective lens, while STED light has a power of $92mW$ at the same plane. The primary spherical aberration amplitudes are varied from $-80nm$ to $80nm$ in $20nm$ increments, with a photon threshold set at $20,000$. The results are shown in Fig. 4.10.

In Fig. 4.10(a), the xy STED image of crimson beads displays the stepwise optimization until the position of the metric maximum is found. Fig. 4.10(b) displays the metric values obtained during the initial optimization for each aberration amplitude. The blue line represents the fitted metric curve. Upon fitting, the optimized primary spherical amplitude is determined to be $\sim 0nm$. Once the first amplitude ($-80nm$ in this case) is sent to the DM, the metric value is calculated only after acquiring $20,000$ photons, constituting one iteration. The DM then is set to the next amplitude. Even after the initial optimization is completed, metric values continue to be calculated across the FOV for monitoring purposes. In Fig. 4.10(c), all the metric values are plotted as a function of iterations. The blue points represent the metric values obtained during the initial optimization, while the green points represent the metric values during the rest of the image acquisition. To provide a clearer visualization of the initial optimization, an inset plot is included, displaying the metric values specifically during initial optimization. The standard deviation of all the metric values obtained during the remaining image acquisition is ~ 0.17, which is nearly

equal to the standard deviation calculated in Fig. 4.9(a) at a photon threshold of $20,000$, which was ~ 0.15.

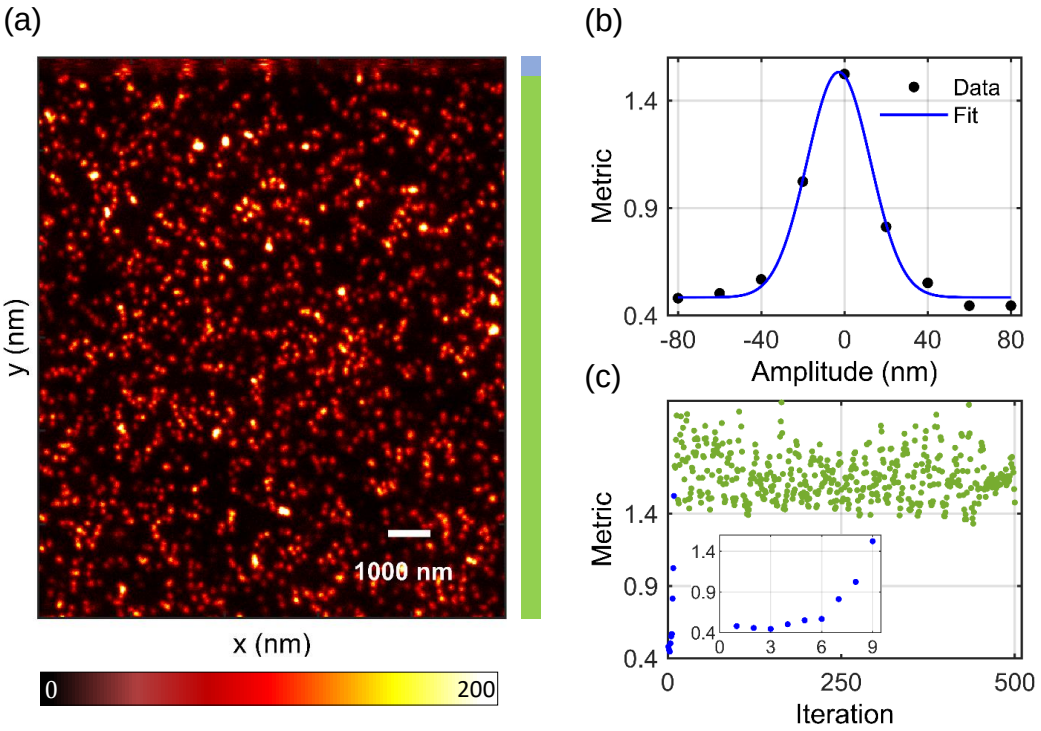

Figure 4.10: Successful testing of automated optimization routine on a layer of crimson beads in xy STED imaging modality. A water objective lens with *NA* $= 1.20$, $640nm$ excitation light are used for measurement. Primary spherical aberration amplitudes are varied from $-80nm$ to $80nm$ in $20nm$ step size. The DM is given instructions to apply the next deformation only after measuring $20,000$ photons and calculating a single metric value. This process is referred to as one iteration. Photon stream-based metrics are calculated for each amplitude and fitted with a given Gaussian function. Finally, the DM is set at the amplitude where metric is maximum, derived from the fit. (a) xy STED image with the optimization process, where blue band represents the initial optimization and green band represents the rest of the image acquisition. (b) The metrics obtained during initial optimization, are plotted as a function of aberration amplitudes, with the blue line representing the fit. (c) Metric values are plotted as a function of all iterations, which include the initial optimization (represented by blue points) as well as the subsequent image acquisition (represented by green points). Inset plot shows the metric values during initial optimization.

4.3 Automatic correction of multiple aberration modes

The accurate imaging of thick biological specimens requires the identification and correction of relevant aberration modes. To determine the specific aberration modes that require

correction, a thorough review of the relevant literature is conducted. The literature search reveals that Zernike polynomials with $j = 5$ (primary astigmatism oblique), $j = 6$ (primary astigmatism vertical), $j = 7$ (primary coma vertical), $j = 8$ (primary coma horizontal), $j = 9$ (primary trefoil oblique), $j = 10$ (primary trefoil vertical), $j = 11$ (primary spherical), $j = 12$ (secondary astigmatism oblique), $j = 13$ (secondary astigmatism vertical), $j = 14$ (primary tetrafoil oblique), $j = 15$ (primary tetrafoil vertical) are typically used for aberration correction [4, 49, 50, 51]. These polynomials include those up to the fourth radial order. Depending on the focusing depth within the specimen, higher radial order polynomials, $j = 22$ (secondary spherical) may also be necessary [17, 19, 20, 52, 53].

This section aims to evaluate the efficacy of the photon stream-based metric in assessing the quality of images affected by aberrations represented by $j = 5 - 17$ and $j = 22$. Furthermore, the automated aberration correction algorithm is implemented to correct multiple aberrations on a bead sample.

To investigate the behaviour of the photon stream-based metric for different aberration modes, measurements are conducted on a layer of crimson beads with a diameter of $48nm$ using an oil objective lens with *NA* $= 1.35$, $640nm$ excitation light, and STED light with powers of $6.3\mu W$ and $83mW$, respectively, at the back focal plane of the objective lens. Different amplitudes of the respective aberration modes are applied using the DM and the corresponding xy STED images are recorded with a FOV of $10\mu m$ x $10\mu m$, a pixel size of $20nm$ x $20nm$, and a pixel dwell time of $400\mu s$ at the focal plane. For each aberration amplitudes, photon stream-based metric is calculated following the approach presented in section 4.2.2. Additionally, lateral FWHM and maximum signal count of individual representative bead image are also determined. The analysis is repeated for all the aberration modes applied. Fig. 4.11 presents the photon stream-based metric (black), lateral FWHM (blue), and maximum signal count (red) as a function of aberration amplitudes for various aberration modes, including primary astigmatism vertical $(j = 6)$, primary coma horizontal $(j = 8)$, primary trefoil vertical $(j = 10)$, primary spherical $(j = 11)$, secondary astigmatism vertical $(j = 13)$, primary tetrafoil vertical $(j = 15)$, secondary coma vertical $(j = 18)$, and secondary spherical $(j = 22)$.

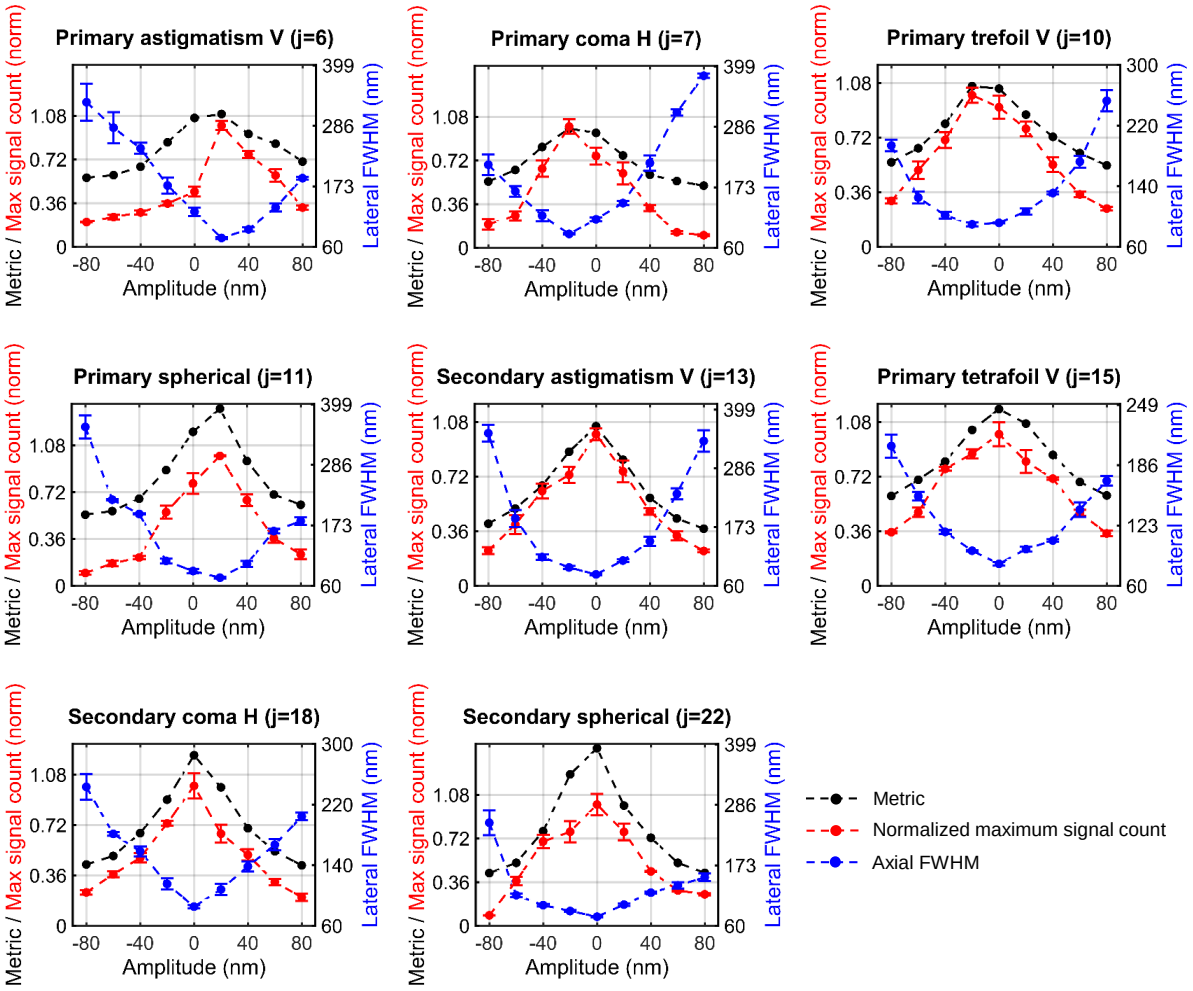

Figure 4.11: Analysis of metric behaviour and image quality for different aberration modes using STED images of $48nm$ beads measured with an oil objective lens with $NA = 1.35$ and $640nm$ excitation light. The plots depict the photon stream-based metric (black), lateral FWHM (blue), and maximum signal counts (red) as a function of aberration amplitudes, with the maximum signal count normalized to that of a non-aberrated bead image. The results show that the metric reached its maximum at the amplitude that correspond to the best STED resolution and brightness for all aberration modes, indicating the optimal image quality. The dashed lines are used as a visual aid.

In situations where an aberration mode occurs in two orientations, such as vertical and horizontal, or oblique and vertical, only one orientation is tested, and it can be assumed that the same results will apply to the other orientation. Additionally, for aberration modes like coma and astigmatism at higher amplitudes, the lateral PSF becomes asymmetric. In such cases, the FWHM along the more extended direction is considered. The maximum signal count is normalized with respect to the maximum signal count of the non-aberrated representative bead image. The graphs demonstrate that for all aberration modes, the metric reaches its maximum at the amplitude that corresponds to the image with the max-

imum brightness and minimum FWHM, indicating the best image quality.

The optimization algorithm is extended to allow for sequential optimization of multiple predefined aberration modes. Once the optimization for a particular mode is finished, the optimized value is sent to the DM, and the algorithm proceeds to optimize the next mode. To demonstrate this capability, the automated optimization algorithm is applied to correct for multiple aberration modes in a sample consisting of two coverslips that contain crimson beads with a size of $48nm$, as illustrated in Fig. 3.13. The coverslips are separated by a specific amount of embedding medium, 20% of thiodiethanol creating a depth of $30\mu m$. The embedding medium has a refractive index of $n_2 = 1.37$. The measurements are conducted using a $60X$ water immersion objective lens with *NA* $= 1.20$, and the excitation and STED light have powers of $5.2\mu W$ and $53.8mW$, respectively, at the back focal plane of the objective lens. The objective lens is focused on the layer at $z = 30\mu m$. In order to purposefully introduce some coma at $z = 30\mu m$ the sample is slightly tilted with respect to the objective lens. The FOV is $14\mu m$ x $20\mu m$, with a pixel size of $20nm$ x $20nm$, and a pixel dwell time of $240\mu s$. During the acquisition of the xy STED image, automated optimization of aberration amplitude is performed with a photon threshold set at 8000. To accurately determine the optimized amplitude, an initial optimization is performed for each relevant aberration mode. This involves testing a wide range of amplitudes from $-60nm$ to $140nm$. It is worth noting that the photon threshold used is lower than the preferred threshold of $20,000$ concluded in section 4.2 for optimization on a bead sample. However, it is also stated in section 4.2 that the stability of the metric curve depends on the number of amplitude values tested. In this case, 15 amplitude values are tested within the range, whereas in section 4.2, only 6 values were tested. As the number of sampling points increases compared to those presented in Fig. 4.9, a lower photon threshold can be expected to maintain the same stability of the metric curve. The optimized amplitude for the maximum metric is then derived by fitting the metric curve. The same procedure is sequentially followed for all the aberration modes, including $j = 5$ (primary astigmatism oblique), $j = 6$ (primary astigmatism vertical), $j = 7$ (primary coma vertical), $j = 8$ (primary coma horizontal), and $j = 11$ (primary spherical).

The Fig. 4.12(a) illustrates the xy STED image without aberration correction. In Fig. 4.12(b), the upper third of the image shows the sequential optimization of each aberration

mode. The white dashed lines in the figure indicate the completion of optimizing each aberration mode, following the sequence of primary coma horizontal, primary coma vertical, spherical aberration, primary astigmatism vertical, and primary astigmatism oblique.

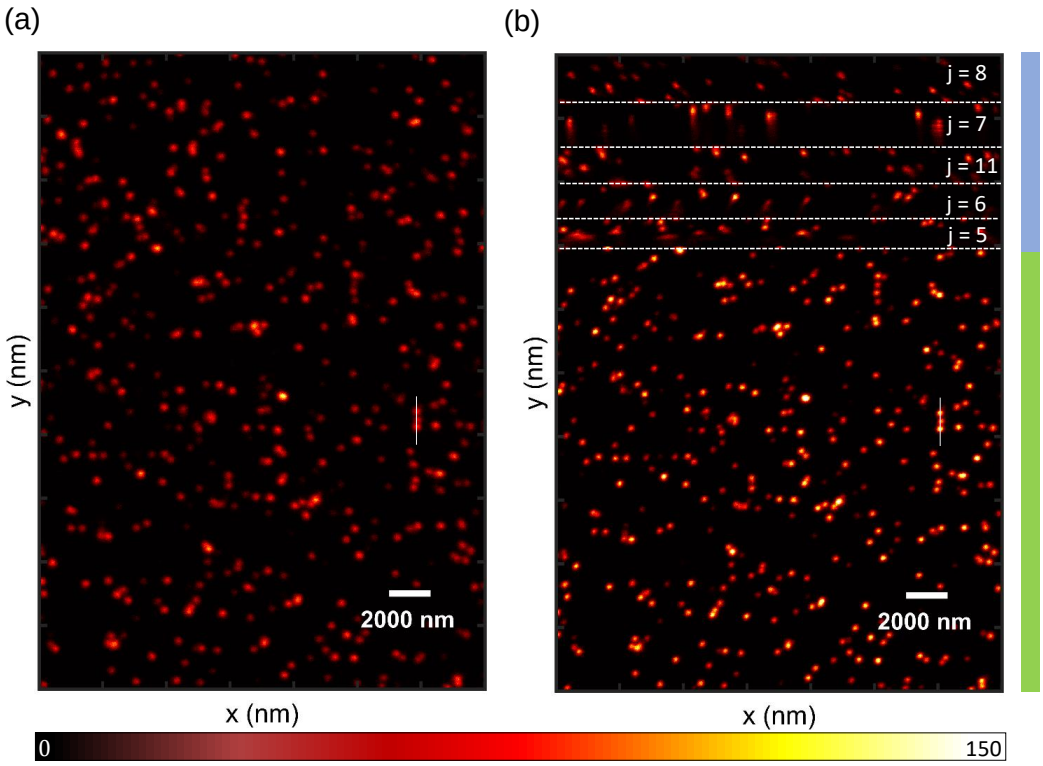

Figure 4.12: Optimization of multiple aberration modes is performed at depth of $30\mu m$ through a refractive index mismatch of $\Delta n = 0.04$ on a sample consisting two layers of crimson beads. Measurement is performed using a water objective lens, $640nm$ excitation and xy STED imaging modality. (a) Uncorrected STED image (b) Corrected STED image where initial optimization for multiple aberration modes is visible in the upper third of the image indicated by the blue band and the green band indicates the rest of the image acquisition. Each white dashed line in the indicates the completion of optimization for one aberration mode, starting from primary coma horizontal, primary coma vertical, spherical aberration, primary astigmatism vertical, and primary astigmatism oblique, in that sequence.

In the remaining part of the image in Fig. 4.12(b), both brightness and resolution are significantly improved compared to the uncorrected image. An example of the optimization process considering the primary coma horizontal is presented in Fig. 4.13(a). Fig. 4.13(b) shows an exemplary line profile through a few beads, as indicated by the white line in Fig. 4.12(a) and (b), demonstrating a substantial enhancement in brightness and resolution after aberration correction. Furthermore, Fig. 4.13(c) displays the optimized amplitudes of the corrected aberration modes, with the x axis representing the Noll index

of the relevant aberration modes. As expected, the results reveal that primary coma horizontal $(j = 8)$ has the most significant contribution. The amplitude of primary astigmatism oblique $(j = 5)$, primary astigmatism vertical $(j = 6)$, and primary coma vertical $(j = 7)$ are required to compensate for the residual aberration from the imaging system. On the other hand, the amplitude of primary spherical $(j = 11)$ is needed to correct the spherical aberration that is created due to the refractive index mismatch of the sample at the depth where the light is focused.

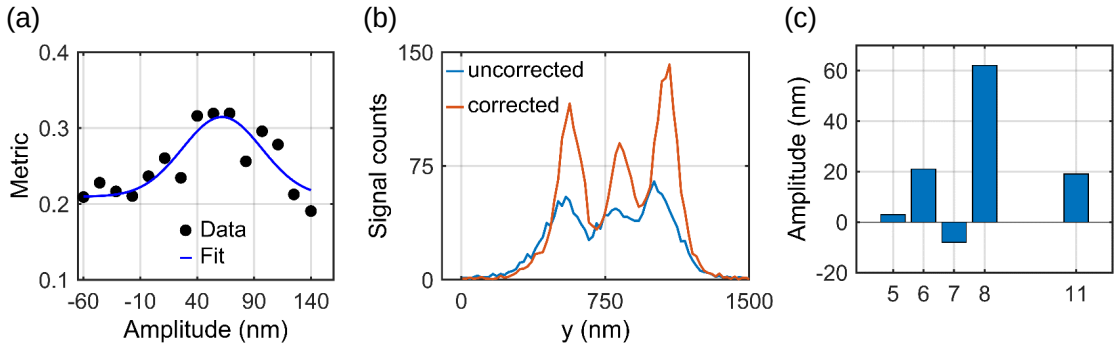

Figure 4.13: Multiple aberration correction. (a) An example of initial optimization of primary coma horizontal (b) The line profile drawn through the beads, as indicated by the white line in Fig. 4.12(a) and (b) , shows the improved image quality due to aberration correction. (c) Bar plots represent the optimized amplitudes of various aberration modes including $j = 5$, $j = 6$, $j = 7$, $j = 8$ and $j = 11$. As the sample was deliberately tilted with respect to the objective lens to introduce coma, the dominant amount of coma, $j = 8$ is expected.

4.4 Continuous optimization of aberration

In this section, the automation of aberration correction using the photon stream-based metric algorithm is improved to incorporate continuous optimization after initial optimization. Within a thick biological specimens, aberrations may change over the FOV or during image acquisition if the focusing depth is altered. To address this issue, continuous optimization has been implemented to detect any aberration changes and compensate for them accordingly.

Continuous optimization routine

After completing the initial optimization process, a continuous optimization process begins and cycles for the remainder of the image acquisition. During each cycle, the algorithm modifies the initially optimized amplitude, denoted as a_0, by a step in either direction while determining the corresponding metric values for all three amplitudes. The step size is chosen such that the metric values are expected to change while keeping the change of image quality at a minimum. Through experimental observation, it is determined that a step size of approximately $5 - 10nm$ is suitable, as can be seen in Fig. 4.4 and Fig. 4.12. The obtained metric values are evaluated through a two-step process: significance check and maximum search. First, the change in the metric values, calculated as the maximum value minus the minimum value, is checked for its significance. This expected change is derived from the initial optimization step and compared to the full range of metric values obtained during that step. A change greater than $5-10$% of the full range is considered significant for typical optimization parameters. If the change is not significant, the tested amplitude range is extended by up to two more steps, one in either direction, and the metric values are re-evaluated for each amplitude. If the change in metric values is significant, a quadratic function of the tested amplitudes is fitted to the metric values $M(a)$, where a represents the tested amplitude. The quadratic function can be expressed as $M(a) = b_0 + b_1\,a + b_2\,a^2$, where b_0,b_1,b_2 are the fitting parameters. Using the fitting parameters, the zero point of the first derivative, represented as $-\frac{b_1}{2\,b_2}$, is determined. Three cases are distinguished based on the location of the zero point:

i) If the fitting function does not have a maximum and the tested range has less than 5 steps, the range is extended up to a maximum of 5 steps and the metric values are re-evaluated each time.

ii) if a maximum exists, as indicated by a negative second derivative of $M(a)$ with respect to a, and its position falls within the range of tested amplitudes, the x-coordinate of the maximum is taken as the new optimized amplitude, and a_0 is replaced by the new value.

iii) In the case that the x-coordinate of the maximum falls outside the tested amplitude range, the search continues to increase the robustness of the maximum determination. This continues until either a maximum number of steps is reached or a new optimized value is found as in case ii). To achieve this, the slope of the fit function is determined

at the center of the tested amplitudes, a_0, and its sign is checked. If the sign is positive, the tested range is extended by one step in the positive direction, and if it is negative, the range is extended in the negative direction.

The optimization cycle continues until a new optimized amplitude is found, or until a given number of steps is reached without any significant change or without finding a maximum within the tested amplitude range. In such cases, the original amplitude, a_0, is retained and used as the starting point for the next optimization cycle of the same aberration mode.

Continuous optimization of the primary spherical aberration

To test the effectiveness of continuous optimization, a sample consisting of two coverslips with crimson beads, with a diameter of $48nm$, is used. As shown in Fig. 3.13, the coverslips are separated by an embedding medium, thiodiethanol, with a refractive index of $n_2 = 1.448$, resulting in a distance of $16\mu m$ between them. The measurement is performed using an oil objective lens. Since the refractive index of the immersion medium, $n_1 = 1.518$, is different from the refractive index of the embedding medium, the strength of the primary spherical aberration varies in the two planes of the coverslips.

The powers of $640nm$ excitation light and STED light are set to $2.7\mu W$ and $83mW$, respectively, at the back focal plane of the objective lens. During xy STED measurements, the initial focus is set on the first plane, $z = 0$. About one-third of the way through image acquisition, the sample is shifted axially to bring the second plane, $z = 16\mu m$, into focus. After a little over two-thirds of the image acquisition, the focus is returned to the first plane, $z = 0$. It has been verified that the focus changes occur within $1 - 2$ lines, ensuring that any deterioration in image quality is due to aberrations rather than the axial position settings.

Fig. 4.14(a) displays the xy STED image acquired during the entire optimization process, which includes both initial optimization and continuous optimization. The blue band at the top of the image represents the initial optimization and the green band indicates the continuous optimization. It is important to note that in continuous optimization, a significantly higher photon threshold is employed due to the utilization of only a few tested amplitudes. During a line scan of 600 along the y direction, the focus is shifted to the $z = 16\mu m$ plane. This change is clearly visible in the zoomed version 1 of the image, where a decrease

in image quality is observed immediately after the plane change due to the presence of spherical aberration.

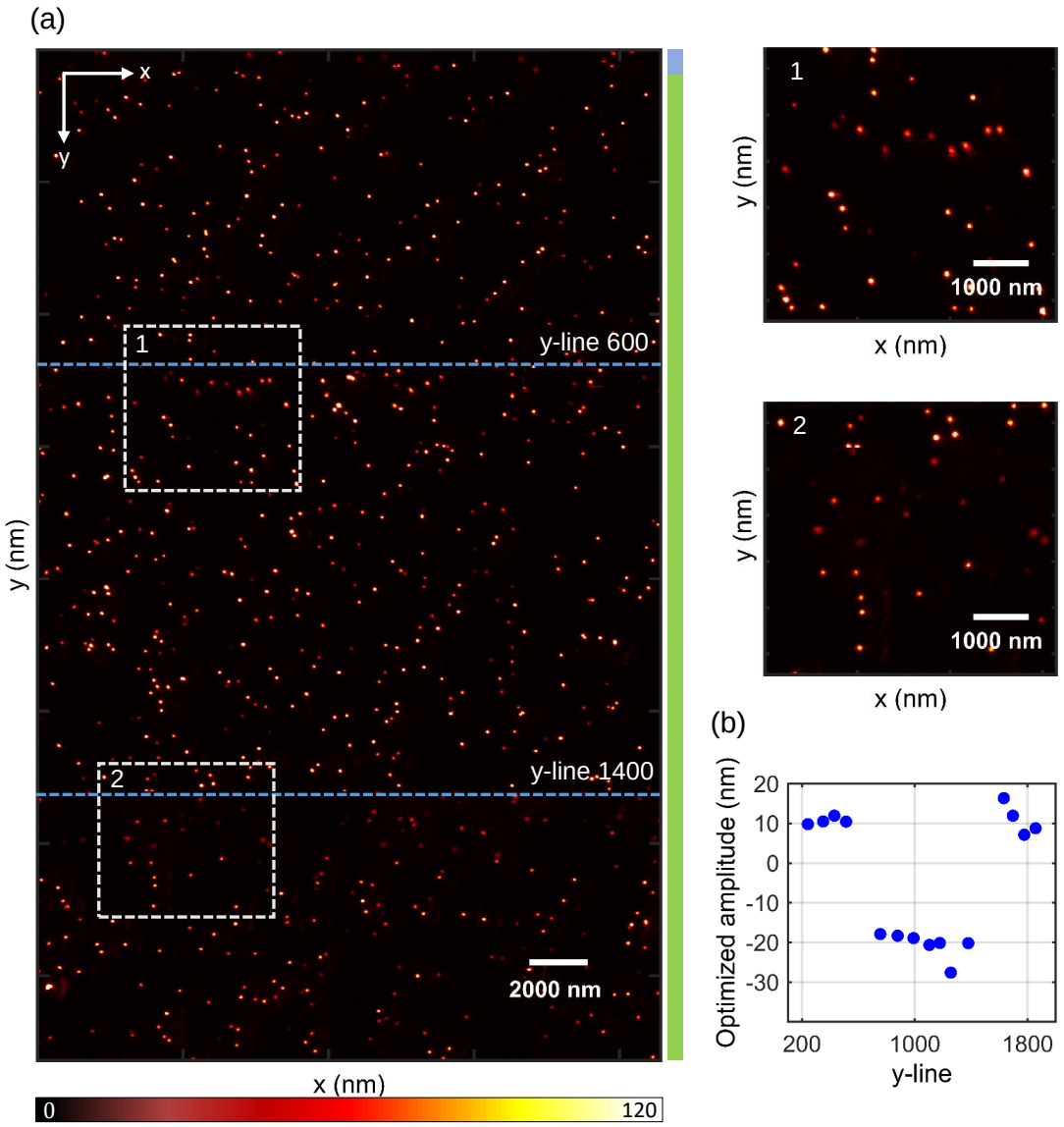

Figure 4.14: Continuous optimization tested on a sample consisting of crimson beads mounted on two layers separated by a distance of $16\mu m$ with embedding medium with a refractive index of 1.448. STED imaging is performed using an oil objective lens with a *NA* $= 1.35$, $640nm$ excitation beam with a power of $2.7\mu W$ and STED beam with a power of $83mW$ at the back focal plane of the objective lens. Due to the difference in refractive indices between the embedding medium and the immersion medium 1.518, the strength of primary spherical aberration is different at the two layers. The initial focus was set at layer 1, which is close to the objective lens. (a) xy STED image shows the initial optimization indicated by the blue band, and the green band indicates continuous optimization of the primary spherical aberration. Blue dashed lines indicate when focus is switched from layer 1 to layer 2 and then from layer 2 to layer 1. Enlarged sections of the image show the optimization of image quality after each focus change. (b) Continuously optimized amplitude of the primary spherical aberration plotted against the lines in the y direction.

However, continuous optimization detects and corrects the aberration within a few line scans, as can be seen in the improvement of image quality. Later, during the line scan of 1400, the focus is set back to the $z = 0$ plane, which results in a degradation of image quality, as shown in zoomed version 2. Nonetheless, continuous optimization once again detects and corrects the aberration, leading to an improvement in image quality. In Fig. 4.14(b), the continuously optimized amplitude of the primary spherical aberration is plotted as a function of the y scan line. The initial optimization phase is completed before line 200, with the optimized amplitude derived from the fitting of the metric curve being $10nm$. From lines 200 to 600, the focus is set at $z = 0$, which is reflected in the plot of the continuously optimized amplitudes. However, after line 600, the amplitudes remain around $-20nm$ due to the change in focus to $z = 16\mu m$. Subsequently, after line 1400, the focus is brought back to $z = 0$, which is reflected in the plot by a continuously optimized amplitude of around $10nm$.

4.5 Application to biological STED imaging

This section validates the automated aberration correction algorithm using the photon stream-based metric in biological samples, both in flat cells and thick tissues.

4.5.1 Optimization of aberration in a thin cell

The sample used for this validation is a microtubule network that is fluorescently labeled with abberior star635P (Abberior Star 635P NHS ester, Abberior, Germany) in a Vero cell that is growing flat on a cover glass. Microtubules are a part of the cytoskeleton in eukaryotic cells and are long, hollow, cylindrical filaments composed of polymerized dimers of alpha and beta tubulin. The outer diameter of a microtubule is approximately $25nm$.

Sample preparation

Cells are cultured onto cover glasses and incubated in cell culture medium at 37° C with 5% CO_2. The cover glasses are washed with phosphate buffered saline (PBS, P5493,Sigma-Aldrich, Germany) and then fixed with cold methanol for five minutes. After removing the

methanol, the cells are washed again with phosphate buffered saline and incubated in a blocking solution (2% bovine serum albumin fraction in phosphate buffered saline) three times for five minutes each. The cover glasses are then incubated in a primary antibody (Anti-alpha-tubulin mouse, Sigma-Aldrich, Germany) diluted in phosphate buffered saline for one hour at room temperature. After washing the cover glasses with blocking solution three times for five minutes each, they are incubated in a secondary antibody (Star 635P goat anti-mouse, Abberior, Germany) staining solution for one hour at room temperature while being shielded from light. The cover glasses are then washed three times with phosphate buffered saline for five minutes each time, and the embedding medium, mowiol is added. Finally, a second cover glass is placed on top of the sample and sealed using two-component silicon glue (Picodent twinsil 22, Picodent, Germany).

Application of the optimization routine

The optimization algorithm to correct multiple aberration modes, utilizing the continuous optimization protocol, is applied on a layer of microtubule network. The measurement is taken using an oil objective lens with an *NA* of 1.35, $640nm$ excitation beam, and STED beam with powers of $1.53\mu W$ and $96mW$, respectively, at the back focal plane of the objective lens. The measurement is performed in a FOV of $30\mu m$ x $41.2\mu m$ with a pixel size of $20nm$ x $20nm$ and a pixel dwell time of $100\mu s$. The DM applies various aberration modes, including primary astigmatism oblique $(j = 5)$, primary coma horizontal $(j = 8)$, primary spherical $(j = 11)$, and secondary spherical $(j = 22)$, with amplitudes ranging from $-80nm$ to $80nm$ in increments of $20nm$. In the optimization algorithm, the photon threshold need to be adjusted according to the specific sample being used. Since biological samples exhibit structural inhomogeneity and variations in dye concentration, a higher photon threshold is necessary to obtain a stable metric curve and reduce relative errors in metric values. It has been verified that setting a photon threshold of $200,000$ produces stable metric curves.

Initial optimization is performed sequentially for all four aberration modes, and the optimized amplitudes of the respective modes are obtained through fitting the metric curve. These optimized amplitudes are then sent to the DM. Once the initial optimization for all aberration modes is completed, continuous optimization is applied to the primary spherical

aberration. This continuous optimization process follows the algorithm outlined in section 4.4. Significance checks are conducted on the changed metric values, and at certain iterations, maximum metric values are identified. These maximum metric values indicate new optimized amplitudes.

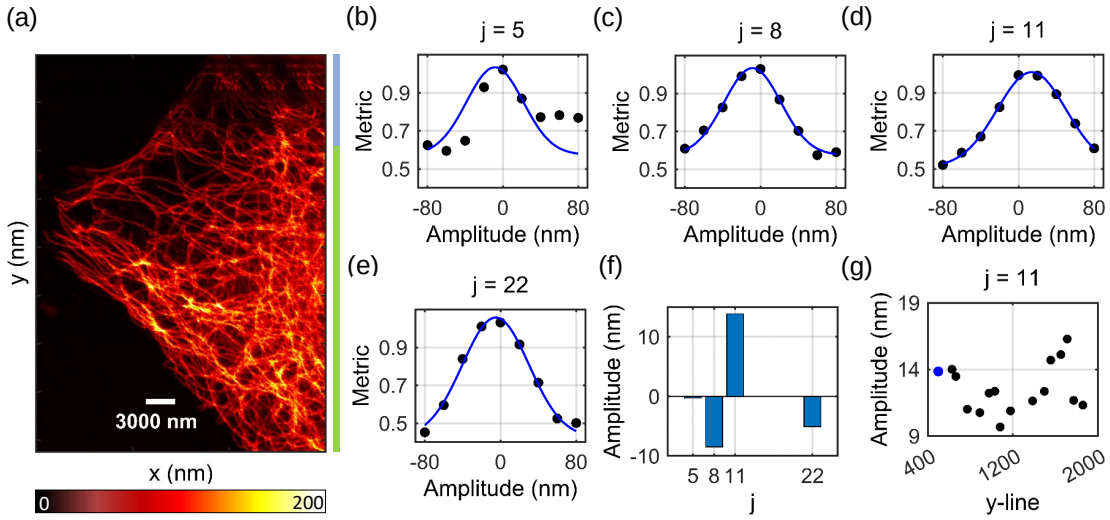

Figure 4.15: Optimization of multiple aberration modes including continuous optimization protocol on a layer of microtubule network fluorescently labeled with abberior star635P. Measurement is performed using an oil objective lens with *NA* $= 1.35$, $640nm$ excitation light with a power of $1.53\mu W$, STED beam with a power of $96mW$ at the back focal plane of the objective lens. Different aberration modes including primary astigmatism oblique $(j = 5)$, primary coma horizontal $(j = 8)$, primary spherical $(j = 11)$, and secondary spherical $(j = 22)$, with amplitudes ranging from $-80nm$ to $80nm$ in increments of $20nm$ are applied to the DM. (a) xy STED image showing the initial optimization of all four aberration modes indicated by the blue band with a photon threshold of $200,000$. The green band indicates the rest of the image acquisition with continuous optimization of primary spherical aberration. Metrics obtained during the initial optimization as a function of the amplitudes, with the blue line indicating the fitting of the metric curve with a Gaussian function for (b) primary astigmatism oblique, (c) primary coma horizontal, (d) primary spherical, and (e) secondary spherical. (f) Bar plots represent the optimized amplitudes of various aberration mode. (g) During continuous optimization of primary spherical aberration newly optimized amplitudes (black points) are plotted with each y-line where they are found. Blue point indicates the initially optimized amplitude.

Fig. 4.15(a) illustrates xy STED image of the microtubule network, where the blue band represents the initial optimization for all four aberration modes, and the green band corresponds to the remaining image acquisition with continuous optimization of primary spherical aberration. The metrics obtained during the initial optimization of primary astigmatism oblique, primary coma horizontal, primary spherical, and secondary spherical aberrations are plotted in Figs. 4.15(b),(c),(d),(e), respectively, as a function of the aberration amplitudes. The blue line in each plot represents the fitting of the metrics, and the optimized

amplitudes are determined to be $-0.25nm$, $-8.46nm$, $13.85nm$, and $-5.06nm$, respectively. Fig. 4.15(f) presents a bar chart depicting the initially optimized amplitudes. Fig. 4.15(g) illustrates the continuously optimized amplitudes of the primary spherical aberration as a function of line number along y direction. The blue point on the graph represents the initially optimized amplitude, and it can be observed that the continuously optimized amplitudes remain within a range of $\pm 5nm$ from the initially optimized amplitude.

4.5.2 Optimization of aberration in two-color STED imaging

This section discusses the application of aberration correction using the photon stream-based metric to the two-color STED imaging modality. In two-color STED microscopy, two types of structures in a biological sample, labeled with two different dyes that typically show distinguishable absorption and emission spectra, can be imaged.

Typically, a two-color STED microscope employs a single STED laser to deplete both dyes [54]. This simplifies the experimental setup and enhances its stability. In order for both dyes to exhibit a sufficient stimulated emission cross section at the STED wavelength, they require some degree of spectral overlap in their fluorescence spectra. However, this spectral overlap also likely leads to crosstalk of the fluorescence signals from the different dyes into the respective detection windows. Due to their different emission spectra, the dyes likely possess different stimulated emission cross sections at a particular STED wavelength. Furthermore, they may exhibit different fluorescence lifetimes. Both can impact the measurement of the photon stream-based metric. For a particular STED intensity, the absolute value of the photon stream-based metric is dependent on the fluorescence lifetime, τ_{fl} and stimulated emission cross section, σ_{STED} of the dye employed. In order to demonstrate the empirical relationship between the metric value and τ_{fl} and σ_{STED}, the integral in Eq. 4.1 is derived by considering $T_1 = T$ and $T_2 = \infty$. Evaluation of the integral gives,

$$M = \frac{1}{1 + \frac{\tau_{fl}\,\sigma_{STED}\,j}{T}} \left\{ 1 - \frac{1}{e^{-T(\frac{1}{\tau_{fl}} + \frac{\sigma_{STED}\,j}{T})}} \right\} \tag{4.2}$$

Here, j is defined as in section 4.1.1. For commonly used dyes in two-color STED microscopy, the values of σ_{STED} can vary to one order of magnitude (known by personal

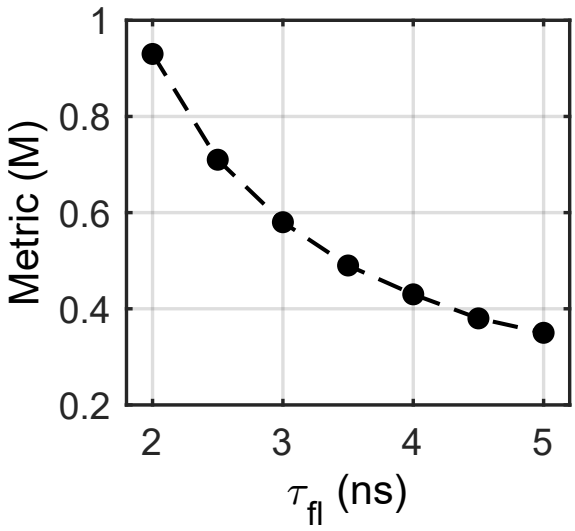

Figure 4.16: Photon stream-based metric values are calculated for different fluorescence lifetime following Eq. 4.1. $I_{STED} = 0.2MW/cm^2$ is used.

communication with Abberior GmbH, on 17.05.2023). Since the product of j and σ_{STED} enters the formula, a change in σ_{STED} to σ'_{STED} can be represented as a rescaled j to j' and Fig. 4.1 can be reproduced. Therefore, metric values are plotted here as a function of τ_{fl} only. Fig. 4.16 illustrates the metric values for different values of τ_{fl} while keeping the j value fixed. The values of τ_{fl} are chosen to span the typical fluorescence lifetimes of dyes commonly used in STED microscopy. These ranges can be obtained from websites such as Abberior.com or atto-tec.com. The metric values are calculated for an exemplary I_{STED} value of $0.2MW/cm^2$, with other parameters taken from section 4.1.1. It can be observed that as τ_{fl} increases, the metric value decreases. When two different structures in the same sample are labeled with different dyes, interchannel crosstalk can cause the relative contribution of each dye to the pixel count to vary based on the spatial distribution of the dyes. Consequently, if the dyes have different properties such as σ_{STED} and τ_{fl}, the absolute value of the metric can also fluctuate from one pixel to another at a specific aberration amplitude. This variation can lead to a false maximization of the metric.

To avoid this issue, two approaches can be employed, either individually or in combination. First, if the interchannel crosstalk is well-characterized, such as through calibration measurements, the metric calculation can be limited to pixels where the contribution of the other dye is negligible. Second, by carefully selecting the measurement protocol and the dyes, it is possible to minimize the interchannel crosstalk to sufficiently low levels where its impact on the metric calculation becomes insignificant. In this thesis, the second approach is taken. In the experimental setup employed in this thesis, a pixel interleaved scheme is utilized, where the sample is not illuminated with both excitation lights simultaneously. Instead, the excitation lights are applied sequentially for each pixel, and the respective

fluorescence signal is recorded separately. This sequential illumination strategy helps minimize crosstalk between the fluorescence signals. To evaluate aberration correction in two-color STED imaging, the selection of the following two dyes is based on their compatibility with the available laser wavelengths and their low anticipated crosstalk according to the specifications of the setup: Abberior star635 (AS635, Abberior STAR 635, Abberior, Germany) and Abberior star580 (AS580, Abberior STAR 580, Abberior, Germany).

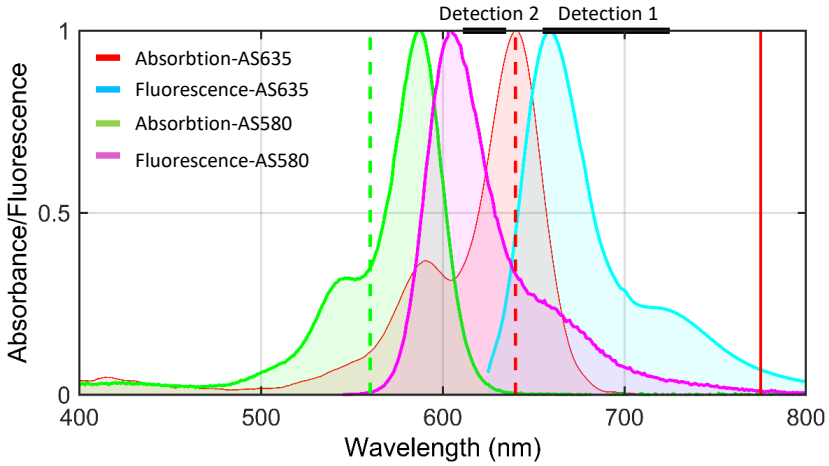

Figure 4.17: Normalized absorption and fluorescence spectra of AS635 and AS580. The red and cyan shaded regions represent the absorption and fluorescence spectra of AS635, respectively. The red dashed line indicates the excitation wavelength of $640nm$. Similarly, the green and magenta shaded regions represent the absorption and fluorescence spectra of AS580, respectively. The green dashed line corresponds to the excitation wavelength of $560nm$. The red solid line represents the STED wavelength. The fluorescence spectra data for AS635 and AS580 are obtained from the abberior website. The detection window wavelengths for channel 1 and channel 2 are indicated by the black lines.

The fluorescence lifetime of AS635 is $2.8ns$, while the fluorescence lifetime of AS580 is $3.5ns$ [55]. Fig. 4.17(a) presents the absorption and emission spectra of both dyes. The absorption spectrum of AS635 is represented by the red shaded region, while its fluorescence spectrum is shown by the cyan shaded region. Similarly, the absorption spectrum of AS580 is depicted by the green shaded region, and its fluorescence spectrum is represented by the magenta shaded region. The vertical dashed lines in red and green indicate the excitation wavelengths of $640nm$ and $560nm$, respectively, while the solid red line indicates the STED wavelength. The detection windows for are indicated by the black horizontal bars.

To calibrate the crosstalk between AS635 and AS580 dyes, two single-stained samples are used. In one sample, the F-actin network in a vero cell is labeled with AS635, while

in the other sample, the microtubule network in a vero cell is labeled with A$S580$. Both samples are embedded in mowiol and subjected to xy STED imaging at the focal plane using an oil objective lens with *NA* $= 1.35$.

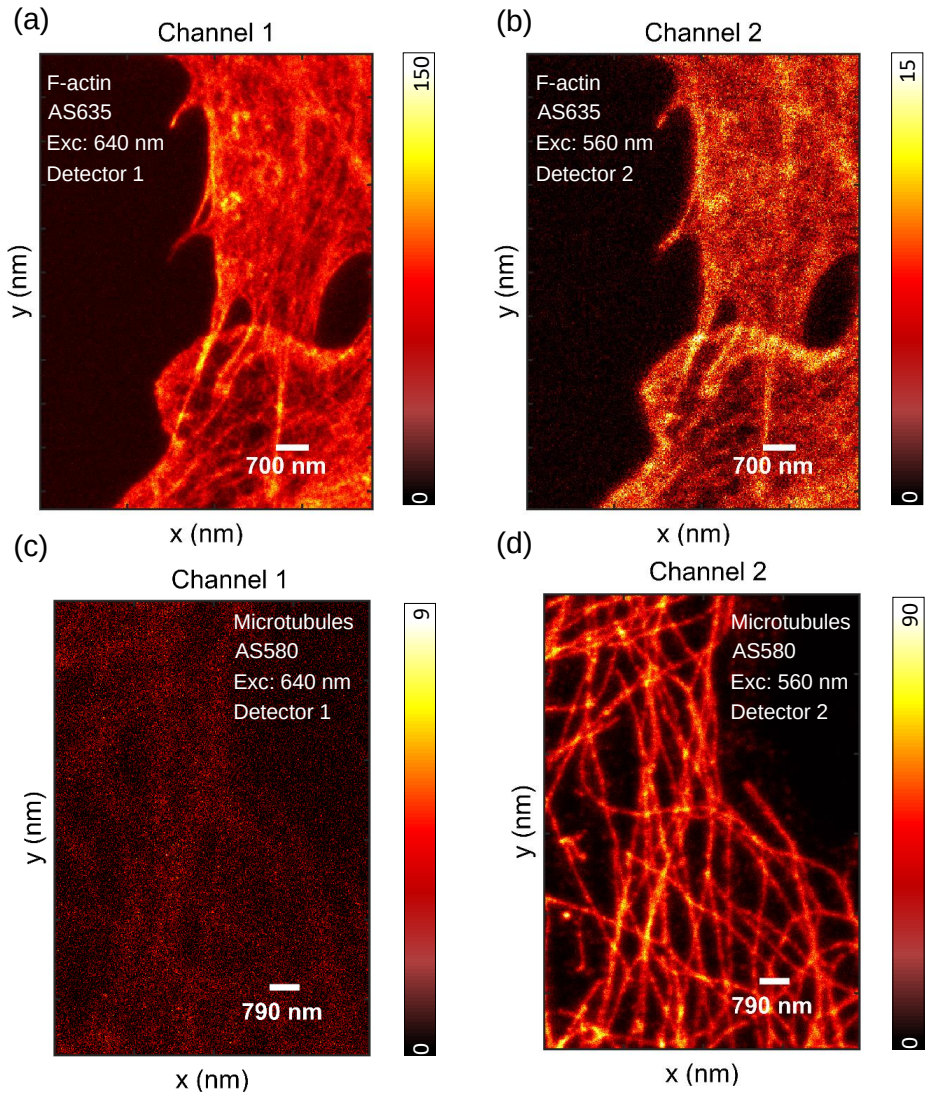

Figure 4.18: xy STED image of F-actin labeled with AS635 at the focal plane using an oil objective lens with a *NA* of 1.35. The image is recorded using $640nm$ excitation beam with a power of $1.53\mu W$ active in channel 1 and STED beam with a power of $92mW$ at the back focal plane of the objective lens. Additionally, $560nm$ excitation beam with a power of $1.12\mu W$ at the back focal plane of the objective lens is also active in channel 2. (a) Signals are detected by the detector placed in channel 1 (b) Signals are detected by the detector placed in channel 2. xy STED image of microtubule labeled with AS580 at the focal plane using an oil objective lens with a *NA* of 1.35. The image is recorded using $560nm$ excitation beam with a power of $1.28\mu W$ active in channel 2 and STED beam with a power of $114mW$ at the back focal plane of the objective lens. Additionally, $640nm$ excitation beam with a power of $2.75\mu W$ at the back focal plane of the objective lens is also active in channel 1. (c) Signals are detected by the detector placed in channel 1. (d) Signals are detected by the detector placed in channel 2

During the imaging process, the $640nm$ excitation beam is activated and the corresponding signal is captured by detector 1. This combination is referred as channel 1. Similarly, the $560nm$ excitation beam is activated and the corresponding signal is recorded by detector 2. This combination is referred as channel 2. Firstly, the AS635-labeled F-actin network is imaged using powers of the $640nm$ excitation, $560nm$ excitation and STED beam at the back focal plane of the objective lens $1.53\mu W$, $1.12\mu W$, and $92mW$, respectively. Fig. 4.18(a) displays the xy STED image of the F-actin network formed in channel 1 with a FOV of $7.6\mu m$ x $10.4\mu m$, a pixel size of $20nm$ x $20nm$, and a pixel dwell time of $100\mu s$. Fig. 4.18(b) shows the image of the same FOV captured in channel 2, indicating the presence of crosstalk of about 10%. The colorbar in channel 2 represents a signal intensity that is 10% of the signal in channel 1.

Secondly, the AS580 labeled microtubule network is imaged with a FOV of $7.9\mu m$ x $11.4\mu m$, a pixel size of $20nm$ x $20nm$, and a pixel dwell time of $100\mu s$. The powers of the $640nm$ excitation, $560nm$ excitation and STED beam at the back focal plane of the objective lens are $2.75\mu W$, $1.28\mu W$, and $114mW$, respectively. Fig. 4.18(c) and Fig. 4.18(d) display the xy STED image of the microtubule network formed in channel 1 and 2, respectively. The colorbar in channel 1 represents a signal intensity that is 10% of the signal in channel 2. The crosstalk is only about 1%.

To investigate if the residual fluorescence signal crosstalk affects aberration optimization, a dual-stained sample of a layer of Vero cells where both microtubules and F-actin are labeled with AS635 and AS580, respectively is used. The measurement is carried out using $640nm$ excitation beam, $560nm$ excitation beam, and STED beam with a power of $1.52\mu W$, $0.82\mu W$, and $114mW$, respectively, at the back focal plane of the objective lens. The initial optimization protocol followed for primary coma H with amplitudes ranging from $-80nm$ to $40nm$ with a step of $20nm$ and a photon threshold of $50,000$. Metric values are calculated for the photon streams detected in both channels for each aberration amplitude. Fig. 4.19(a) displays the xy STED image of F-actin recorded in channel 1, with a FOV of $11.2\mu m$ x $21\mu m$, a pixel size of $20nm$ x $20nm$, and a pixel dwell time of $100\mu s$ at the focal plane. Similarly, Fig. 4.19(b) displays the xy STED image of microtubules with the same FOV, pixel size, and pixel dwell time where signals are recorded by the detector in channel 2. The blue band represents the initial optimization, while the green

band represents the subsequent image acquisition.

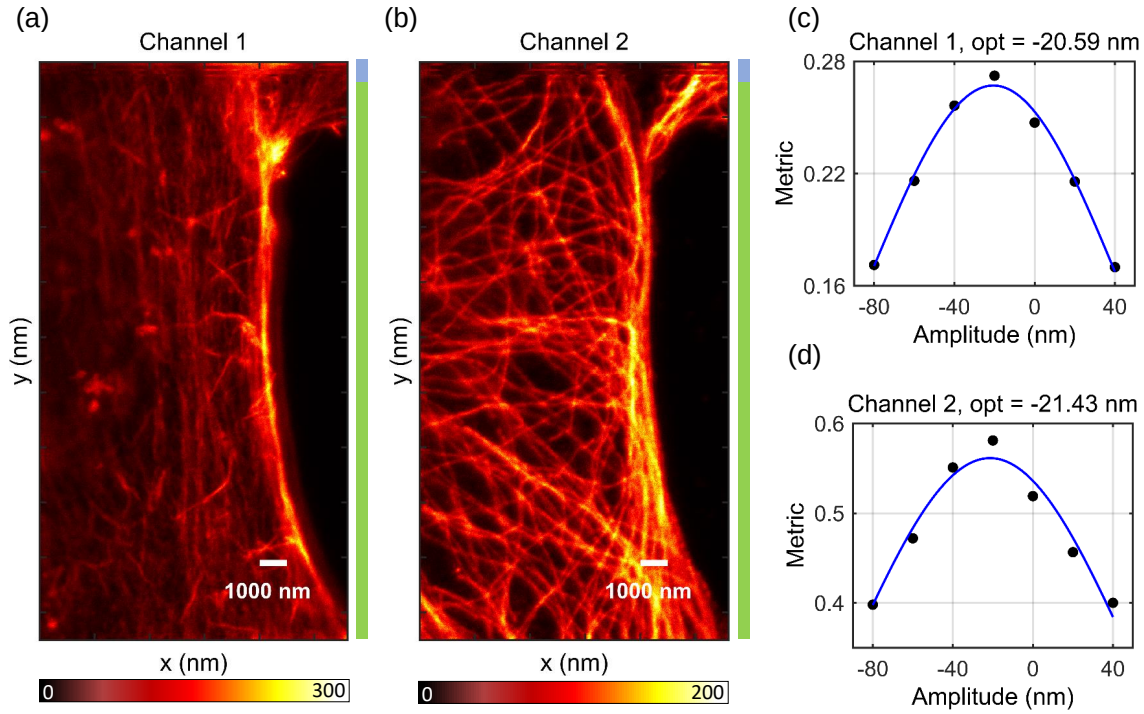

Figure 4.19: Optimization of aberration amplitude on a layer of a cell where F-actin and microtubules are stained with abberior star635 and abberior star 580, respectively, using an oil objective lens with *NA* $= 1.35$, $640nm$ excitation beam with a power of $3\mu W$, $560nm$ excitation beam with a power of $1.2\mu W$, and STED beam with a power of $83mW$ at the back focal plane of the objective lens. The primary coma amplitude ranges from $-80nm$ to $40nm$ in steps of $20nm$ applied to the DM. (a) xy STED image of F-actin with signals detected in channel 1 (b) xy STED image of microtubules with signals detected in channel 2. The blue band in (a),(b) signifies the initial optimization, while the green band signifies the rest of the image acquisition. Metrics obtained during initial optimization with respect to the aberration amplitude in (c) channel 1 and (d) channel 2. The black points represent the metrics obtained and the blue lines represent the corresponding fitting.

The photon stream-based metric values obtained during initial optimization at each aberration amplitude are shown in Fig. 4.19(c) and Fig. 4.19(d) for channel 1 and channel 2, respectively. Although the absolute metric values differ for both channels which is expected, there is a clear maximum in both. After fitting with individual Gaussian functions, the optimized amplitudes are found to be $-20.59nm$ and $-21.43nm$ for channels 1 and 2, respectively. Although there is a deviation of $0.8nm$ between the optimized amplitudes obtained in the two channels, this does not affect the image quality.

This study demonstrates that photon stream-based aberration correction can be in principle directly applied to two-color STED imaging. However, for samples with more complex characteristics such as rapidly and differently changing intensity distributions in both

channels, or in the presence of increased interchannel crosstalk, it may be necessary to employ a pixel selection method based on crosstalk calibration to calculate the metric accurately.

4.5.3 Optimization of aberration in a thick tissue

Aberrations occurring within a thick biological specimen typically arise from variations in the refractive index [13]. These variations are inherent to the non-uniform three-dimensional structures of cells, leading to variations in refractive index. The refractive index of biological tissue can be influenced by factors such as the tissue's composition, density variations, and local temperature differences. Numerous studies have revealed that tissues exhibit a distribution of refractive index values [56, 57]. Therefore, aberrations exhibit significant changes with focusing depth and can even differ among different regions at a specific depth. The presence of sample-induced aberrations pose challenges as it typically restricts the imaging capability beyond the sample's surface. Correcting these aberrations inside the specimen is particularly crucial, especially in biomedical applications. Spherical aberrations are widely recognized as the primary type of aberration in environments characterized by a varying refractive index. However, accurately predicting their magnitude beforehand is often impractical due to the complex internal structure distribution of tissues, which hinders the precise determination of the refractive index. The application of aberration correction using the photon stream-based metric is demonstrated in a thick tissue sample of Drosophila guts. Drosophila, a widely utilized model organism in research, is favored for its cost-effectiveness and rapid generation time. The Drosophila gut, also known as the gastrointestinal tract, serves as a prominent model system for investigating various aspects of gut physiology, host-microbiota interactions, etc. In this context, the α-tubulin protein of microtubule networks within the gut cells is fluorescently labeled using Abberior Star Red (abberior STAR RED, Abberior, Germany).

Sample preparation

The adult Drosophila guts are dissected in phosphate buffered saline. The dissected guts are then fixed in a buffer containing 4% formaldehyde for a duration of 20 minutes. Fol-

lowing fixation, the fixed gut tissues are washed three times for 20 minutes each with a solution of phosphate buffered saline containing 0.1% Triton X-100 and 0.5% bovine serum albumin. A blocking step is performed using bovine serum albumin for one hour. Next, the tissues are incubated overnight at 4° celsius with the primary antibody acetyl-α-tubulin sigma mouse. After washing with phosphate buffered saline three times for 20 minutes each, the guts are incubated for two hours using the secondary antibody Abberior Star Red goat anti-mouse. Following another round of washing with phosphate buffered saline, the guts are mounted using the following procedure: An imaging spacer (iSpacer, Sunjin Lab, Taiwan) is affixed to a cover slide, and the guts are placed within the cavity of the spacer on the cover slide. The embedding medium, abberior Mount Solid (abberior Mount, Solid, Abberior, Germany), is added to the cavity, and a cover slip is then attached from the top. The entire sample preparation and mounting process has been carried out by Dr. Bastian-J. Klußmann-Fricke from Abberior, Göttingen, Germany.

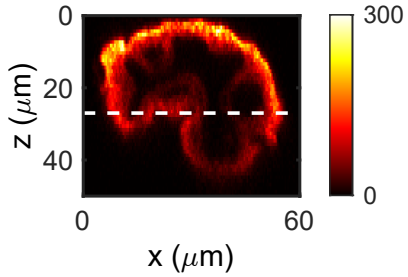

Figure 4.20: Axial xz confocal image of Drosophila gut sample using an oil objective lens with a *NA* $= 1.35$ without aberration correction. The white dashed line indicates the specific z position at which aberration correction is performed.

The refractive index of abberior Mount Solid prior to hardening is 1.38. However, the exact refractive index value of after hardening is not determined. Consequently, the magnitude of the spherical aberration amplitude is believed to be influenced by the difference in refractive index between the immersion medium and the embedding medium, as well as the inherent refractive index variation within the tissue. For aberration correction, the selected depth within the specimen should ensure that the necessary primary spherical amplitude for correction falls within the linear range of the applied response graph, as depicted in Fig. 3.12. Fig. 4.20 presents an uncorrected confocal xz overview of Drosophila gut tissue. The optimization algorithm for correcting multiple aberration modes is applied to a specific layer within the tissue, as indicated by the white dashed line positioned approximately $25\mu m$ deep within the sample.

The xy STED measurement is performed using an oil objective lens with *NA* $= 1.35$,

$640nm$ excitation and STED light at wavelength $775nm$, with a power of $1.06\mu W$ and $49.4mW$, respectively at the back focal plane of the objective lens. A FOV of $21.6\mu m$ x $31.6\mu m$, with a pixel size of $20nm$ x $20nm$ and a pixel dwell time of $240\mu s$ are used. The DM applies various aberration modes including primary coma V $(j = 7)$, primary coma H $(j = 8)$, primary spherical $(j = 11)$ and secondary spherical $(j = 22)$. Based on previous testing of the DM for different refractive index mismatches, it has been established that when the refractive index of the immersion medium exceeds that of the embedding medium, a negative amplitude of spherical aberration is required. Consequently, the range of the primary spherical aberration amplitude is shifted towards negative values and is set within the range of $-120nm$ to $40nm$. For the other aberration modes, the amplitude ranges from $-80nm$ to $80nm$. To ensure a stable metric curve within the tissue's inhomogeneous structure and brightness, both the photon threshold and sampling numbers are set at higher values compared to the previously presented results. The photon threshold is set to $800,000$, and 14 amplitudes are tested within the specified range. The initial optimization process is carried out sequentially for all aberration modes, following the approach explained in Section 4.2. Fig. 4.21(a) shows the xy STED image without aberration correction. In Fig. 4.21(b), the upper section of the xy STED image, marked by the blue band, shows the initial optimization of the aberration modes. The optimization process follows a sequence consisting of primary spherical, secondary spherical, primary spherical (again), primary coma H, and primary coma V. Given the significant contribution of primary spherical aberration, it undergoes a second iteration after optimizing the amplitudes of primary and secondary spherical aberration. In the remaining portion of the image, brightness is significantly improved. Despite the pixel count range spanning $16-1073$ for the uncorrected image and $12-1177$ for the corrected image, to enhance the visibility of the relevant sample regions, the colorbar range for both the uncorrected and corrected images is set to $150-800$ counts. Fig. 4.21(c) displays exemplary line profiles that traverse the structures, indicated by the green line, for both the corrected (red line) and uncorrected (blue line) image. The line profiles are averaged over three consecutive lines, which corresponds to an averaging over three pixels. Similarly, Fig. 4.21(d) displays another line profiles that traverse the structures, indicated by the white line. These line profiles demonstrate the enhancement in brightness achieved after the implementation of

aberration correction. Fig. 4.21(e) represents the initial default aberration amplitudes for each aberration modes. These default amplitudes minimize the residual aberration of the optical system. Fig. 4.21(f) represent the optimized aberration amplitudes obtained after the correction process for each aberration mode.

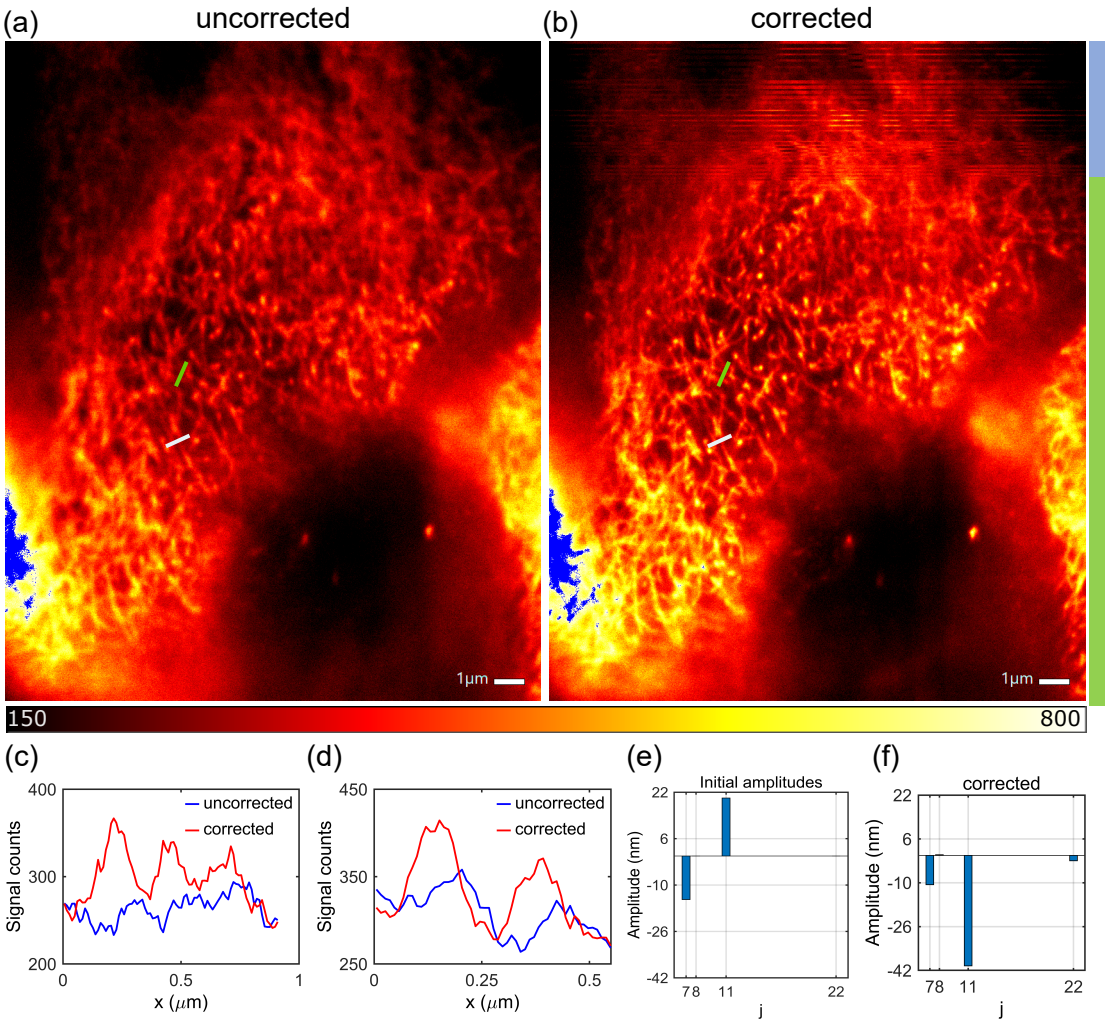

Figure 4.21: Correction of multiple aberration modes is performed inside the Drosophila gut using an oil objective lens with an *NA* of 1.35, $640nm$ excitation beam with a power of $1.06\mu W$ and a STED beam with a power of $49.4mW$ at the back focal plane of the objective lens. Aberration correction is conducted on a FOV of $21.6\mu m$ x $31.6\mu m$, with a pixel size of $20nm$ x $20nm$ and a pixel dwell time of $240\mu s$. (a) xy STED image without aberration correction. (b) xy STED image of the same FOV after aberration correction. The blue band indicates the initial optimization of primary spherical, secondary spherical, primary coma H, and primary coma V in sequential order. The green band represents the remaining image acquisition. Line profiles through the structures, (c) indicated by the green line and (d) white line, in both the STED image without correction (blue) and the STED image with correction (red). This comparison clearly demonstrates the improvement in image quality achieved through aberration correction.(e) Default amplitudes of the four aberration modes without correction are presented in a bar chart style. (f) Optimized amplitudes obtained after aberration correction for the four aberration modes.

4.6 Application to confocal imaging

This section focuses on aberration correction in confocal imaging and also explores the applicability of the photon stream-based metric for this purpose. In confocal imaging, it is commonly observed that the fluorescence signal exhibits a linear dependence on the intensity of the excitation light , as in Eq. 2.3. This linear relationship is only observed when the fluorescence intensity is below saturation levels. The photon stream-based metric utilizes the reduction in fluorescence lifetime resulting from the presence of some other probe light-induced process, as discussed in section 4.1.1. To ensure that changes in the fluorescence signal corresponding to variations in photon arrival times are pronounced and distinguishable, a non-linear dependence of fluorescence signal on the incident light intensity is required. Therefore, to apply the photon stream-based metric in confocal imaging, a second process exhibiting a non-linear dependence of fluorescence signal on light intensity, such as two-photon excitation or STED light-induced stimulated emission, is necessary. In this thesis, to apply the photon stream-based metric in confocal imaging stimulated emission through a STED light with a Gaussian intensity profile at the focus of the objective lens is used. The same experimental setup illustrated in Fig. 3.1 is used for this purpose. It is important to note that the STED laser, is not subjected to any phase modulation by configuring the SLM accordingly. In addition to the photon stream-based metric, another metric can be constructed, which is named here 'confocal-sted'. This metric is defined as the ratio of the fluorescence signal obtained without the irradiation of the STED light to the fluorescence signal obtained with the STED light. The confocal-sted metric does not require time-resolving detection, which provides the advantage of placing lower demands on the detection electronics compared to the photon stream-based metric. During the acquisition of a confocal image, the STED light is added repeatedly for a fraction of the acquisition time. During this irradiation of the STED light, a time-resolved detection of the photons is carried out to determine the photon stream-based metric following the same approach as presented in section 4.1.2, while the confocal-sted metric is derived directly from the fluorescence signals obtained without and with the irradiation of the STED light.

To assess the applicability of both the metrics in aberration correction and to verify if they

exhibit a maximum at the aberration amplitude corresponding to the best image quality, measurements are performed on a layer of $48nm$ diameter crimson beads. An oil objective lens with a *NA* of 1.35 is used, along with $640nm$ excitation light at a power of $3\mu W$ at the back focal plane of the objective lens. The power of the STED light is $0.83mW$ at the back focal plane of the objective lens. The primary astigmatism V $(j = 6)$ is varied over a range of amplitudes from $-40nm$ to $80nm$, with a step size of $20nm$, and applied to the DM. At each aberration amplitude, xy images are recorded at the focal plane, with a pixel dwell time of $200\mu s$. During each $200\mu s$ period, $100\mu s$ are spent without the STED light, and $100\mu s$ are spent with the STED light applied. Both the metrics are computed through post-processing of recorded images. Each image is segmented into non-overlapping regions, with each region containing a certain number of photon counts detected during the irradiation period of the STED light. The photon stream-based and confocal-sted metrics are then calculated for each region, and their corresponding averages and standard deviations are determined across all regions.

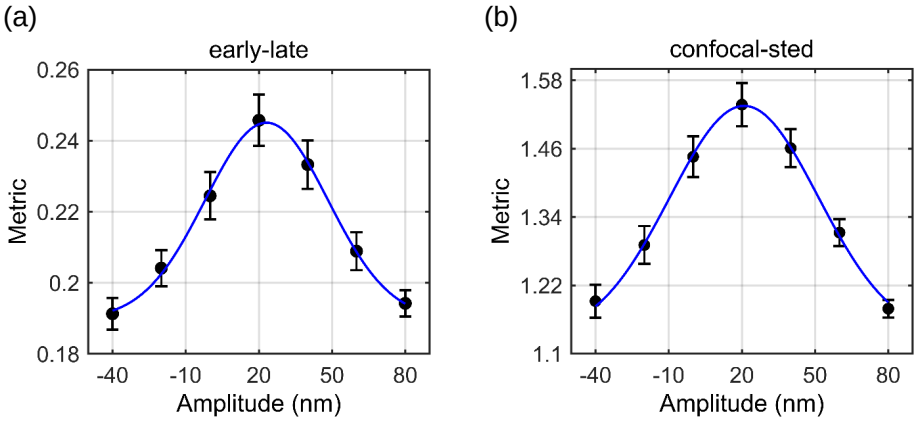

Figure 4.22: Measurements are performed on a layer of crimson beads with a diameter of $48nm$. An oil objective lens with *NA* $= 1.35$, $640nm$ excitation with a power of $3\mu W$, and STED light with a power of $0.83mW$ at the back focal plane of the objective lens are used. Primary astigmatism is varied with an amplitude range of $-60nm$ to $60nm$ in $20nm$ steps, and the corresponding xy images at the focal plane are recorded. The pixel dwell time is $200\mu s$, with $100\mu s$ dedicated to recording images without the STED light and $100\mu s$ for recording images with the STED light. The images are divided into boxes such that $20,000$ photons are detected, and metrics are calculated over these boxes. (a) the average photon stream-based metric and (b) the average confocal-sted metric as a function of aberration amplitude, with error bars indicating the corresponding standard deviation. Blue line represents the fitting. Although the absolute values of the metrics differ, both curves show a maximum at the same aberration amplitude, with a deviation of only $0.08nm$.

Fig. 4.22(a) displays the metric curve plotting the average photon stream-based metric

values as a function of aberration amplitude. The metric values are computed for a photon threshold of $20,000$, and they are averaged over 130 regions, with the error bars indicating the standard deviation. Fig. 4.22(b) shows the same for the confocal-sted metric. Although the absolute values of the two metrics differ, a clear maximum is observed in both cases. After fitting the metric values as a function of aberration amplitudes with a Gaussian function, it is observed that the aberration amplitude corresponding to the maximum metric derived from the fit is $23.14nm$ for the early-late metric and $20.92nm$ for the confocal-sted metric. The deviation between these two values is a negligible amount of $2.22nm$. In section 4.3, it is verified that the best image quality is achieved at an amplitude of $20nm$ for primary astigmatism V.

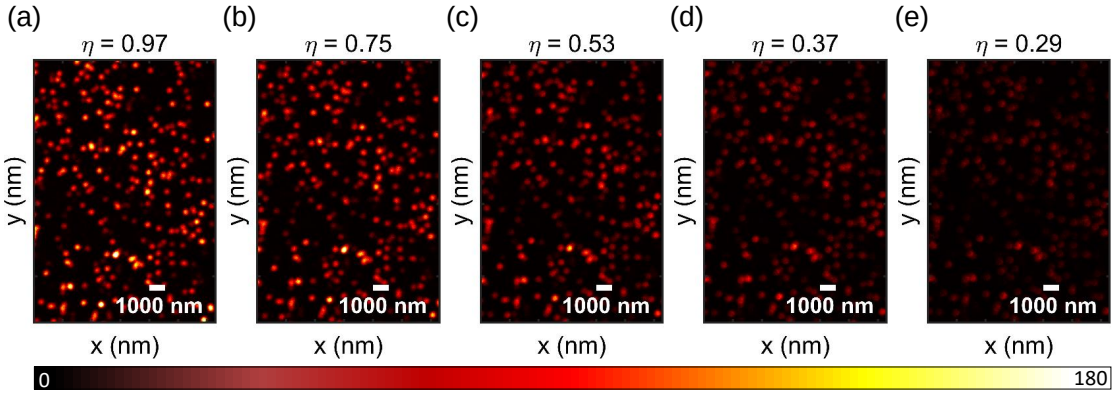

Figure 4.23: xy images of crimson beads recorded in the focal plane using an oil objective lens with a *NA* of 1.35, $640nm$ excitation light with a power of $3\mu W$ at the back focal plane of the objective lens, with different η values correspond to different powers of the STED light at the back focal plane, with the primary astigmatism amplitude optimized at $20nm$. A total pixel dwell time of $200\mu s$ is used, with $100\mu s$ without the STED light and $100\mu s$ with the STED light. (a) $\eta = 0.97$, $P_{STED} = 0.073mW$ (b) $\eta = 0.75$, $P_{STED} = 0.34mW$ (c) $\eta = 0.53$, $P_{STED} = 0.83mW$ (d) $\eta = 0.37$, $P_{STED} = 1.55mW$ and (e) $\eta = 0.29$, $P_{STED} = 2.47mW$.

It is essential to determine the optimal power of the STED light. On one hand, utilizing a low power is essential to maintain an adequate level of non-depleted fluorescence signal intensity during illumination with the STED light and to minimize sample bleaching. On the other hand, it is equally important to obtain metric values with minimal error. According to Eq. 2.21 and Eq. 2.24, the presence of the STED light induces stimulated emission and depletes the fluorescence by a factor of η.

$$\eta \propto e^{-\ln(2)\frac{P_{STED}}{P_{sat}}}, \tag{4.3}$$

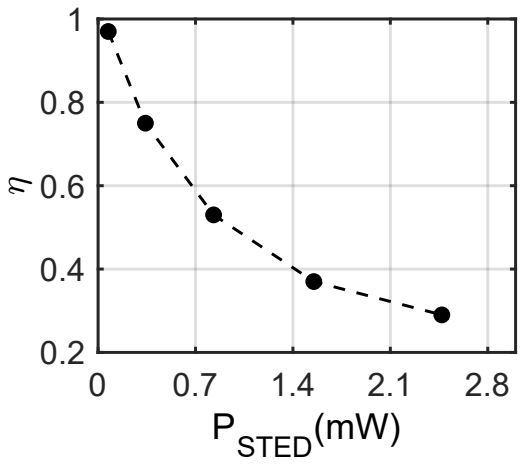

Figure 4.24: η as a function of STED laser power measured at the back focal plane of the objective lens. Measurements are conducted on a layer of crimson beads with a diameter of $48nm$, using an oil objective lens with $NA = 1.35$, and $640nm$ excitation light with a power of $3\mu W$ and various STED light powers at the back focal plane of the objective lens. xy images at the focal plane are recorded with a pixel dwell time of $200\mu s$, in which $100\mu s$ is without the STED light and $100\mu s$ is with the STED light. η is calculated at each STED laser power by taking the ratio of the image obtained with the STED light to the image acquired without the STED light and then, calculating the average count at the center positions of the representative beads.

where P_{STED} is the average power of the STED light. The parameter η associated with the STED laser does not contribute to resolution enhancement. Rather, it acts as a free parameter that influences the metric utilized during the aberration optimization process. In the following, the impact of the η on the metric as well as on the light dose, which is irradiated by the STED light, is analyzed.

To examine this, the aforementioned measurement is conducted for various power values of the STED light. The power is varied across a range of values: $0.073mW$, $0.34mW$, $0.83mW$, $1.55mW$, and $2.47mW$ at the back focal plane of the objective lens. Fig. 4.23 presents exemplary images of crimson beads captured at the optimized primary astigmatism amplitude of $20nm$. The value $\eta = 1$ signifies no application of the STED light to the sample. For each power of the STED light, the value of η is determined at the center of bead images by first taking the ratio of the images obtained with and without the STED light and then averaging over the central region of representative beads. In Fig. 4.24, the variation of η with the applied STED laser powers is shown. A high η value corresponds to a comparatively larger number of detected fluorescence photons, but with minimal influence of the STED light on the photon stream.

To analyze the impact of η on the metric, a post-processing step is performed on the recorded images. This step involves segmenting the images into non-overlapping boxes based on a photon threshold of $20,000$, as mentioned earlier. Two parameters are extracted from each of the metric curves obtained at various η values. The first parameter is contrast of the metric curve which is defined as the maximum average value of the metric

minus the minimum average value of the metric, divided by the sum of the maximum and minimum average metric values. Fig. 4.25 displays the contrast of the metric curves for both metrics as a function of η. The figures indicate that the metric contrast decreases as η increases, as the effect of the STED laser becomes smaller with increasing η.

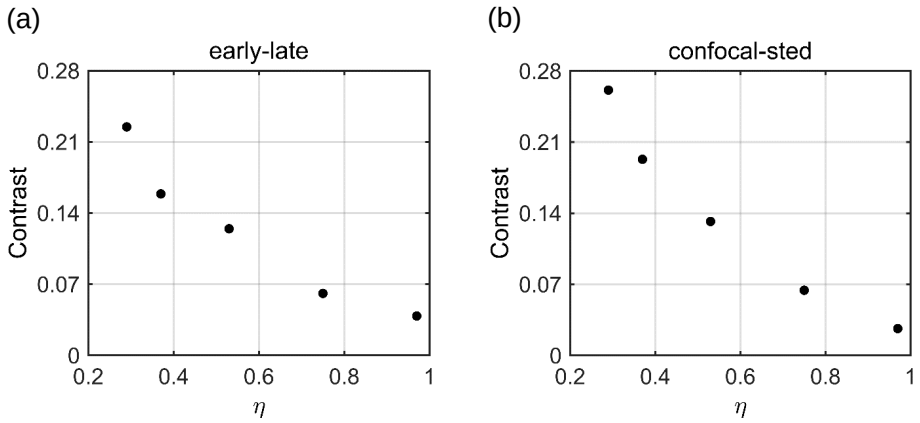

Figure 4.25: The contrast of the metric curves is calculated for both metrics, (a) photon stream-based metric (b) confocal-sted and plotted as a function of η. Metric curves representing the variation of metric values as a function of aberration amplitude determined for both photon stream-based and confocal-sted metrics, each calculated with a photon threshold of $20,000$. xy images of crimson beads at the focal plane are recorded using an oil objective lens with *NA* $= 1.35$, $640nm$ excitation with a power of $3\mu W$ at the back focal plane of the objective lens. η values are varied corresponding to different powers of the STED light.

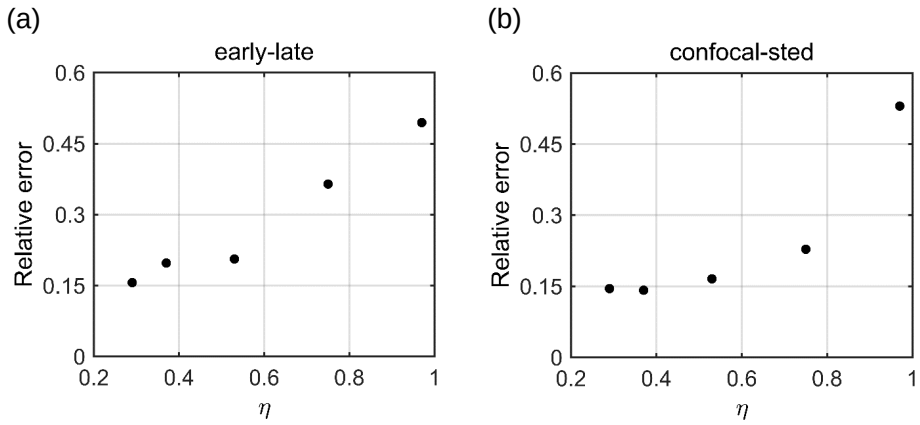

Figure 4.26: Relative variation of metric values as a function of η are determined for both photon stream-based and confocal-sted metrics, each calculated with a photon threshold of $20,000$. xy images of crimson beads at the focal plane are recorded using an oil objective lens with *NA* $= 1.35$, $640nm$ excitation with a power of $3\mu W$, while different powers of the STED light at the back focal plane of the objective lens. The relative variation parameter is constructed by taking the ratio between the mean of the standard deviation of the metrics at each aberration amplitude of a given metric curve and the metric stroke, which is defined as the difference between the maximum and minimum metric values of the same curve. The relative variation is calculated for both metrics (a) photon stream-based metric and (b) confocal-sted, and plotted as a function of η.

The second parameter is defined as the ratio between the mean of the standard deviation of the metrics at each aberration amplitude of a given metric curve and the metric stroke, which is defined as the difference between the maximum and minimum metric values of the same curve. As already used in Fig. 4.9(c), this ratio serves as a measure of the relative variation of the metric values. Fig. 4.26 depicts the relative variation of the metrics as a function of η for both the photon stream-based and confocal-sted metrics. It is observed that the relative variation increases as η increases. A high relative variation of metrics can adversely affect the accuracy of aberration correction. Fig. 4.25 and Fig. 4.26 demonstrate that a low η value is preferable for achieving a higher contrast in the metric curve and lower relative variation of the metrics.

Next, as previously established, the photon threshold value, which is applied to the number of collected photons during illumination with the STED light, plays a significant role in the relative error, as demonstrated in Fig. 4.9(c). Therefore, the photon threshold will be varied as a second parameter. However, before doing so, a simple relationship between the photon threshold and η, as well as the light dose and acquisition time, will be derived. As the value of η increases, it indicates a lower depletion of the fluorescence signal. Consequently, the signal count per pixel, represented as n_p, is directly proportional to η, expressed as $n_p \propto \eta$. Under the assumption of a spatially uniformly distributed fluorescence signal, the number of pixels required to collect a number of photon counts equal to a certain photon threshold, n_{th} is $\frac{n_{th}}{n_p}$.

$$\frac{n_{th}}{n_p} \propto n_{th}\,\frac{1}{\eta} \tag{4.4}$$

Assuming the pixel dwell time is denoted as t_p, the acquisition time, t_{roi} required to collect n_{th} photon count is given by,

$$t_{roi} \propto t_p\, n_{th}\,\frac{1}{\eta} \tag{4.5}$$

The light dose, D can be expressed as the product of the average measurable power of the STED light, P_{STED}, and the acquisition time, $D = P_{STED}.t_{roi}$. Substituting P_{STED} from Eq. 4.3, D can be expressed as,

$$D \propto -P_{sat}\,\frac{1}{\ln 2}\,t_p\,\frac{\ln \eta}{\eta}\,n_{th} \tag{4.6}$$

The relative error of both metrics is computed for different values of the photon threshold. This analysis is carried out at various η values, utilizing the same recorded images and following the previously described post-processing approach. Fig. 4.27(a) and Fig. 4.27(b) illustrate the relative error of both the metrics plotted against the photon threshold for the photon stream-based metric and the confocal-sted metric, respectively, with different values of η. The results indicate that increasing the photon threshold or decreasing η leads to a smaller relative variation, thereby improving the accuracy of the metric. However, Eqs. 4.5 and 4.6 demonstrate that the light dose (D) and the acquisition time (t_{roi}) exhibit the opposite behavior. This means that a higher light dose and a longer acquisition time are required for the initial optimization step. Hence, a trade-off exists between accuracy, on one hand, and the light dose and acquisition time, on the other hand.

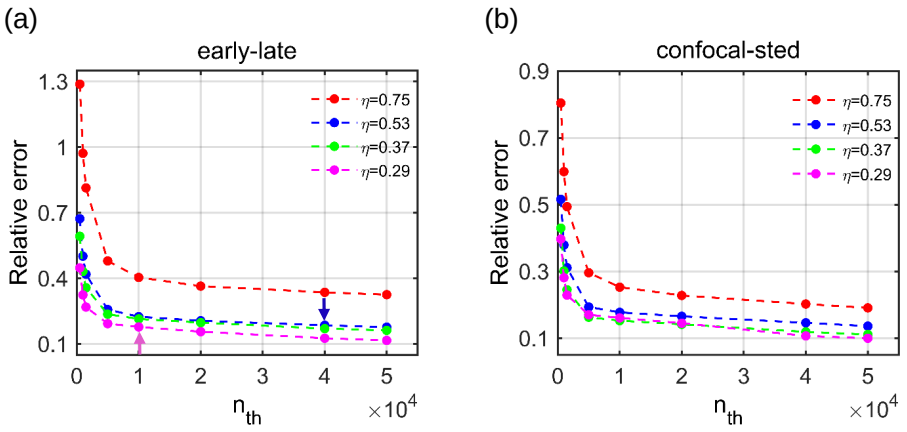

Figure 4.27: Relative variation of metric as a function of photon threshold at different η for (a) photon stream-based metric and (b) confocal-sted.

The data demonstrates that achieving the same relative error is possible with different combinations of η and photon threshold, providing the option to prioritize parameter pairs that result in a more favorable light dose. Furthermore, as D and t_{roi} exhibit different dependencies on η, it is possible to speed up the acquisition time, for example by a factor of two, while maintaining the relative error and light dose at acceptable levels. For the photon-stream based metric, this is for example the case for the data points at $\eta = 0.29$ and $n_{th} = 10,000$, indicated by the magenta arrow in Fig. 4.27(a), and at $\eta = 0.53$ and $n_{th} = 40,000$, indicated by the blue arrow in Fig. 4.27(a). In both cases, the relative error is approximately the same, around 0.18. The corresponding values of D, calculated using Eq. 4.6, are $P_{sat}\, t_p\, 6.15 \times 10^4$ (in arbitrary unit) and $P_{sat}\, t_p\, 6.91 \times 10^4$ (in arbitrary unit),

respectively, which are very similar. However, t_{roi}, calculated using Eq. 4.5, differs significantly between the two parameter pairs, with values of $t_p\, 3.44 \times 10^4$ (in arbitrary unit) and $t_p\, 7.54 \times 10^4$ (in arbitrary unit), respectively. This indicates a difference of more than two times in the acquisition time between the two parameter sets. In order to decrease the values of D and t_{roi}, the photon threshold can be reduced. However, this reduction will result in an increase in the relative error in the metric.

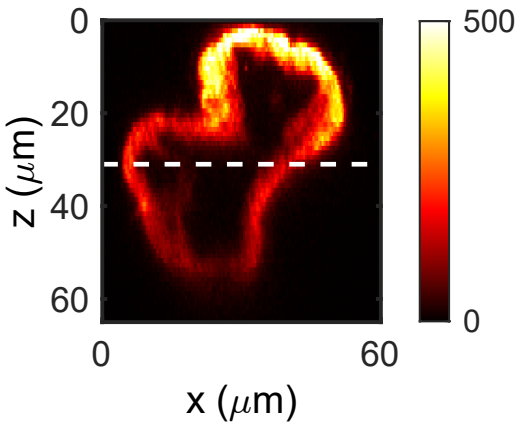

Figure 4.28: Axial xz overview of uncorrected confocal image of Drosophila gut sample using an oil objective lens with *NA=1.35*. Aberration correction is implemented at the z position indicated by the white line.

In order to demonstrate the correction of multiple aberration modes using the photon stream-based metric in confocal imaging of a biological sample, measurements are conducted within a Drosophila guts tissue. The α-tubulin protein of the microtubule network is labeled with the dye Abberior Star Red. The same sample described in section 4.5.3 is utilized. Fig. 4.28 displays an xz confocal image of a section of the tissue without aberration correction. The optimization algorithm for correcting multiple aberration modes is applied at an approximate depth of $31\mu m$ within the sample, indicated by the white dashed line. The measurement is done using an oil objective lens with $NA = 1.35$. The sample is excited with $640nm$ excitation light at a power of $0.33\mu W$ at the back focal plane of the objective lens, while a STED light at wavelength of $775nm$ and with a power of $2.47mW$ is applied to the specimen. The total pixel dwell time is $380\mu s$, divided into $300\mu s$ without the STED light and $80\mu s$ with the STED light. Different aberration modes including primary astigmatism V $(j = 6)$, primary coma V $(j = 7)$, primary coma H $(j = 8)$, primary spherical $(j = 11)$ and secondary spherical $(j = 22)$ are applied to the DM. The amplitude range for primary spherical aberration is set from $-120nm$ to $40nm$, following the same reason as described in section 4.5.3. For the other aberration modes, the amplitude ranges from $-80nm$ to $80nm$. A photon threshold of $80,000$ is chosen, and 12 different amplitudes are tested within the specified amplitude range.

Fig. 4.29(a) displays the xy confocal image of a FOV measuring $18.8\mu m$ x $25.6\mu m$, with a pixel size of $20nm$ x $20nm$, without aberration correction. Fig. 4.29(b) presents the confocal image of the same FOV after aberration correction. The blue band indicates the initial optimization of aberration modes, including primary spherical, secondary spherical, primary spherical (again), primary coma H, primary coma V, and primary astigmatism V, applied sequentially. The spherical aberration amplitudes are tested twice, as mentioned in section 4.5.3. The green band indicates the subsequent image acquisition, where the brightness is significantly improved due to aberration correction. Despite the pixel count range spanning from 6 to 447 for the uncorrected and 5 to 714 for the corrected image, the colorbar range for both images is set to 20 to 700 counts to enhance the visibility of the relevant regions. Fig. 4.29(c) presents exemplary line profiles that traverse the structures, indicated by the green line, for both the corrected (red line) and uncorrected (blue line) images. The line profiles are obtained by averaging over three consecutive lines, corresponding to an averaging over three pixels. While the optimization of multiple aberration modes during data acquisition is performed using the photon stream-based metric, the calculation of the respective confocal-sted metric values is carried out on the recorded image through post-processing. In order to compare the optimized amplitudes for both the photon stream-based metric and the confocal-sted metric for different aberration modes, the optimized amplitude values for confocal-sted metric are derived in the same manner, as for the early-late metric, through fitting with a Gaussian function. In Fig. 4.29(d), the optimized amplitudes for the photon stream-based metric are represented by blue circles, while the optimized amplitudes for the confocal-sted metric are denoted by red squares. The figure illustrates that the optimized aberration amplitudes exhibit a deviation of no more than $5nm$ for both the metrics used.

These results demonstrate that the aberration correction protocols in confocal imaging can be effectively achieved using both the photon stream-based metric and the confocal-sted metric.

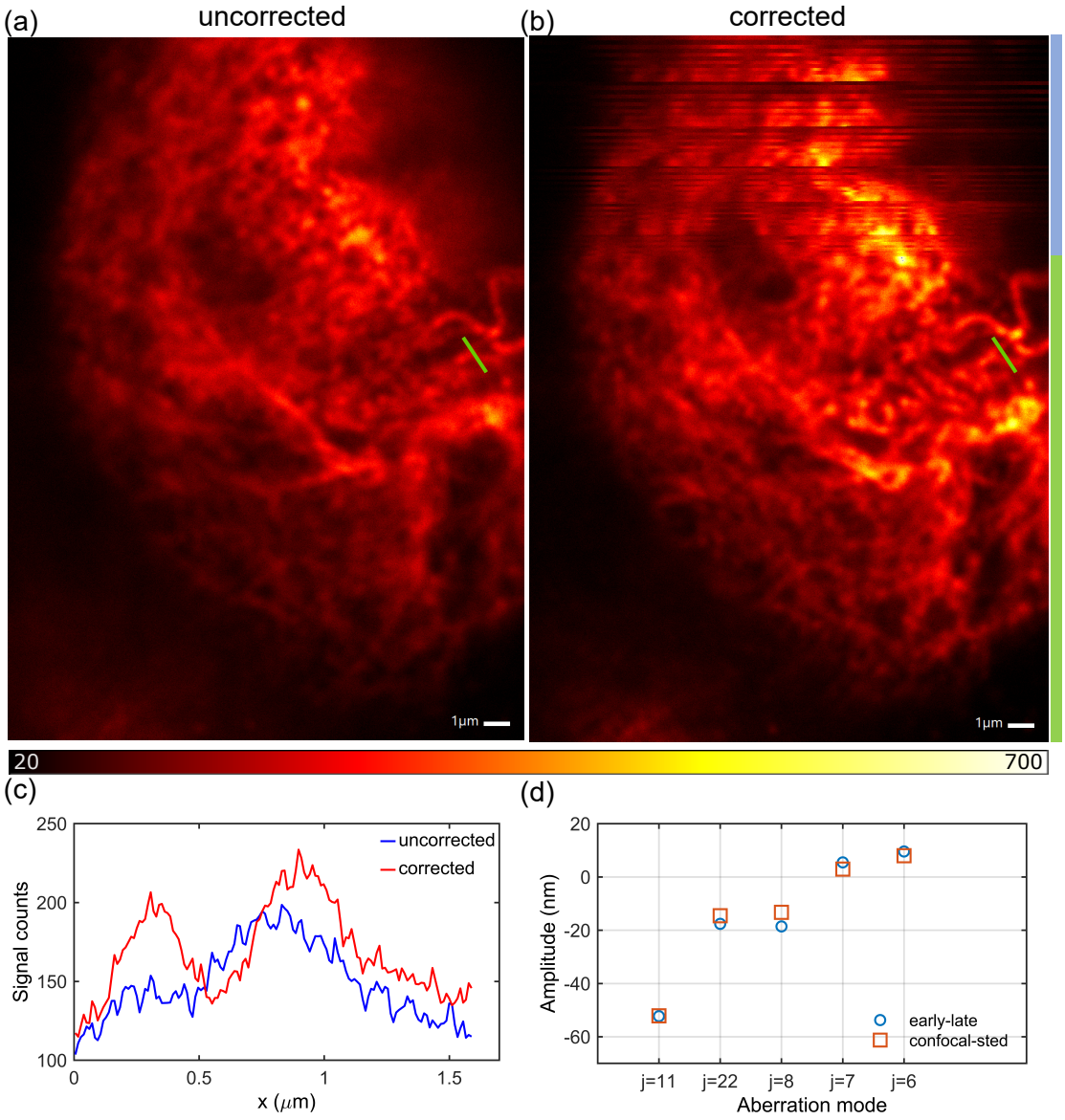

Figure 4.29: Correction of multiple aberration modes in confocal imaging is performed inside the Drosophila gut using an oil objective lens with an *NA* of 1.35, $640nm$ excitation beam with a power of $0.33\mu W$ and the STED laser beam with a power of $2.47mW$ at the back focal plane of the objective lens. Aberration correction is conducted on a FOV of $18.8\mu m$ x $25.6\mu m$, with a pixel size of $20nm$ x $20nm$ and a pixel dwell time of $380\mu s$. Within this dwell time, $300\mu s$ is allocated without the STED laser, while the remaining $80\mu s$ is with the STED laser. (a) xy confocal image without aberration correction. (b) xy confocal image of the same FOV after aberration correction. The blue band indicates the initial optimization of primary spherical, secondary spherical, primary coma H, and primary coma V, primary astigmatism V in sequential order. The green band represents the remaining image acquisition. (c) line profiles are shown through the structures, marked by the green line, in both the image without correction (blue) and the image with correction (red). This comparison serves to clearly illustrate the improvement in image quality achieved through aberration correction. (d) Optimized aberration amplitudes obtained from the automatic algorithm using the photon stream-based metric (blue circle) and derived by post-processing of the recorded image for confocal-sted metric (red rectangle).

Chapter 5

Summary and discussions

In this thesis a method for correcting aberrations in STED microscopy has been presented. The approach is based on indirect optimization of a metric utilizing a DM and employs a recently patented photon stream-based metric that analyzes the detected fluorescent photon flux from the sample.

The experiments have been performed using a two-color pulsed STED microscopy setup, which had been upgraded with a DM. Excitation beams of wavelengths $640nm$ and $560nm$, and a STED beam of wavelength $775nm$, have been utilized. An SLM has been used to shape the wavefront of the STED beam to a helical pattern, allowing for resolution enhancement in both lateral directions. Imaging has been carried out using either an oil or water objective lens. The resolution of the STED microscope has been characterized by varying the applied STED beam powers and detecting fluorescence signal from single fluorescent crimson beads. Throughout almost all the measurements presented in this thesis, a comparatively long pixel dwell time has been used. This choice has been made as low excitation powers have been used to ensure that the APD does not saturate. The linear range of the APD used in this thesis is limited to a maximum of 2×10^6 counts per second. It is important to note that this limitation is not general, as one can utilize multiple APDs by using a beamsplitter.

The DM has been characterized by assessing its efficiency in generating Zernike polynomials of a particular type and amplitude using a wavefront sensor. In order to use two different objective lenses with different pupil diameters, and considering limitations

in the available lens configurations, only a portion of the active area of the DM could be employed for wavefront modulation. Consequently, only $9-10$ actuators across the diameter, out of the total 12 available, have been utilized. This restricted the DM's capability to generate higher-order aberration modes, including tertiary spherical aberration, with sufficient quality and strength. It has been verified that there is a linear relationship between the aberration amplitude measured by the wavefront sensor and the aberration amplitude applied to the DM, but this relationship holds true only within a limited amplitude range. This has resulted in a reduced working depth in the sample and correction quality. However, this is not a fundamental limitation and can be addressed by increasing the number of utilized actuators. This can be achieved, for example, either by implementing a modified optical system or by using a different DM of the same diameter but with a smaller actuator pitch.

The properties of the photon stream-based metric have been thoroughly analyzed using fluorescent crimson beads in the $2D$ STED imaging modality. Experimental evaluations have demonstrated that adjusting the amplitude of Zernike-based aberration modes leads to the attainment of maxima in the metric. These maxima correspond to settings associated with superior image quality, characterized by maximum brightness and resolution. These findings have been verified for various aberration modes that are particularly relevant for fluorescence microscopy on axially extended biological specimens. Furthermore, experimental studies have demonstrated, exemplary results for primary spherical aberration, that the amplitude of aberration leading to the maximum metric value remains consistent, even when altering the sample type from specimens with distinct structural features (e.g., single fluorescent beads) to completely featureless samples (e.g., dye solutions). With respect to the sample's brightness, it has been observed that the aberration amplitude at which the metric reaches its maximum value is independent of the sample's brightness, as illustrated in Fig. 4.5. However, Fig. 4.5 also depicts a decrease of the overall metric values as the brightness of the image decreases. This observation can be explained as follows: Firstly, it should be noted that the spatial distribution of STED intensity over the excitation PSF is not constant, as assumed for simplicity in Eq. 4.1. Rather, it follows a two-dimensional spatial distribution determined by the STED PSF. As a consequence, in STED images of point-like objects, which can be considered equivalent

to the effective PSF, the metric values exhibit local variations across the image of each object. The metric is comparatively lower at the center of the effective PSF due to the lower STED intensity and increases towards the rim of the effective PSF, where the local STED intensity is higher. Secondly, in the analysis of experimental data, a threshold has been applied to account for the presence of unspecific background signal. This threshold ensures that only pixels with counts above a certain value have been considered for calculating the metric. In the case of the sample analyzed for Fig. 4.5, which consisted of small and sparsely distributed microspheres, their STED images closely approximated the effective PSF. Consequently, the thresholding process resulted in an exclusion of the darker outer parts of the bead image. Since the absolute metric values were obtained as a signal-weighted average over the entire STED image, the application of the threshold introduced a dependence of the absolute metric values on the image brightness. With increasing brightness, more outer regions of the effective PSF surpass the background level. Consequently, these regions are included in the metric calculation, resulting in a higher averaged metric value. This effect is prominently noticeable in bead samples but is expected to have less significance for more extended sample structures. Based on this analysis, it can be concluded that when performing automatic aberration correction, it is advisable to compare sufficiently similar regions within the sample. Further investigation should be performed to explore alternative approaches for metric calculation, such as weighting schemes, that may lead to independence of the absolute metric values from sample brightness.

The application of spherical aberrations by the DM to the imaging system results in an axial shift of the PSF, necessitating the development of a method to mitigate this effect. This was crucial to enable automatic correction of sample-induced aberrations within a specific image plane. To evaluate the efficacy of this method, bead samples were utilized in confocal imaging experiments. The results obtained within the range of spherical aberration amplitudes applied in this thesis were found to be satisfactory. However, it should be noted that the effectiveness of this approach is influenced by the focusing depth and refractive index mismatch of the sample. Therefore, the data presented in Fig. 4.7 serves as an illustrative example specific to the particular kind of sample used. Further improvement might be achieved by employing more advanced technique, such as constructing

modified orthogonal Zernike functions, as demonstrated in the study by J. Cui et al [38]. For the automatic correction of sample induced aberrations, a Python-based algorithm has been developed, which sequentially corrects multiple aberration modes. The algorithm sequentially accesses the number of photons detected within each line, both in the early and total photon counts, and accumulates them. Once a pre-defined photon threshold is reached, the metric is calculated, and the corresponding aberration strength on the DM is adjusted. Subsequently, the photon counters are reset to zero in preparation for the next iteration. The purpose of introducing the photon threshold is to improve the signal-to-noise ratio. The influence of this threshold on the metric and optimization process has been extensively examined, leading to the determination that a photon count of $20,000$ or higher is appropriate for achieving stable optimization, as demonstrated in Fig. 4.9, when using a bead sample. The determination of the appropriate photon threshold is dependent on various factors, including the metric stroke and the number of tested aberration amplitudes within the given range. The example provided serves as a protocol for establishing the photon threshold, and it may be necessary to perform this analysis for each specific sample and under different experimental conditions. It is important to note that when working with biological samples, a higher photon threshold is often required to achieve a stable metric curve during the optimization of aberration amplitudes. This higher threshold can be justified due to the inherent characteristics of biological samples, such as uneven brightness and structural distribution, which tend to be more heterogeneous compared to bead samples. An alternative approach to the current line-based evaluation of photon counts is to perform it on a pixel-wise basis. This modification would enable the adaptive selection of the evaluation region based on the structure of the sample. However, implementing this approach would require additional modifications in the control of image acquisition, such as employing a field programmable gate array for the implementation of the metric calculation. This field programmable gate array-based implementation would provide the necessary computational efficiency for pixel-wise evaluation and adaptive region selection.

In this thesis, the correction of multiple aberration modes follows a sequential approach, where each mode is addressed one after another. However, alternative methods exist where a simultaneous correction of all relevant aberration modes can be achieved. One

such approach is the implementation of a genetic algorithm [58]. This algorithm begins with a trial shape of the wavefront and iteratively modifies the wavefront while evaluating the resulting metric. Another approach uses a random search algorithm [59]. In this method, random voltages are applied to the actuators, altering the wavefront shape. The metric is then calculated. By repeating this process with multiple random wavefront modifications, the algorithm searches for the optimal configuration that maximizes the metric value.

The photon stream-based metric has shown a maximum at the optimal aberration amplitude, indicating the point of highest image quality. Furthermore, experimental observations have revealed that variations in the aberration amplitude within a range of approximately $\pm 5nm$ around this optimal value do not have a significant impact on image quality. Taking advantage of this characteristic, the aberration correction algorithm has been further developed to enable simultaneous and continuous detection and compensation for any changes in the prevailing aberrations. This approach was tested on a two-layered bead sample, with each layer positioned at different focusing depths and separated by a thick intermediate layer of refractive index mismatched medium. For STED imaging, the focal plane was initially set to one of the layers. However, during the image acquisition, after the initial optimization, the focal plane was intentionally shifted to the other layer. Consequently, the spherical aberrations present in the system also changed, but this change was successfully detected and compensated for using the continuous aberration correction scheme. This continuous aberration correction scheme shows great promise for $3D$ STED imaging of tissue, especially in xz axial imaging. As the imaging depth changes, the spherical aberrations can be automatically adapted and corrected, providing a significant advantage in maintaining optimal image quality throughout the entire imaging process.

The successful application of the aberration correction method using the photon stream-based metric has also been demonstrated in two-color STED imaging. This technique involves the utilization of two different dyes, each possessing distinct fluorescence lifetimes and stimulated emission cross sections. The metric values can be influenced by factors such as the fluorescence lifetime and stimulated emission cross section of the dyes used. In situations where inter-channel cross talk is non-negligible or when dealing

with challenging samples exhibiting heterogeneous changes in brightness, a pixel selection method based on cross talk may be required during the automatic optimization of aberration amplitude. This technique would involve identifying and including only those pixels in the metric calculation where the cross talk is negligible. By selectively considering these pixels, the accuracy of the metric calculation could be improved, particularly in scenarios where inter-channel cross talk or sample heterogeneity pose challenges to achieving accurate aberration optimization.

The developed aberration correction method has also been successfully applied to confocal imaging, enabling rapid aberration correction in parallel with image acquisition. However, this comes at the expense of requiring an additional laser light source specifically for STED illumination. Alongside the photon stream-based metric, a new metric called confocal-sted has been introduced. The confocal-sted metric offers several advantages. Firstly, it does not necessitate detection with a time resolution better than the fluorescence lifetime, which allows for the use of simpler and more cost-effective detection electronics. Additionally, the confocal-sted metric can be employed with continuous STED and excitation lasers, reducing the overall cost of the imaging setup. It is important to note that when using continuous STED light, Eq. 2.14 has to be adapted, along with the expression of the depletion factor η. However, one can still expect a clearly pronounced extremum of the metric at accurately compensated aberration amplitudes. The introduction of STED light in the confocal imaging process resulted in a depletion of the fluorescence signal by a certain factor. To assess the impact of this depletion factor on various aspects, such as the accuracy of the metric, the light dose, and the time needed for initial optimization, a comprehensive analysis was conducted. The findings of this analysis highlighted the need to strike a balance between the accuracy of the metric and the practical considerations of light dose and acquisition time. In other words, optimizing these factors requires a trade-off: increasing the accuracy of the metric may necessitate higher light doses and longer acquisition times, while compromising on accuracy can lead to reduced light doses and shorter acquisition times. Therefore, it becomes crucial to find an optimal compromise that ensures an acceptable level of accuracy in the metric while minimizing the required light dose and acquisition time. This balance will vary depending on the specific imaging conditions and experimental requirements, and it should be carefully considered in order

to achieve the best overall performance in aberration correction.

In summary, the findings presented in this thesis demonstrate the potential of the automated aberration correction scheme, utilizing the photon stream-based metric, for rapid and continuous correction of aberrations alongside image acquisition. This capability makes it well-suited for routine application in biomedical research. The results highlight the effectiveness of the scheme in achieving accurate aberration correction and maintaining optimal image quality in real-time. Overall, this thesis contributes to the advancement of aberration correction techniques and underscores their value in enabling high-quality imaging for biomedical research purposes.

Bibliography

[1] S. W. Hell, J. Wichmann, Breaking the diffraction resolution limit by stimulated emission: stimulated-emission-depletion fluorescence microscopy, *Opt. Lett.*, **11**, 780-782 (1994).

[2] S. Deng, L. Liu, Y. Cheng, R. Li, Z. Xu, Investigation of the influence of the aberration induced by a plane interface on STED microscopy, *Opt. Express*, **17 (3)**, 1714-25, (2009).

[3] M. J. Booth, Adaptive optics in microscopy, *Phil. Trans. R. Soc*, **A 365**, 2829-2843, (2007).

[4] D. Débarre, E. J. Botcherby, T. Watanabe, S. Srinivas, M. J. Booth, T. Wilson, Image-based adaptive optics for two-photon microscopy, *Opt. Lett.*, **34(16)**, 2495, (2009).

[5] A. Egner, C. Geisler, F. Rocca, Method and microscope with a correction device for correcting aberration-induced imaging errors, *Patent*, PCT/EP2020/068501, (2021).

[6] H. Helmholtz, H. Fripp, On the Limits of the Optical Capacity of the Microscope, https://doi.org/10.1111/j.1365-2818.1876.tb05606.x.

[7] T. J. Gould, P. A. Pellett, J. Bewersdorf, STED Microscopy, Fluorescence Microscopy, From Principles to Biological Applications, *Wiley-VCH* (2nd ed.), 375-392, (2013).

[8] A. Egner, S. W. Hell, Aberration in Confocal and Multi-Photon Fluorescence Microscopy Induced by Refractive Index Mismatch, Handbook of Biological Confocal Microscopy, *SpringerScience*, 404-413, (2006).

[9] Y. Ue, H. Monai, K. Higuchi, D. Nishiwaki, T. Tajima, K. Okazaki, H. Hama, H. Hirase, A. Miyawaki, A spherical aberration-free microscopy system for live brain imaging, *Biochem. Biophys. Res. Commun.*, **500(2)**, 236-241, (2018).

[10] D. S. Wan, M. Rajadhyaksha, R. H. Webb, Analysis of spherical aberration of a water immersion objective: application to specimens with refractive indices 1.33–1.40, *Journal of Microscopy*, **40**, 274-284, (2000).

[11] T. Staudt, M. Lang, R. Medda, J. Engelhardt, S. W. Hell, 2,2´-Thiodiethanol: a new water soluble mounting medium for high resolution optical microscopy, *Micr. Res. Tech*, **70**, 1-9, (2006).

[12] Z. Kam, B. Hanser, M. G. L. Gustafsson, D. A. Agard, J. W. Sedat, Computational adaptive optics for live three-dimensional biological imaging, *Proc. Natl. Acad. Sci.*, **98**, 3790-3795, (2001).

[13] M. J. Booth, Adaptive optical microscopy: the ongoing quest for a perfect image, *Light:Science and Application*, **3**, e165, (2014).

[14] J. W. O'Byrne, P. W. Fekete, M. R. Arnison, H. Zhao, M. Serrano, D. Philip, W. Sudiarta, C. J. Cogswell, Adaptive optics in confocal microscopy, *Adaptive Optics for Industry and Medicine, World Scientific*, **pp.**, 85-90, (1999).

[15] J. M. Girkin, S. Poland and A.J. Wright, Adaptive optics in confocal and twophoton microscopy of rat brain: a single correction per optical section, *Proc. of SPIE*, **6442**,(2007).

[16] B. R. Patton, D. Burke, D. Owald, T. J. Gould, J. Bewersdorf, M. J. Booth, Three-dimensional STED microscopy of aberrating tissue using dual adaptive optics, *Opt. Express*, **8**, Vol 24, 8862, (2016).

[17] T. J. Gould, D. Burke, J. Bewersdorf, M. J. Booth, Adaptive optics enables 3D STED microscopy in aberrating specimens, *Opt. Express*, **19**, Vol 20, 20998, (2012).

[18] X. Tao, J. Crest, S. Kotadia, O. Azucena, D. C. Chen, W. Sullivan, J. Kubby, Live imaging using adaptive optics with fluorescent protein guide-stars, *Opt. Express*, **20**, 15969-15982, (2012).

[19] L. Sherman, J. Y. Ye, O. Albert, T. B. Norris, Adaptive correction of depth-induced aberrations in multiphoton scanning microscopy using a deformable mirror, *J.Microsc.*, **206**, 65-71, (2002).

[20] D. Burke, B. Patton, F. Huang, J. Bewersdorf, M. J. Booth, Adaptive optics correction of specimen-induced aberrations in single-molecule switching microscopy, *Optica*, **2 (2)**, 177-185, (2015).

[21] J. R. Lakowicz, Principles of Fluorescence Spectroscopy, *Springer* (3rd ed.), (2006)

[22] M. Marvin, Microscopy apparatus, *US Patent Office*, 3,013,467, Dec 19 (1961).

[23] A. Egner, C. Geisler, R. Siegmund, STED Nanoscopy, Nanoscale Photonic Imaging, *Springer*, (2020).

[24] M. Born, E. Wolf, Principle of optics, *Cambridge university press* (7th ed.), (1999).

[25] J. W. Goodman, Introduction to Fourier Optics, *McGraw-Hill* (2nd ed.), (2005).

[26] J. R. Krüger, J. K. Findeisen, C. Geisler, A. Egner, Tomographic STED microscopy, *Biomed. Opt. Express*, **11**, 6, (2020).

[27] T. A. Klar, S. Jakobs, M. Dyba, A. Egner, S. W. Hell, Fluorescence microscopy with diffraction resolution barrier broken by stimulated emission, *Proc. Natl. Acad. Sci.*, **97**, 15 , 8206-8210, (2000).

[28] J. Keller, A. Schönle, S. W. Hell, Efficient fluorescence inhibition patterns for RESOLFT microscopy, *Opt. Express*, **15**, 15 , 3361-3371, (2007).

[29] B. Harke, J. Keller, C. K. Ullal, V. Westphal, A. Schönle, S. W. Hell, Resolution scaling in STED microscopy, *Opt. Express*, **16(6)**, 4154–4162, (2008).

[30] B. R. A. Nijboer, The diffraction theory of aberrations, (1942).

[31] J. C. Wyant, K. Creath, Basic Wavefront Aberration Theory for Optical Metrology, *Academic press, Inc.*, (1992).

[32] F. Zernike, Diffraction theory of the knife-edge test and its improved form, the phase-contrast method, *Royal Astronomical Society*, 377-384, (1934).

[33] R. J. Noll, Zernike polynomials and atmospheric turbulence, *J.Opt.Soc.Am*, **66**, 207-211, (1946).

[34] M. J. Booth, M. A. A. Neil, T. Wilson, Aberration correction for confocal imaging in refractive index mismatched media, *J.Microsc.*, **192(2)**, 90-98, (1998).

[35] S. Stallinga, Finite conjugate spherical aberration compensation in high numerical-aperture optical disc readout, *Appl.Opt.*, **44**, 7307-7312, (2005).

[36] M. J. Booth, T. Wilson, Refractive-index-mismatch induced aberrations in single-photon and two-photon microscopy and the use of aberration correction, *Journal of biomedical optics*, **6(3)**, 266-72, (2001).

[37] P. Török, P. Varga, G. Németh, Analytical solution of the diffraction integrals and interpretation of wave-front distortion when light is focused through a planar interface between materials of mismatched refractive indices, *J.Opt.Soc.Am*, **12**, 2660-2671, (1995).

[38] J. Cui, J. Antonell, A. R. Kirkpatrick, P. S. Salter, M. J. Booth, Generalised adaptive optics method for high-NA aberration-free refocusing in refractive-index-mismatched media, *Opt. Express*, **30**, 11809, (2022).

[39] M. J. Booth, Adaptive optics in microscopy, *Philosophical Transactions of the Royal Society A: Mathematical, Physical and Engineering Sciences*, **365**, 2829-2843, (2003).

[40] V. N. Mahajan, Strehl ratio for primary aberrations: some analytical results for circular and annular pupils, *J.Opt.Soc.Am*, **72(9)**, (1982).

[41] J. Antonello, D. Burke, M. J. Booth, Aberrations in stimulated emission depletion (STED) microscopy, *Optics Communications*, **404**, 203-209, (2017).

[42] M. J. Booth1, D. Andrade, D. Burke, B. Patton, M. Zurauskas, Aberrations and adaptive optics in super-resolution microscopy, *Microscopy*, 251-261, (2015).

[43] L. P. Murray, J. C. Dainty, J. Coignus, F. Felberer, Wavefront correction of extended objects through image sharpness maximisation, *SPIE*, **5823**, 60181A, (2005).

[44] D. Debarre, M. J. Booth, T. Wilson, Image based adaptive optics through optimisation of low spatial frequencies, *Opt. Express*, **15(13)**, 8176, (2007).

[45] E. Neubert, D. Meyer, F. Rocca, G. Günay, A. K. Tessmann, J. Grandke, S. S. Sander, C. Geisler, A. Egner, M. P. Schön , L. Erpenbeck, S. Kruss, Chromatin swelling drives neutrophil extracellular trap release, *Nat Commun.*, **14**, 9(1), 3767, (2018).

[46] G. Vicidomini, A. Schönle, H. Ta, K. Y. Han, G. Moneron, C. Eggeling, S. W. Hell, STED nanoscopy with time-gated detection: theoretical and experimental aspects, *PLoS One.*, **8(1)**, e54421, (2013).

[47] J. R. Moffitt, C. Osseforth, J. Michaelis, Time-gating improves the spatial resolution of STED microscopy, *Opt. Express*, **19**, 4242-4254, (2011).

[48] Python Interface named SpecPy, https://pypi.org/project/specpy/

[49] J. Zeng, P. Mahou, M. C. S. Klein, E. Beaurepaire, D. Débarre, 3D resolved mapping of optical aberrations in thick tissues, *Opt. Express*, **3**, 1898-1913, (2012).

[50] M. J. Mlodzianoski, P. J. C. Hathaway, S. M. Bemiller, T. J. McCray, S. Liu, D. A. Miller, B. T. Lamb, G. E. Landreth, F. Huang, Active PSF shaping and adaptive optics enable volumetric localization microscopy through brain sections, *Nat Methods.*, **15(8)**, 583-586, (2018).

[51] C. Bourgenot, C. D. Saunter, J. M. Taylor, J. M. Girkin, G. D. Love, 3D adaptive optics in a light sheet microscope, *Opt. Express*, **20**, 13252-13261, (2012).

[52] R. A. Espinosa, J. Andilla, R. P. Guezenec, O. E. Olarte, M. Nieto, X. Levecq, D. Artigas, P. L. Alvarez, Measurement and correction of in vivo sample aberrations employing a nonlinear guide-star in two-photon excited fluorescence microscopy, *Opt. Express*, **2**, 3135-3149, (2011).

[53] M. A. Neil, R. Juskaitis, M. J. Booth, T. Wilson, T. Tanaka, S. Kawata, Adaptive aberration correction in a two-photon microscope , *J Microsc.*, **200**, 105-108, (2000).

[54] P. A. Pellett, X. Sun, T. J. Gould, J. E. Rothman, M. Q. Xu, I. R. Corrêa, J. Bewersdorf, Two-color STED microscopy in living cells, *Biomed. Opt. Express*, **2(8)**, 2364-71, (2011).

[55] https://abberior.shop/.

[56] J. J. Dirckx, L. C. Kuypers, W. F. Decraemer, Refractive index of tissue measured with confocal microscopy, *J. Biomed. Opt.*, **10(4)**, 044014, (2005).

[57] Y. Zhou, K. K. H. Chan, T. Lai, S. Tang, Characterizing refractive index and thickness of biological tissues using combined multiphoton microscopy and optical coherence tomography, *Biomed. Opt. Express*, **4(1)**, 38-50, (2013).

[58] O. Albert, L. Sherman, G. Mourou, T. B. Norris, G. Vdovin, Smart microscope: an adaptive optics learning system for aberration correction in multiphoton confocal microscopy, *Opt. Lett.*, **25(1)**, 52, (2000).

[59] A. J. Wright, D. Burns, B. A. Patterson, S. P. Poland, G. J. Valentine, J. M. Girkin, Exploration of the optimisation algorithms used in the implementation of adaptive optics in confocal and multiphoton microscopy, *Microsc Res Tech.*, **67(1)**, 36-44, (2005).

List of publications

Parts of this thesis have been published as follows:

- D. Ghosh, F. Rocca, C. Geisler, A. Egner: 'Photon stream-based aberration correction for STED microscopy.', submitted.

Conference contribution

- D. Ghosh, C. Geisler, A. Egner,
  Photon stream-based aberration correction for STED microscopy,
  DPG Meeting 2022, Regensburg, $(04.09.2022 - 09.09.2022)$.

Acknowledgement

The exciting journey of my doctoral research has been some of the most memorable and rewarding experiences of my life. It is my pleasure to express my gratitude here in these couple of pages to the wonderful people who have surrounded me. People, who not only helped me to get settled in a new country but also encouraged, motivated and supported me in a new lab and on this journey.

I would like to express my sincere gratitude to my supervisor, Prof. Dr. Alexander Egner, for providing me with the opportunity to work in his research group and for his invaluable guidance throughout my studies.

I am indebted to Dr. Claudia Geisler for her consistent guidance and support without which my Ph.D. journey would not have been possible. Her careful review, thorough analysis of data, and strong dedication have been truly inspiring.

I would like to thank Prof. Dr. Jörg Enderlein and Prof. Dr. Sarah Köster for their time and providing invaluable advice during my thesis committee meeting. I would also like to thank Prof. Dr. Timo Betz, Prof. Dr. Michael Seibt and Prof. Dr. Fred S. Wouters for being on my examination board.

I would like to express my gratitude to Dr. Francesco Rocca for building up the experimental setup that served as the foundation for my measurements. I must thank Dr. Bastian-J. Klussmann for providing me with the excellent Drosophila sample, without which my research progress would have been hindered.

I would like to express my sincere appreciation to all of my group members. In particular, I would like to thank Dr. Parul Jain for her constant help, both as a colleague and as a friend. She has been valuable to me, providing guidance and assistance in both my work and outside academic life. I thank Dr. René Siegmund for his patience and

thorough guidance in teaching me how to use the experimental setup during my early days in the lab. Lenny Reinkensmeier provided invaluable assistance, whether it was with technical issues or sample preparation, and his willingness to share his knowledge and expertise has been greatly appreciated. I would also like to thank Dr. Julia Kratz, Ayiben Nuerbahati, Theresa Brinker, Dr. Mark Bates, Dr. Carola Gregor for making life easier in lab.

I am grateful to all the members of IFNANO, Special thanks go to Anja Ahrens and Maik Lübbecke, with whom I enjoyed spending time chatting and taking breaks. I would like to express my thanks to the purchasing and administration department of IFNANO for their efficient and helpful services.

I have been fortunate to have a supportive, kind and loving group of people in Goettingen who have become like family to me. My heartfelt thanks goes to ManiSankar Maiti, Sipra Maiti, Anwesha Maiti, Debankur, Manika Knyrim, Jayita Singha Dev, Subhabrata Ghosh, Debarghya Banerjee, Rupamanjari Majumdar, Suparna Chakraborty, Sania Irrum, to name a few. I am thankful to Saientan, Sufi-Raja.

I would like to express my sincere gratitude to my former guide, Dr. Urbasi Sinha, in India, who not only taught me scientific lessons but also valuable lessons in lab work culture e.g. the importance of maintaining a daily lab notebook.

I am immensely grateful to my parents and sister for their unwavering love and support. I would like to take this opportunity to express my heartfelt gratitude to Rituparno, for always being there.

Eidesstattliche Erklärung

Hiermit erkläre ich, dass ich die vorliegende Arbeit selbständig angefertigt, nicht anderweitig zu Prüfungszwecken vorgelegt und keine anderen als die angegebenen Hilfsmittel verwendet habe. Sämtliche wissentlich verwendeten Textausschnitte, Zitate oder Inhalte anderer Verfasser wurden ausdrücklich als solche gekennzeichnet.

Ort, Datum	Unterschrift